



UNIVERSITÀ DEGLI STUDI DI PADOVA

DIPARTIMENTO DI INGEGNERIA INDUSTRIALE
CORSO DI LAUREA IN INGEGNERIA MECCANICA

TESI DI LAUREA MAGISTRALE

Hydrodynamic study of a bow of a combatant hull

Relatore:

Prof. Ernesto BENINI

Laureando:

Federica FERUGLIO

Correlatore:

Ing. Andrea DAL MONTE

Anno accademico 2017/2018

SUMMARY

This thesis deals with methods to study and improve the hydrodynamic performance of a ship. More specifically, it focuses on the ship's resistance and on the modern methods used in the design process to reduce it and achieve the best design configuration. These methods are CFD analyses and optimization techniques. Each aspect related to this modern design process is described in detail.

In the first part of this thesis, Chapter 1, the fundamentals of physics needed to understand the problem at hand are provided. Different mechanisms which cause resistance to the ship's motion are highlighted and the calm water resistance is split into components accordingly. The attention is focused on the main component, due to the wave-making, and on the effects that some geometric features of the hull – the bulbous bow and the transom stern – have on it. Next, similarity laws for naval applications, needed to refer model's data to a full-scale hull, are described. In fact, a fundamental step of the design process is the prediction of ship performance, which can be achieved through experimental tests but also by using statistical or numerical methods. Experimental tests, which are actually performed on scaled models, are in any case essential both to develop a statistical model and to validate a CFD analysis.

Nowadays, CFD simulations represent the most commonly used method to predict ship performance. The main difference between numerical codes used for naval applications and the ones used for other fluid dynamical problems is the presence of two phases and an interface between them. In this thesis, in Chapter 2, a brief overview of the numerical techniques required to catch the location of the water free surface is provided. Following this, the attention is focused on OpenFOAM: an open source C++ library where a great collection of precompiled applications is available to perform different types of analyses. In OpenFOAM, several solvers to perform CFD simulations are provided. Among them, InterFoam is suitable for naval applications.

Once the performance of the ship have been estimated, it may be necessary to improve them in order to fulfil all designer's requirements. For this purpose, optimization techniques are increasingly used in naval applications. The first step of optimization is the parametrization of the hull's geometry to obtain shape variations by changing the values of few parameters. This aspect is discussed in Chapter 4.

Then, it may be convenient to perform a design of experiments to evaluate the influence of variables on ship performance. A design of experiments usually consists in two steps: a sampling phase needed to select a certain number of different individuals followed by a sensitivity analysis, to estimate the main effects of the variables and their interactions. In Chapter 5, a possible approach to perform a design of experiments is presented.

Optimization methods usually require the evaluation of a large number of individuals to reach the optimum configuration. If this is done by means of CFD analyses, a high computational effort may be required. Surrogate models represent an excellent alternative to numerical methods to save time, as they are able to provide an approximation of the system's response in few seconds. Chapter 6 provides a description of some of these models.

Summary

Then, the optimization algorithms which are most commonly used for naval applications, i.e. genetic algorithms, are introduced.

The original part of this thesis is the study and the optimization of the DTMB 5415 hydrodynamics. More specifically the purpose is to evaluate the influence of two details of the ship's geometry, the bulbous bow and the transom stern, on the ship's performance and to improve their shape in order to minimize the ship's resistance. The work has been carried out in four steps, reported respectively in Chapters 3, 4, 5 and 6. Firstly a numerical model has been validated to predict the hull's resistance; secondly a parametrization of the geometry has been proposed; thirdly two design of experiments have been performed to evaluate the influence of the variables on the ship's performance; finally an optimization procedure has been implemented in order to find the best design configuration.

Summary

CONTENTS

Summary	iii
Contents	vii
Introduction	1
1 The Physics of the Problem	5
1.1 Components of Calm Water Resistance	5
1.2 Wave-making Component of the Drag	7
1.2.1 The Bulbous Bow	12
1.2.2 The Transom Stern	13
1.3 Froude's Analysis Procedure	14
1.3.1 Similarity Laws for Model Tests	14
1.3.2 Dimensional Analysis	17
1.3.3 Scaling of the Resistance Coefficient	18
1.4 Conclusions	21
2 CFD Analyses for Naval Applications	25
2.1 Theory: Equations Involved	25
2.1.1 Reynolds-Averaged Navier-Stokes Equations	27
2.1.2 Euler and Laplace Equations	28
2.1.3 Turbulence Models	29
2.2 Two-phases Flows	29
2.2.1 Free Surface Modeling	30
2.3 CFD Analysis with OpenFOAM	32
2.3.1 Compiling OpenFOAM Applications	34
2.3.2 Organization of an OpenFOAM Case	35
2.4 Conclusions	37
3 The Case Study: Hull Simulation with InterFoam	39
3.1 Introduction	39
3.2 The DTMB 5415 OpenFOAM case	41
3.3 Validation	44
3.3.1 The DTC Hull Tutorial	44
3.3.2 The DTMB01 Model	49
3.3.3 The DTMB02 Model	51
3.3.4 Flow Field Analysis	53
3.4 Conclusions	58

4 Geometry Parametrization	61
4.1 Traditional Hull Form Design	61
4.1.1 Main Dimensions	61
4.1.2 Coefficients of Form	64
4.1.3 Traditional Modeling Approach	66
4.2 Modern Modeling Methods	67
4.2.1 Parametric Hull Form Variations	69
4.3 Parametrization of DTMB 5415	72
4.3.1 Parametrization of the Bulbous Bow	72
4.3.2 Parametrization of the Stern	75
4.4 Conclusions	77
5 Design of Experiments	79
5.1 What is a Design of Experiments?	79
5.1.1 Sampling Techniques	80
5.1.2 Sensitivity Analysis Methods	81
5.2 A DoE for the DTMB 5415	82
5.2.1 The First Design of Experiments: DoE1	83
5.2.2 The Second Design of Experiments: DoE2	88
5.3 Conclusions	92
6 Response Surfaces and Optimization	95
6.1 Response Surfaces	95
6.1.1 Polynomial Models	97
6.1.2 Kriging Models	97
6.1.3 Artificial Neural Networks	98
6.2 Optimization Techniques	101
6.2.1 Genetic Algorithms	101
6.3 Optimization of the DTMB 5415	103
6.3.1 First Optimization: OPT1	103
6.3.2 Second Optimization: OPT2	106
6.4 Conclusions	111
Conclusions	114
Bibliography	119

INTRODUCTION

The ship design process has changed considerably over the recent few years. The traditional approach was based on the designer's experience and know-how and was basically a trial and error process. The design was guided by empirical rules and some empirical methods were available to roughly predict the performance of a ship. Tank tests were then a fundamental step to check and verify the design. Today, new tools are available to faster achieve the best design configuration. These are essentially numerical simulations and optimization methods, which have become extremely popular thanks to increasingly robust calculation codes and more extensive availability of computing power. These modern techniques may be regarded as the current state of the art in naval engineering and can be used to face several aspects of ship design. The main aspects to consider during the ship design process are resistance and propulsion, seakeeping and manoeuvring.

The resistance and propulsion fields regard the analysis of the mechanisms dealing with ship resistance, the design of the propeller and the study of the interaction between the hull and the propeller. Seakeeping is about the dynamical behaviour of the ship: it includes the study of ship performance in rough seas, the structural design of the ship with respect to loads in seaways and other aspects regarding ship safety such as capsizing, large roll motions and accelerations, wave impact on superstructures and propeller performance in difficult sea conditions. Finally, manoeuvring concerns the ability of the ship to keep the course and to react if changes of direction or speed are required. In [1] many examples where all these aspects are studied by using numerical simulations are provided.

This thesis is focused on ship resistance and on techniques to reduce it according to some modern design methods. The proposed design procedure is then applied to a practical case, the DTMB 5415 hull [24]. More specifically, a numerical simulation is validated to predict the hull's drag and an optimization is implemented to improve the ship's performance. In the literature, several examples of this design approach can be found and different methods to accomplish each step are provided.

Many numerical codes have been used to predict resistance, both viscous and inviscid. The most common ones are potential codes or panel methods as they are faster and provide a good prediction of the wave-making resistance. They are used for example in [2], [3], [4], [5], [6], [7], [8], [9], [10]. However, also RANS codes – which are able to provide an accurate prediction of the total resistance – have already been used to deal with such kind of problems. Examples may be found in [11], [12], [13], [14], [15].

Concerning parametrization, in most papers, the Lackenby transformation is adopted as it is an efficient method to produce global hull shape variations. Other approaches are for example the analytical description of some curves [3] or the radial basis function method [4], [5]. The free form deformation technique is not yet very popular in naval applications, although it is versatile and efficient. It is adopted for example in [2] and [12]. In most works, constraints are introduced to keep the ship's main dimensions unmodified and often, a design of experiments is carried out to evaluate the influence of design variables on the ship's resistance.

The optimization is usually performed by using a genetic algorithm, but also other optimization methods can be found. In [4] and [9], an artificial bee colony and a particle swarm are used. In [2] the simulated annealing algorithm is adopted, whereas the sequential quadratic programming method (SQP) is used in [13], [15] and [10]. These algorithms are often run over surrogate models. The most common ones are neural networks [6] [7], Kriging models [2] [12] and polynomial models [3] [14]. The percentage reduction of ship resistance achieved by using these optimization techniques goes on average from 5% to 15%.

The purpose of this thesis is to develop a flexible and efficient method to improve the ship's resistance performance. Through the chapters, different approaches to realize each design stage are presented, discussing advantages and drawbacks. Then, the following methods have been selected and applied to the DTMB 5415 case: the InterFoam RANS solver available in OpenFOAM has been chosen to perform the CFD analyses; the hull geometry has been parametrized in CAESES by using the free form deformation method for the bulb and a conventional method based on NURBS curves for the stern; then, a design of experiments based on the Sobol sampling technique and on the analysis of variance method, available in R, has been performed; finally, three surrogate models – a neural network, a polynomial model and a Kriging model – are built in MATLAB with the results of the design of experiments and used to run a genetic algorithm.

Introduction

CHAPTER 1

THE PHYSICS OF THE PROBLEM

One of the first questions that arise when dealing with ship design is to predict ship resistance in order to estimate the fuel consumption. In particular this is of primary and fundamental importance for big ships, like for example tankers, container-ships or bulk carriers, because in these cases even a little reduction in drag means saving a huge amount of fuel. This chapter goes through the mechanisms governing drag and the ways to measure and analyse each resistance component.

1.1 COMPONENTS OF CALM WATER RESISTANCE

The resistance experienced by a ship is made up of many components. Some of them are calm water resistance, rough water resistance, air resistance of hull and superstructure, appendages drag and roughness as well as fouling of the hull. The most important component is calm water resistance, so this thesis focuses on how this component arises and on methods for its reduction.

Calm water resistance is in turn made up of several components. It is possible to split it according to the forces acting on the hull or to the mechanisms of energy dissipation. In the first case it is possible to distinguish between frictional and pressure resistance while in the second case between viscous and wave resistance. This breakdown is shown in Figure 1.1 and Figure 1.2. The words "resistance" and "drag" are from now on used to define the calm water component of total resistance.

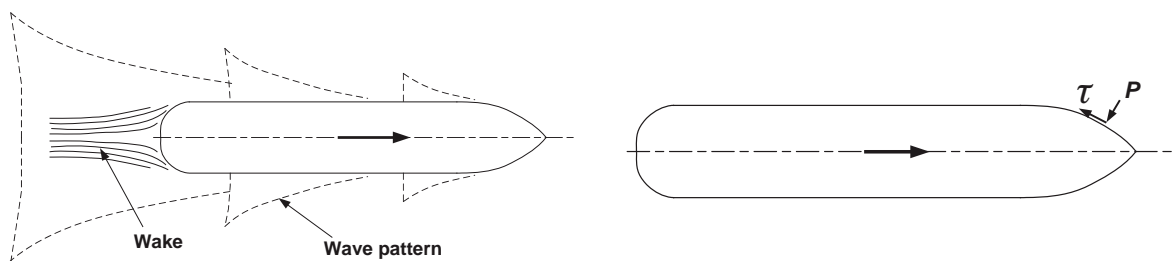


Figure 1.1: On the left mechanisms of energy dissipation, on the right forces acting on the hull [16].

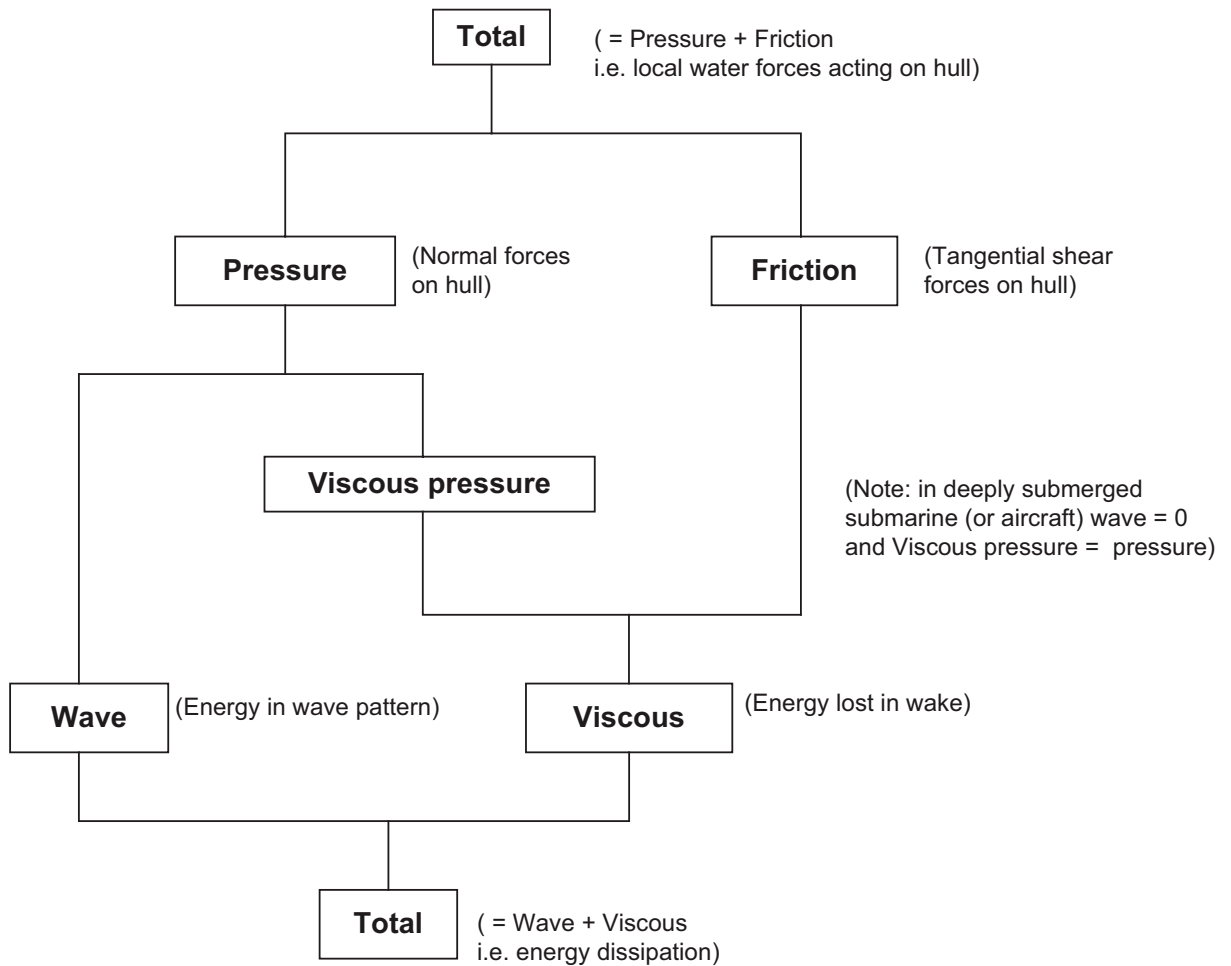


Figure 1.2: Calm water resistance decomposition into components [16].

- FORCES ACTING ON THE HULL:

Pressure resistance is due to the components of the hydrodynamical forces that act normal to each element of the hull surface and it can be calculated by integrating the components of these forces which are parallel to the moving direction of the ship. Instead, *frictional resistance* is due to the tangential stresses acting over the hull surface and it can be calculated by integrating the components of these forces which are parallel to the moving direction of the ship.

Frictional resistance is caused by the viscosity of the fluid while pressure resistance is due to the hull's wave-making but also to viscous effects. This last component of pressure resistance is called *viscous pressure resistance*.

It is possible to make a parallel between a ship and a body which is moving completely immersed in a fluid. When a submerged body travels through a fluid, like for example an airplane or a submarine, there is no wave-making effect but the resistance experienced by the body will be higher than just the frictional drag. In fact, the additional resistance component appears because the shape of the immersed body causes pressure variations in the flow field which result in turn in a higher value of

the integral of the shear stresses over the body. This is the so-called viscous pressure resistance.

- MECHANISMS OF ENERGY DISSIPATION:

Viscous resistance is due to viscous losses caused by the growth of a boundary layer around the hull surface and the appearance of a wake behind the ship, while *wave resistance* arises because the ship motion gives birth to a wave pattern and some power is spent to that end. Viscous resistance can also be seen as the sum of friction resistance and viscous pressure resistance.

Considering an ideal fluid with no viscosity, a deeply submerged symmetric body would have zero resistance because both the velocity and the pressure field would be perfectly symmetric. If this body is positioned on the free surface, the pressure field acting on the immersed part would cause changing in the water level and, therefore, the appearance of a wave pattern. This phenomenon requires the expense of some energy, causing the body to undergo a non zero resistance. Exactly the same happens in the case of a ship moving on the water free surface: this is a simple and intuitive explanation of why there is a wave-making resistance component in the ship drag.

1.2 WAVE-MAKING COMPONENT OF THE DRAG

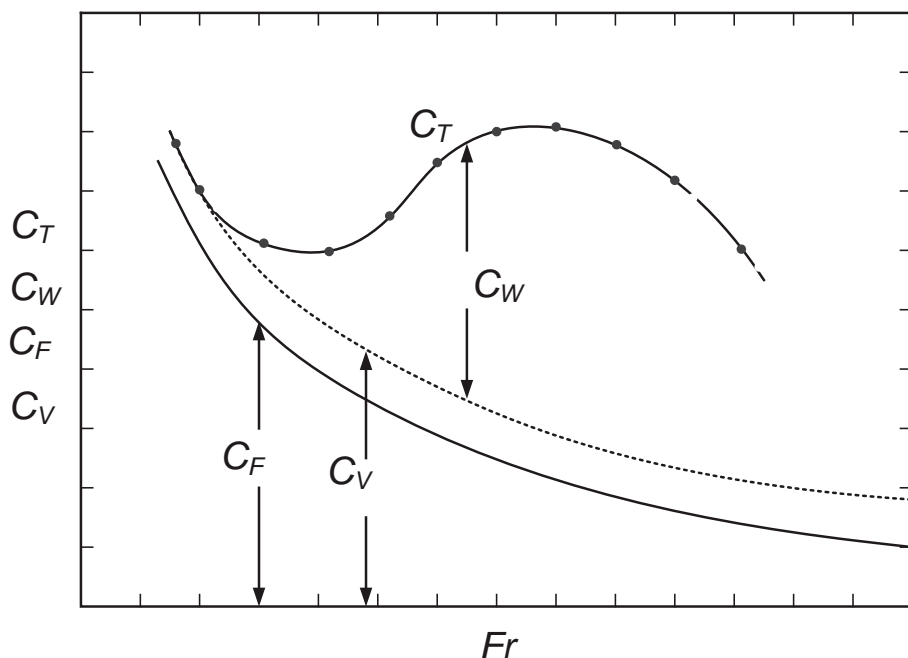


Figure 1.3: Breakdown of the resistance as a function of the Froude number Fr : c_T is the total drag coefficient, c_W is the wave resistance coefficient, c_F is the friction resistance coefficient, c_V is the viscous resistance coefficient. These quantities will be defined throughout the chapter [16].

Figure 1.3 provides a cross section of the components of hull's resistance. It can be noticed that friction and wave resistances are the main components. As will be seen in Section 1.3.3, friction resistance depends on the Reynolds number, that is on ship's length and speed, and obviously on surface characteristics. Hence the shape of the hull does not influence this component of the drag and the only way to reduce it is by changing the hull's material and improving surface finish by adding for example a coating layer.

Instead the wave-making component of the drag is strongly influenced by ship's geometry and, therefore, it can be reduced by working on this issue. This section analyses in greater detail what the mechanisms governing wave resistance are and how this component of the total drag is influenced by the hull shape. The wave pattern generated by the motion of the ship consists of two wave systems.

- PRIMARY WAVE SYSTEM:

As mentioned in Section 1.1, considering a ship moving completely immersed in water, it is possible to imagine the resulting flow field. As in the case of an airplane or more simply a wing, in some regions the flow accelerates causing a pressure decrease while in some others the flow slows down and the pressure increases. The same thing happens for a ship moving at the free surface: its motion modifies the pressure field. However in this case, according to Bernoulli's law, this modification leads to an increase of the free surface height in some regions and to a decrease of it in some others. This is the so-called *primary wave system* which is characterized by wave crests at the ship's ends, where the pressure is higher, and a long wave trough along the middle, where the pressure is lower.

The shape of this wave system, that is the locations of maxima and minima, does not depend on the hull's speed while the amplitude of crests and troughs depends quadratically on it. Obviously this wave system is strongly dependent on the hull's shape.

- SECONDARY WAVE SYSTEM:

It consists of a wave pattern composed of transverse and divergent waves which propagate downstream bounded by an angle α . In deep water α is independent of the hull's shape and it stands at 19.471° . This system is also called *Kelvin wave pattern* from the name of the well-known scientist who first studied this phenomenon.

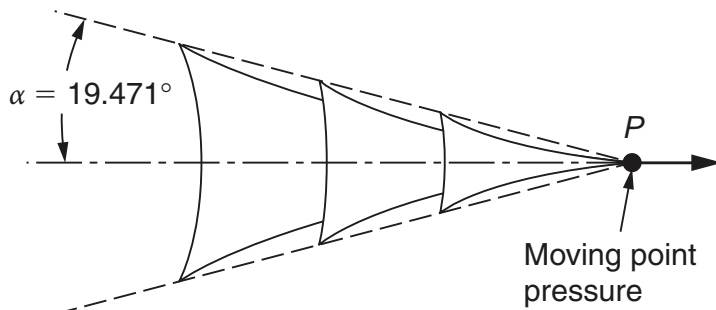


Figure 1.4: The so-called "Kelvin wave" model: the wave is created by a travelling pressure point. Adapted from [17].

The Kelvin wave is defined as a wave system created by a pressure point source travelling at the free surface, as it is shown in Figure 1.4. The wave pattern of a ship is composed of the superposition of many Kelvin waves which are produced by geometry discontinuities of the hull and interfere with each other. This can be seen in Figure 1.5.

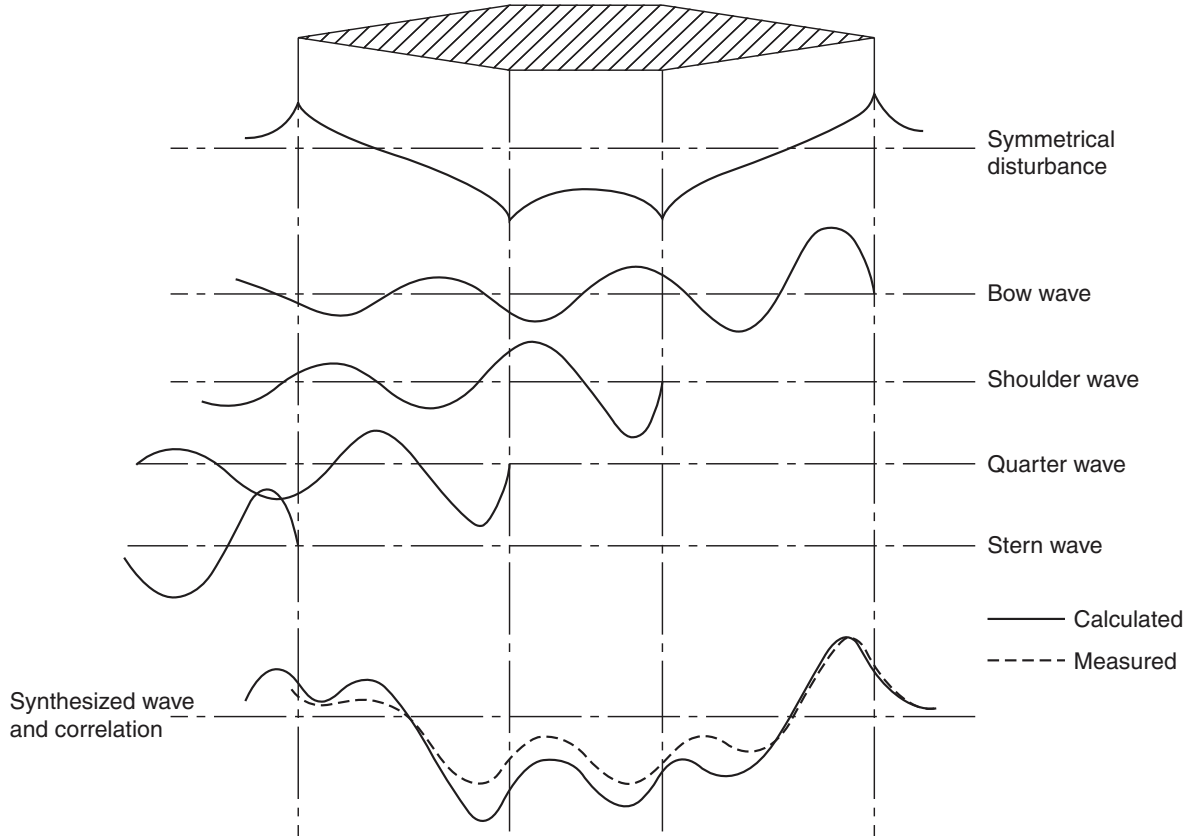


Figure 1.5: Secondary wave pattern generated by a simple body [17]. Each elementary wave can be found by using the "Kelvin wave" model.

In a ship based reference frame, waves are steady if the ship moves steadily. Equation 1.1 defines the wavelengths λ of the transversal waves composing the Kelvin wave pattern.

$$\lambda = \frac{2\pi V^2}{g} \quad 1.1$$

where V is the ship speed and g is the gravity acceleration. This wavelength is the fundamental wavelength of the secondary wave system. The wavelength of each other wave of the pattern is lower than the fundamental and it depends on the propagation angle of the wave according to the following relation:

$$\lambda_i = \frac{2\pi V_i^2}{g} = \frac{2\pi V^2 \cos \theta_i^2}{g} \quad 1.2$$

Here λ_i , V_i and θ_i are the wavelength, the speed and the propagation angle of the i -th wave of the system. The angle θ_i ranges from zero, in the case of transversal waves, and α , in the case of the most open diverging wave. According to 1.2, the wavelength reaches its maximum value for $\theta_i = 0$, that is in the case of a transversal wave. These equations also show that the relation linking the ship speed V and the velocity of every wave of the Kelvin system V_i is:

$$V_i = V \cos \theta_i \quad 1.3$$

In equation 1.1 it can be noted that the fundamental wavelength λ of each Kelvin wave that composes the complete wave pattern is proportional to the square of the ship's speed, so at different Froude numbers, positive or negative interference of transversal waves is possible. For this reason wave resistance depends on the hull's velocity showing humps and hollows at different Froude numbers, as Figure 1.6 shows. Froude number will be introduced in Section 1.3.1, now suffice it to say that it is defined as:

$$Fr = \frac{V}{\sqrt{gL}} \quad 1.4$$

where L is the ship's length.

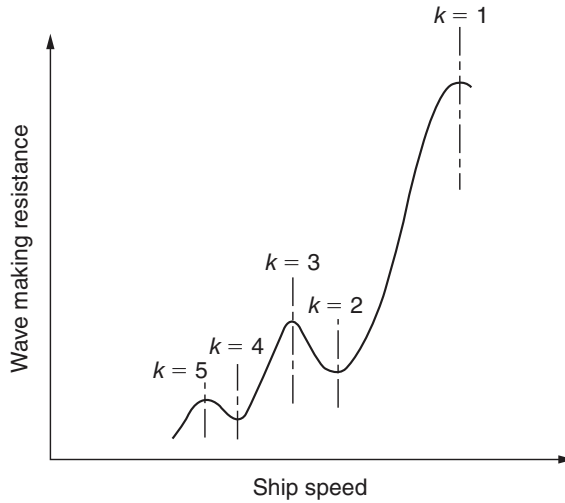


Figure 1.6: Trend of wave resistance depending on the Froude number [17].

It follows that in ship design, once the length of the hull has been established, the cruising speed has to be set to guarantee a favourable cruising Froude number. Vice versa if a certain cruising speed is imposed, ship length has to be adjusted to guarantee a favourable cruising Froude number. In particular, positive interference between bow and stern transversal waves occurs when:

$$L - \frac{\lambda}{4} = k \frac{\lambda}{2} \quad k = 1, 3, 5, \dots \iff \frac{\lambda}{L} = \frac{4}{2k+1} = \frac{2\pi V^2}{gL} = 2\pi Fr^2 \quad 1.5$$

From equation 1.5 it is possible to deduce the values of the Froude number that lead to a reinforcement of the transverse wave pattern at the stern: large waves will be formed in that region.

In the same manner, values of the Froude number for which a negative interference occurs may be determined. The relation is the same as 1.5 but in this case $k = 2, 4, 6, \dots$. This leads to the following result:

$$Fr = \sqrt{\frac{2}{\pi(2k+1)}} \quad k = \begin{cases} 1, 3, 5, \dots & \text{positive interference} \\ 2, 4, 6, \dots & \text{negative interference} \end{cases} \quad 1.6$$

Using equation 1.6 it is possible to obtain the favourable and unfavourable values of the Froude number, which are reported in Table 1.1. In Figure 1.7 it is possible to observe the corresponding wave interference.

k	$Fr[-]$	Description
1	0,461	First hump in R_W
2	0,357	First hollow in R_W
3	0,301	Second hump in R_W
4	0,266	Second hollow in R_W
5	0,241	Third hump in R_W
...

Table 1.1: Froude number calculated with equation 1.6 for different values of k [17]. R_W is the wave resistance.

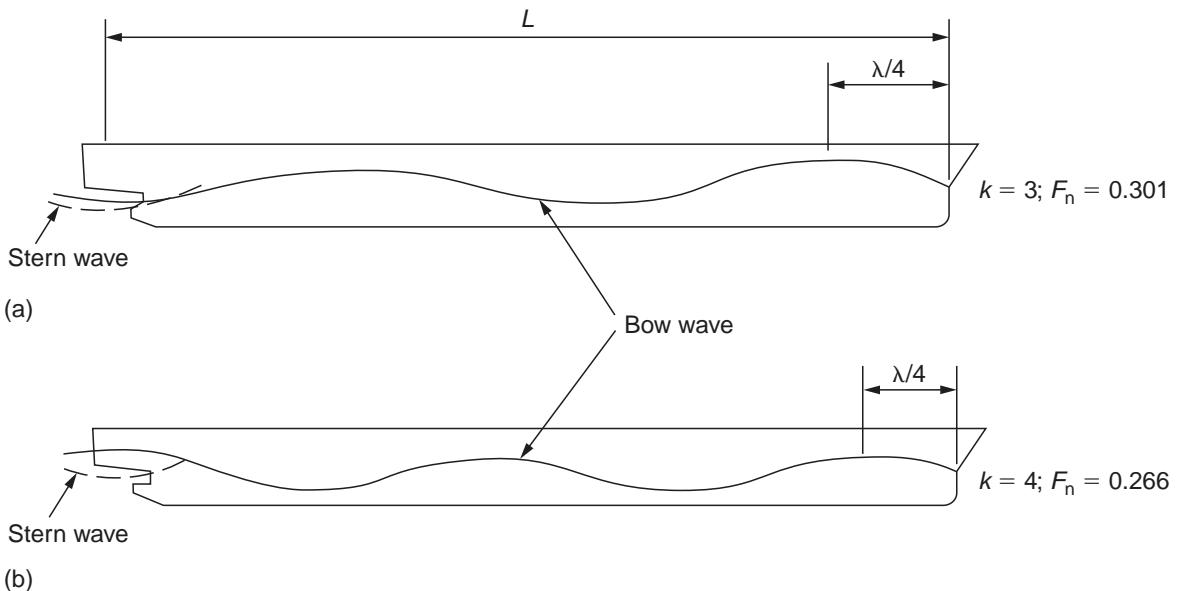


Figure 1.7: Wave interference at favourable and unfavourable Froude numbers [17].

1.2.1 THE BULBOUS Bow

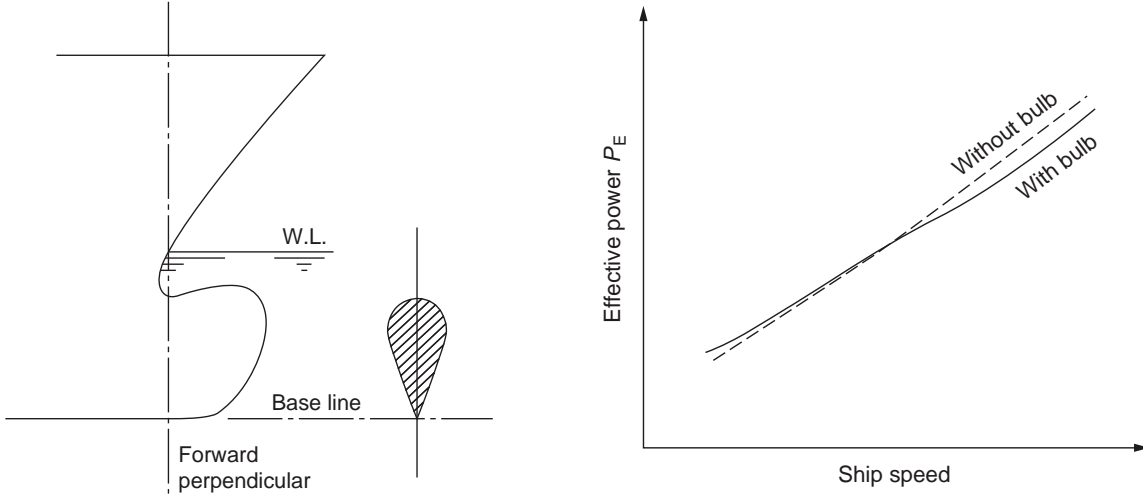


Figure 1.8: On the left the bulbous bow, on the right its influence on the ship's resistance. Adapted from [17].

The bulbous bow is a particular expedient developed at the beginning of the 20th century to obtain a reduction in the wave resistance. Its traditional shape and impact on ship resistance are depicted in Figure 1.8. This device appeared for the first time in 1912 in the US navy but its applications in merchant ships dates back to the late 1950s and early 1960s [17]. The basic idea behind this technical feature is to induce a flow acceleration and, hence, a low pressure region. This can be interpreted as a low pressure wave which, interfering with the bow pressure wave, is able to reduce its amplitude and, therefore, the wave resistance.

In the previous section, it has been explained that the wave interference phenomenon is strongly dependent on the ship's speed and that for a certain geometry of the hull there are favourable and unfavourable speeds. Hence, it is possible to deduce that the presence of a bulb is convenient and brings advantages only within a restricted range of ship velocities. For this reason, bulbs are usually adopted in ships that have a well defined cruise speed. Moreover in general the reduction in ship resistance can be appreciated only at high velocities, where the wave resistance component is high, because the introduction of the bulbous bow causes also an increase of the frictional resistance which prevails at low speeds.

Other effects of the bulb are the introduction of a downward velocity component near the bow, a modification of the overall flow field with possible consequences on the propeller's performance and a change in the wave breaking phenomenon. The shape of the bulb is particularly important in determining its beneficial effect and today it is still the subject of intense studies.

1.2.2 THE TRANSOM STERN

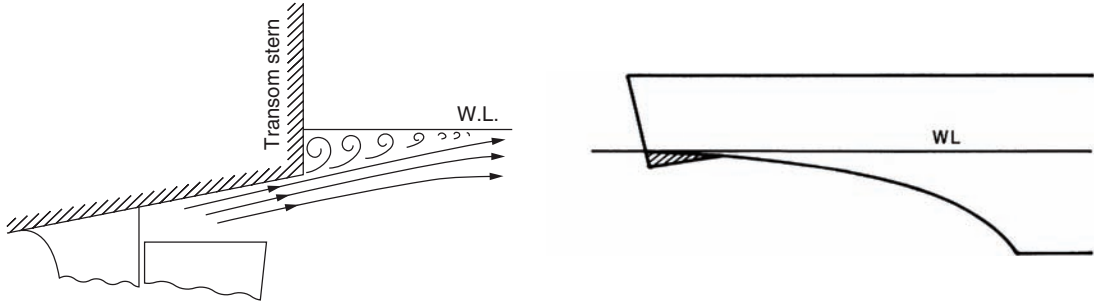


Figure 1.9: On the left, transom stern geometry and behaviour at low speeds: vortices are generated behind the stern causing pressure losses [17]. On the right, example of wedge used in transom sterns to create a downward component of velocity in the flow field, adapted from [18].

The transom stern is a particular type of stern which has been introduced to simplify construction and improve performance of fast ships. It is characterized by a flat shape extending to the waterline, as can be observed on the left hand side of Figure 1.9. This kind of stern presents a higher resistance than an equivalent conventional cruiser stern at low speeds but shows favourable resistance characteristics at high speeds. In fact at low velocities the transom is submerged in water, which means a higher wetted surface, and the flow separates because of the sharp edge. This causes vortices and pressure losses leading to an increase of the ship's resistance. Instead at high velocities, ship's performance improves because the flow breaks cleanly from the transom corner: the stern region, which is wet at low speeds, becomes dry. This brings to a reduction of friction resistance because of a smaller wetted surface. Moreover, in [19] O'Dea et al. write: *the depression in the free surface behind the transom acts as a fictitious extended afterbody. This fictitious afterbody increases the effective hull length for generating wave drag and thus reduces the effective Froude number, but without any frictional drag penalty for this extended length.*

Hence the transom stern improves the hydrodynamical behaviour of the ship at high speeds. However today these mechanisms are not yet well understood because the turbulent flow field in the forebody area is not simple to study and analyse performing tank tests and CFD simulations.

The transom stern influences positively also the dynamic configuration of the ship since it causes a reduction of the trim angle. To enhance this aspect, usually the so-called *stern wedge* is added to the stern corner. This geometric feature, shown on the right hand side of Figure 1.9, modifies the flow field by creating a downward velocity component which reduces the height of the first stern wave and the associated energy loss. However this downward velocity component presses the bow deeper into water at high speeds, worsening the ship's seakeeping behaviour. Hence transom stern has to be designed carefully and a lot of factors have to be taken into account.

1.3 FROUDE S ANALYSIS PROCEDURE

1.3.1 SIMILARITY LAWS FOR MODEL TESTS

It is not straightforward how to estimate the hull's resistance and there are a lot of options to do it. Basically it is possible to divide them into three groups: empirical/statistical, experimental and numerical approaches. Certainly experimental methods, based on model or full-scale tests, give the most precise estimation but they are expensive and time costing. On the other hand, empirical approaches are faster but less accurate. They can be useful to have an idea about the order of magnitude of the drag in the first stages of the design process. Finally numerical methods, often based on CFD simulations, are precise enough, inexpensive but time consuming. Nonetheless experimental tests are fundamental both to develop an empirical or statistical method and to validate a CFD analysis.

In the case of a scaled model test, it is important to understand how the results obtained for the model can be transferred to a full-scale hull by a proportionality factor. From here on the symbols s and m refer to the full-scale ship and to the model respectively.

- GEOMETRIC SIMILARITY:

The scale factor λ is introduced for length quantities:

$$L_s = \lambda L_m \quad A_s = \lambda^2 A_m \quad \nabla_s = \lambda^3 \nabla_m \quad 1.7$$

In the third of 1.7, ∇ denotes the volume of water displaced by the hull.

- KINEMATIC SIMILARITY:

The scale factor τ is introduced for time quantities:

$$t_s = \tau t_m \quad 1.8$$

Therefore the following relations are deduced for velocities and accelerations:

$$V_s = \frac{\lambda}{\tau} V_m \quad a_s = \frac{\lambda}{\tau^2} a_m \quad 1.9$$

- DYNAMICAL SIMILARITY:

The scale factor k is introduced for forces:

$$F_s = k F_m \quad 1.10$$

It is possible to deduce for k the following expression depending on λ and τ which is called Newton's law of similarity.

$$k = \frac{F_s}{F_m} = \frac{m_s a_s}{m_m a_m} = \frac{\frac{s}{m} \nabla_s a_s}{\frac{s}{m} \nabla_m a_m} = \frac{\frac{s}{m} \lambda^4}{\frac{s}{m}} \quad 1.11$$

By rearranging equation 1.11 the following result can be obtained:

$$k = \frac{\frac{s}{m} \lambda^2}{\frac{s}{m}} = \frac{\frac{s}{m} A_s}{\frac{s}{m} A_m} \frac{\frac{V_s}{V_m}}{\frac{V_s}{V_m}} = \frac{\frac{1}{2} s c_s A_s V_s^2}{\frac{1}{2} m c_m A_m V_m^2} \quad 1.12$$

In 1.12, $F = \frac{1}{2} cAV^2$ is the expression of a generic hydrodynamic force and c_s and c_m are the drag coefficients of a full-scale ship and its scaled model. It follows that if Newton's similarity law is fulfilled, the drag coefficient is constant for both the ship and the model and vice versa.

1. Inertial and gravity forces:

For the gravity force, k coefficient can be calculated as:

$$k_g = \frac{G_s}{G_m} = \frac{\frac{s}{m} \nabla_s}{\frac{s}{m} \nabla_m} = \frac{\frac{s}{m} \lambda^3}{\frac{s}{m}} \quad 1.13$$

k_g is the dynamical scale factor k in the case of gravity force. Both equations 1.13 and 1.11 have to be fulfilled. So, imposing $k = k_g$:

$$\lambda^3 = \frac{\lambda^4}{2} \iff \lambda = \sqrt{\lambda} \quad 1.14$$

Equation 1.14 can be inserted into the first of 1.9 and the following relation can be deduced:

$$\frac{V_s}{V_m} = \sqrt{\lambda} = \sqrt{\frac{L_s}{L_m}} \iff \frac{V_s}{\sqrt{L_s}} = \frac{V_m}{\sqrt{L_m}} \quad 1.15$$

From this, the Froude number is defined as:

$$Fr = \frac{V}{\sqrt{gL}} \quad 1.16$$

In a system where gravity and inertia are the only forces acting, if the full-scale ship and the model share the same Froude number the dynamical similarity is ensured and the wave pattern will be geometrically similar (the gravity acceleration g is the same both the ship and the model). This is true for small non-breaking waves, where other physical mechanisms like surface tension or viscous effect are negligible.

2. Inertial and frictional forces:

Frictional forces can be expressed as:

$$R = \frac{u}{n} A \quad 1.17$$

where the partial derivative is the velocity gradient normal to the flow direction, μ is the dynamic viscosity and A is the area subject to the frictional stresses. As before, it is possible to evaluate the dynamical scale factor k in the case of frictional forces:

$$k_f = \frac{R_s}{R_m} = \frac{\frac{s}{m} \lambda^2}{\frac{s}{m}} \quad 1.18$$

Imposing $k = k_f$, the following relation is deduced:

$$\frac{\frac{s}{m} \lambda^4}{\frac{s}{m}^2} = \frac{\frac{s}{m} \lambda^2}{\frac{s}{m}} \quad 1.19$$

By making use of the relation $\mu = \rho / \eta$ between dynamic viscosity, cinematic viscosity and density, from equation 1.19 it follows:

$$\frac{\frac{s}{m}}{\frac{s}{m}} = \frac{\lambda^2}{\frac{V_s L_s}{V_m L_m}} \iff \frac{V_s L_s}{s} = \frac{V_m L_m}{m} = Re \quad 1.20$$

In 1.20 Re is the Reynolds number. This last relation means that in a system where friction and inertia are the only forces acting, if the Reynolds number is constant for both the ship and the scaled model, the dynamical similarity is ensured.

During experimental tests, the equality between the ship's and the model's Froude numbers is easy to achieve. If for example the geometrical scale factor λ is set to 25, which means that the model is twenty-five time smaller than the full-scale ship, to fulfil Froude's similarity law it is sufficient to reduce the model's velocity by a scale factor of 5, as can be deduced from equation 1.16.

On the contrary, to fulfil Reynold's law with the same geometrical scale factor of 25, the model's velocity would have to be set 25 times larger than the full-scale ship's speed, as can be seen in equation 1.20 and this is not so straightforward.

In naval applications, both gravity and frictional forces are not negligible, thus in model tests both Froude's and Reynolds' laws should be fulfilled at the same time. In practice this is not possible. As a matter of fact if the geometrical scale factor is set as before to 25 and the model's speed is scaled down by a factor of 5 to ensure the compliance to Froude's law, the only way to achieve also the equality between the ship's and the model's Reynolds numbers would be to modify the viscosity of the fluid in the tank where the tests are performed, as suggested by the following equation, and this is obviously infeasible.

$$\frac{Re_s}{Re_m} = \frac{\frac{L_s}{L_m}}{\frac{s}{m}}^3 = \frac{\frac{m}{s} \lambda^{1.5}}{\frac{s}{m}} = 1 \quad 1.21$$

So model's tank tests are usually performed at the same Froude number of the full-scale ship while Reynolds' similarity law cannot be fulfilled: Reynolds number of the model is much smaller than the Reynolds number of the full-scale ship. A solution to this problem when the full-scale ship drag coefficients have to be deduced from the model's one, is given in Section 1.3.3.

1.3.2 DIMENSIONAL ANALYSIS

Using the dimensional analysis method it is possible to reach the same results achieved in the previous section. The quantities involved in the problem are the followings:

Hull resistance	R_T	$\frac{ML}{T^2}$
Hull speed	V	$\frac{L}{T}$
Hull size	L	L
Fluid density		$\frac{M}{L^3}$
Fluid viscosity		$\frac{M}{LT}$
Gravity acceleration	g	$\frac{L}{T^2}$

Table 1.2: Quantities and dimensions involved in the dimensional analysis for naval applications [16].

The relationship between the quantities may be expressed as:

$$f(R_T, V, L, \alpha_1, \alpha_2, \alpha_3, g, \alpha_i) = 0 \iff R_T = f(V, L, \alpha_1, \alpha_2, \alpha_3, g, \alpha_i) \quad 1.22$$

where α_i are adimensional parameters of the hull's shape. Dimensional analysis leads to:

$$\frac{R_T}{L^2 V^2} = f(Re, Fr, \alpha_i) \iff c_T = f(Re, Fr, \alpha_i) \quad 1.23$$

where c_T is the drag coefficient of the hull defined as follows:

$$c_T = \frac{R_T}{\frac{1}{2} SV^2} \quad 1.24$$

and S is the hull's wetted surface area.

Equation 1.23 means that the complete dynamic similarity between two ships is ensured if the ships are geometrically similar and if they share the same Reynolds and Froude numbers. In the previous section it has been demonstrated that it is not possible to perform experimental tests keeping both Reynolds and Froude numbers constant and that it is easier to fulfil Froude's similarity law rather than Reynolds' similarity law.

Equation 1.23 can be rewritten as:

$$c_T = f(Re) + f(Fr) + f(Re, Fr) \quad 1.25$$

Here the drag of the hull is divided into three terms. The first depends on the Reynolds number and can be associated with the viscous component of the hull's resistance. The second, which depends on the Froude number, relates to the wave-making component of the hull's resistance. The third term depends on both numbers because, as has been said in Section 1.1, a total breakdown of resistance into components is not possible. In

fact wave resistance is not totally independent of Re and viscous resistance is not totally independent of Fr . Nevertheless this third term is negligible. Therefore performing a model tank test at the same Froude number of the full-scale ship, leads to a reasonably good estimation of the pressure resistance and of the shape of the wave pattern.

1.3.3 SCALING OF THE RESISTANCE COEFFICIENT

The drag coefficient of the hull c_T can be broken down into two terms as follows:

$$c_T = c_F + c_R \quad 1.26$$

where c_F is the skin friction drag coefficient while c_R is called *residuary drag coefficient* and it takes into account all the rest, which is mainly wave-making and pressure form resistances.

In Section 1.3.1 it has been said that if Froude's similarity law is fulfilled, the drag coefficient associated to the wave-making resistance is constant for both the ship and the model. Hence, as in experimental tests model's and ship's Froude numbers are the same, the residuary drag coefficient is constant. Instead, skin friction coefficient depends on the Reynolds number and in tank tests Reynolds number is not the same for the model and the ship. Therefore another approach to estimate this component of the drag is needed.

The most currently used method to evaluate c_F is the ITTC 1957 formula reported in 1.27 which is an empirical correlation based on the curve in Figure 1.10.

$$c_F = \frac{0.075}{\log_{10} Re - 2^2} \quad 1.27$$

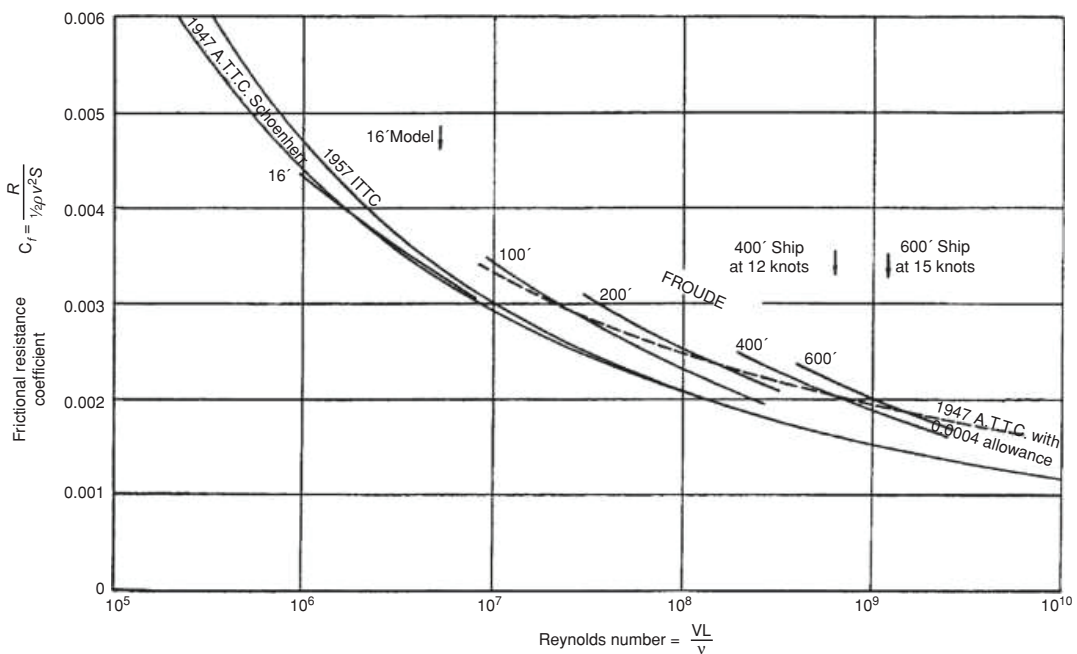


Figure 1.10: Skin friction resistance coefficient [16].

Tank tests give as a result an estimation of the total drag coefficient c_{Tm} of the model. From this it is necessary to deduce the total drag coefficient c_{Ts} of the full-scale ship. The relations involved are the followings:

$$c_{Tm} = c_{Fm} + c_{Rm} \quad c_{Ts} = c_{Fs} + c_{Rs} \quad 1.28$$

Since it has been said that $c_{Rs} = c_{Rm}$, equations 1.28 lead to:

$$c_{Tm} - c_{Ts} = c_{Fm} - c_{Fs} \iff c_{Ts} = c_{Tm} - (c_{Fm} - c_{Fs}) \quad 1.29$$

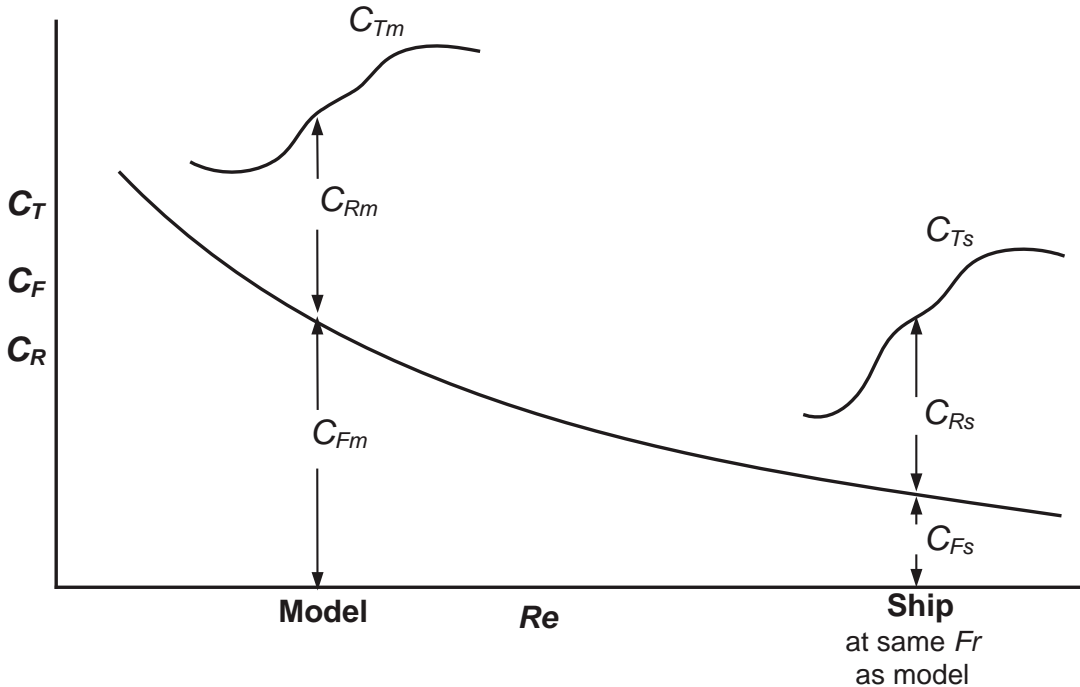


Figure 1.11: Model-ship extrapolation procedure according to Froude's approach [16].

This procedure to deduce the ship's resistance is depicted in Figure 1.11. A better approximation of c_T can be achieved by using Hughes' form factor approach. The procedure is the same as before, but the partition of resistance components, that is equation 1.26, changes. Here the drag is broken down as follows:

$$c_T = c_V + c_W \quad 1.30$$

where c_V and c_W are the viscous and wave-making resistance coefficients.

In this case if Froude's similarity law is fulfilled, c_W is the same for the model and the ship while c_V has to be estimated in some other way. The coefficient c_V can be expressed as:

$$c_V = (1 + k)c_F \quad 1.31$$

In equation 1.31 c_F is the skin friction resistance coefficient and k is a form factor which depends on the hull's form and may be derived from low-speed tests. In fact, at low Fr , wave resistance coefficient c_W tends to zero and it follows:

$$(1 + k) = \frac{c_{Tm}}{c_{Fm}} \quad 1.32$$

The total resistance coefficient of the full-scale ship may be deduced with a relation similar to equation 1.29:

$$c_{Ts} = c_{Tm} - (1 + k)(c_{Fm} - c_{Fs}) \quad 1.33$$

This procedure to evaluate the hull drag is schematically shown in Figure 1.12. However this method is more complex and less used.

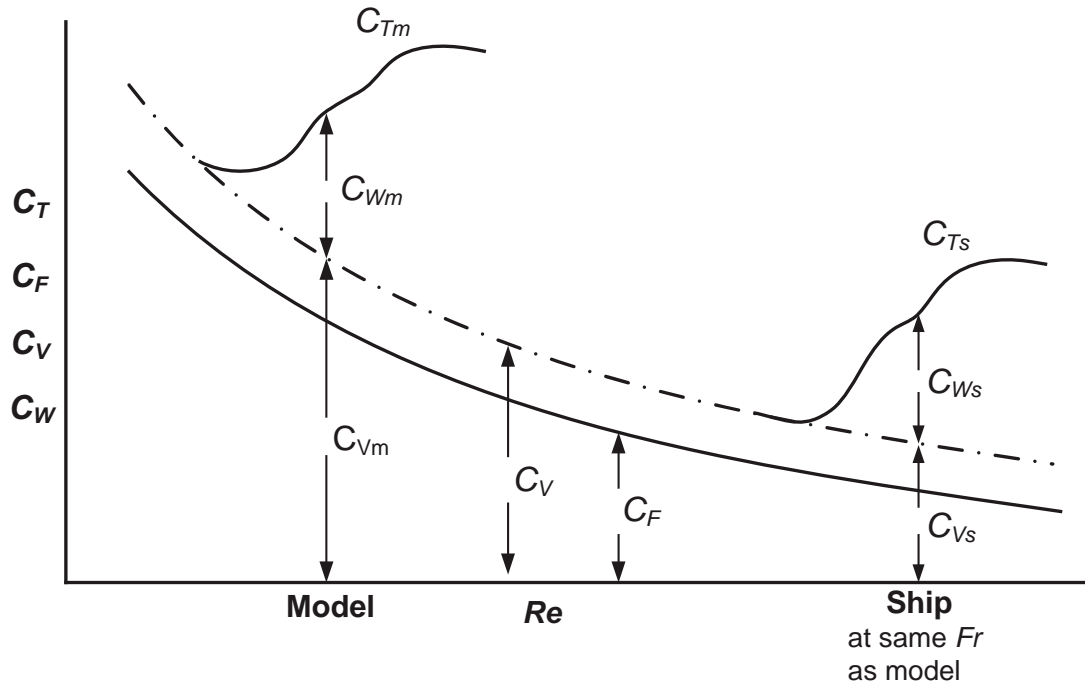


Figure 1.12: Model-ship extrapolation procedure according to Hughes' approach [16].

1.4 CONCLUSIONS

In this chapter the physics of the problem is provided. The chapter is divided in two parts. In the first one, the attention is focused on the most important resistance component – calm water resistance – and on its underlying phenomena. In the second one, similarity laws for naval applications, which are needed to refer model's data to a full-scale ship, are introduced.

Calm water resistance can be analysed according to the forces acting on the hull or to the mechanisms of energy dissipation. In the first case it is possible to distinguish between frictional and pressure resistance, while in the second case between viscous and wave resistance. Frictional and wave-making resistance are the main components of the ship drag. The first depends on the Reynolds number and on surface characteristics, hence it cannot be easily reduced. Instead, the second can be decreased optimizing the hull's shape.

The wave-making resistance component is due to the wave pattern which forms around the ship through the expense of some energy. This wave pattern consists of a primary and a secondary wave system. The former one is caused by the non-uniform pressure field around the moving hull and it is characterized by wave crests at the ship's ends, where the pressure is higher, and a long wave trough along the middle, where the pressure is lower. The shape of this wave system, that is the locations of maxima and minima, does not depend on the hull's speed while the amplitude of crests and troughs depends quadratically on it. The secondary wave system results from the superposition of several Kelvin waves. These, in turn, are composed of transverse and divergent waves which propagate downstream bounded by an angle α . The Kelvin waves are produced by geometry discontinuities and interfere with each other. More specifically, the fundamental wavelength λ of each Kelvin wave is proportional to the square of the ship's speed. Therefore at different velocities, positive or negative interference is possible. For this reason wave resistance depends on the ship's speed, showing humps and hollows at different Froude numbers. Two geometrical details have a particular influence on the wave-making resistance: the bulbous bow and the transom stern.

Several methods are available to predict the ship's drag. The most commonly used are statistical approaches, CFD analyses and experimental tests. The latter ones, however, are fundamental both to develop a statistical method and to validate a numerical model and are usually performed by using a scaled model of the ship: it is important to understand how the results obtained for the model can be transferred to the full-scale ship. This can be done by means of the similarity laws, which can be summarized as follows. The dynamic similarity is ensured if the full-scale ship and the model share the same:

- Froude number, in a system where gravity and inertia are the only forces acting;
- Reynolds number, in a system where friction and inertia are the only forces acting.

In naval applications, both gravity and frictional forces are not negligible, thus in model tests both Froude's and Reynolds' laws should be fulfilled at the same time. In practice this is not possible. Model's tank tests are usually performed at the same Froude number

of the full-scale ship while Reynolds' similarity law cannot be fulfilled. As a consequence, the wave resistance coefficient of the full-scale ship is equal to the model's one, while other approaches are needed to estimate the friction resistance coefficient. The most currently used are the ITTC 1957 empirical formula and the Hughes' statistical method.

CHAPTER 2

CFD ANALYSES FOR NAVAL APPLICATIONS

Nowadays CFD simulations are currently used during the ship design process as they can replace model tests saving a lot of time and allowing a deeper study of the ship's performance. These techniques have become extremely popular over recent years thanks to increasingly robust calculation codes and more extensive availability of computing power. A lot of different analysis can be performed: viscous or inviscid, steady or unsteady, simulations which involve one or more degrees of freedom and so on. Each of these analysis has advantages and disadvantages and the designer will choose the more convenient to solve the problem under examination. Various tools are available to carry out the simulations: commercial codes and also some open source solver. In this chapter a brief summary of fluid dynamics' laws is carried out focusing in particular on the numerical approaches used in naval applications. Then the CFD open source code OpenFOAM, used to analyse the case study of this thesis, is introduced.

2.1 THEORY: EQUATIONS INVOLVED

The main fluid ship designer deals with in naval applications is obviously water, which is an incompressible fluid: the density ρ can be assumed constant and it is possible to adopt the theory developed for incompressible fluids. Considering an incompressible fluid which is moving through an infinitely small control volume, its behaviour can be described by using two fundamental laws of the fluid dynamics: the continuity law and the conservation of momentum. Instead, the study of a compressible fluid would require also the energy conservation's law.

- CONTINUITY EQUATION:

The continuity equation states that any amount of fluid flowing into a control volume, also flows out of the control volume at the same time. In the two-dimensional case, Figure 2.1, this concept can be expressed analytically through the following relation:

$$-\frac{\partial u}{\partial y} + (u + u_x \frac{\partial u}{\partial x}) - \frac{\partial v}{\partial x} + (v + v_y \frac{\partial v}{\partial y}) = 0 \quad 2.1$$

where u and v are the components of the fluid velocity along x and y directions, the indices denote the partial derivative, for example $u_x = \frac{\partial u}{\partial x}$, and dx , dy are the

sides of the elementary control area. Simplifying the equation and considering the three-dimensional case, it is possible to get:

$$u_x + v_y + w_z = 0 \quad 2.2$$

where w_z is the partial derivative of the vertical component of fluid velocity w with respect to the z direction. This is the differential form of the continuity equation for an incompressible fluid. In the general formulation, an additional term appears, that is the substantial derivative of the density.

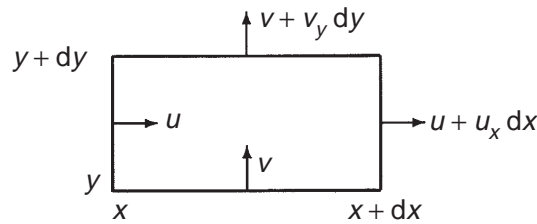


Figure 2.1: Two-dimensional fluid element model to define the continuity equation 2.1 [20].

- CONSERVATION OF MOMENTUM:

The conservation of momentum in the fluid moving through the control volume leads to:

$$\begin{aligned} (u_t + uu_x + vu_y + wu_z) &= f_1 - P_x + (u_{xx} + u_{yy} + u_{zz}) \\ (v_t + uv_x + vv_y + wv_z) &= f_2 - P_y + (v_{xx} + v_{yy} + v_{zz}) \\ (w_t + uw_x + vw_y + ww_z) &= f_3 - P_z + (w_{xx} + w_{yy} + w_{zz}) \end{aligned} \quad 2.3$$

where u_t is the derivative of the velocity with respect to time, f_1 , f_2 , f_3 are accelerations due to volumetric forces, P is pressure, ν is the kinematic viscosity of the fluid and the terms with two indices are the second order derivatives of the velocity components. The above relation can be expressed more briefly as follows:

$$\frac{U}{t} + \mathbf{U} \cdot \nabla \mathbf{U} = \mathbf{f} - \nabla P + \nabla^2 \mathbf{U} \quad 2.4$$

In this equation the term within brackets states physically that the velocity of the fluid element is changing as the element passes through a point because of two factors. The first factor, expressed by the time derivative which is called *source term*, is a fluctuation with time of the velocity itself. The second factor, summarized by the second term within brackets which is called *convective term*, is a velocity gradient in the fluid domain. The second order derivatives on the right hand side of the equation are the so-called *diffusion term*. The source term obviously disappears in the case of a steady problem.

The equation 2.3 or 2.4 is called *Navier-Stokes equation* from the names of Claude-Louis Navier (1785 – 1836), a French engineer and mathematician who first gave a differential description of incompressible flows, and George Gabriel Stokes (1819 – 1903), an Irish physicist who derived an analytical description of the problem.

2.1.1 REYNOLDS-AVERAGED NAVIER-STOKES EQUATIONS

The continuity equation together with the Navier-Stokes equations form a system of coupled, non-linear, partial differential equations. Until now there is no analytical solution to this system and a numerical approach is needed to solve fluid dynamical problems. Examples of numerical approach are the finite difference method, the finite element method or the the finite volume method. However today's computers are not powerful enough to allow either a numerical solution of the Navier-Stokes equations and so they have to be simplified in some way.

Velocities and pressures can be expressed as the sum of a time averaged term and a fluctuation term in order to describe statistically the effects of the turbulence. This brings to the following equations:

$$\begin{aligned} (u_t + uu_x + vu_y + wu_z) &= f_1 - P_x + (u_{xx} + u_{yy} + u_{zz}) - [(u u)_x + (u v)_y + (u w)_z] \\ (v_t + uv_x + vv_y + wv_z) &= f_2 - P_y + (v_{xx} + v_{yy} + v_{zz}) - [(u v)_x + (v v)_y + (v w)_z] \\ (w_t + uw_x + vw_y + ww_z) &= f_3 - P_z + (w_{xx} + w_{yy} + w_{zz}) - [(w u)_x + (w v)_y + (w w)_z] \end{aligned} \quad 2.5$$

where u, v, w, p are used to identify the time averages while u, v, w denote the fluctuation parts. In 2.5 the last terms on the right hand side are the derivatives of the so-called Reynolds stresses, so these equations are named *Reynolds-averaged Navier-Stokes equations* or more simply *RANS* equations. In fact, these terms are dimensionally equivalent to stresses.

The operation of averaging quantities over time is straightforward in the case of a steady problem while in the case of unsteady flows, fluctuations are averaged over a chosen time interval which is small compared to the global motions, but large compared to the turbulent fluctuations.

RANS equations need a turbulence model to estimate the Reynolds stresses terms. *Large-eddy simulations* or *LES* lie somewhere in between the original Navier-Stokes equations and the RANS equations, as they resolve the flow at a more detailed level by using turbulence models only to represent the smaller turbulent structures while the larger structures are resolved directly.

2.1.2 EULER AND LAPLACE EQUATIONS

There are some other ways to simplify the Navier-Stokes equations to solve a fluid dynamics problem.

- **EULER EQUATIONS:** Euler equations are derived from the RANS with the assumption of inviscid fluid. They can be expressed in the following form:

$$\frac{U}{t} + \mathbf{U} \cdot \nabla \mathbf{U} = \mathbf{f} - \nabla P \quad 2.6$$

These equations are commonly used in aerospace applications to study the flow field around a lifting object. Instead, they are not often used in ship design where potential solvers are preferred.

- **LAPLACE EQUATIONS:** The additional assumption of irrotational flow brings to the Laplace equation. A flow is said to be irrotational if its curl is equal to zero, which means:

$$\nabla \cdot \mathbf{U} = 0 \iff \frac{\partial u}{\partial x}, \frac{\partial v}{\partial y}, \frac{\partial w}{\partial z} = 0 \quad (u, v, w) = 0 \quad 2.7$$

The left hand side of equation 2.7 is also the definition of the vorticity, hence an irrotational flow has zero vorticity.

An irrotational inviscid flow is called *potential flow* because its velocity can be expressed as the gradient of a scalar function, the velocity potential ϕ , as follows:

$$u = \frac{\partial \phi}{\partial x}, \quad v = \frac{\partial \phi}{\partial y}, \quad w = \frac{\partial \phi}{\partial z} \iff \mathbf{U} = \nabla \phi \quad 2.8$$

These relations can be put in the continuity equation 2.2, leading to:

$$\frac{\partial^2 \phi}{\partial x^2} + \frac{\partial^2 \phi}{\partial y^2} + \frac{\partial^2 \phi}{\partial z^2} = 0 \iff \nabla^2 \phi = 0 \quad 2.9$$

which is the Laplace equation. Here three unknowns, the velocity components, are reduced to only one unknown, the potential ϕ , leading to a strong simplification of the problem. Moreover Laplace equation is linear: the flow can be seen as the superposition of elementary potential flows, as source, sink, dipole, vortices and so on, which have a known simple solution.

As for RANS equations, Euler and Laplace equations can be solved numerically as well. In cases where the viscosity of the fluid can be ignored, these equations lead to a satisfactory solution which is near to the solution provided by the RANS equation. However, they are often used as a first approach to solve also more complex fluid dynamical problems with the great advantage of a much shorter computing time. In fact, RANS equations require hours to resolve even a quite simple problem while Euler or Laplace equations can calculate the solution in few seconds.

2.1.3 TURBULENCE MODELS

As stated in Section 2.1.1, turbulence models are used in Reynolds-averaged Navier-Stokes equations to relate the turbulent stresses to the mean flow properties. The simplest procedure is based on the so-called Boussinesq approximation: turbulence is assumed to be isotropic and the Reynolds stresses are linked to the gradients of the average velocities through the turbulence kinetic energy $k = \frac{1}{2}(u^2 + v^2 + w^2)$ and a term called *eddy viscosity* τ_t as follows:

$$-\begin{matrix} u & u \\ u & v \\ u & w \end{matrix} - \begin{matrix} v & u \\ v & v \\ v & w \end{matrix} - \begin{matrix} w & u \\ w & v \\ w & w \end{matrix} = \tau_t \begin{matrix} 2u_x \\ u_y + v_x \\ u_z + w_x \end{matrix} - \begin{matrix} u_y + v_x \\ 2v_y \\ w_y + v_z \end{matrix} - \begin{matrix} u_z + w_x \\ w_y + v_z \\ 2w_z \end{matrix} - \begin{matrix} \frac{2}{3}k \\ 0 \\ 0 \end{matrix} - \begin{matrix} 0 \\ \frac{2}{3}k \\ 0 \end{matrix} - \begin{matrix} 0 \\ 0 \\ \frac{2}{3}k \end{matrix} \quad 2.10$$

The most commonly used models based on this approximation are the so-called $k - \epsilon$ and $k - \omega$ models where ϵ and ω , which are respectively the dissipation rate and the frequency of turbulence kinetic energy, are used to express the eddy viscosity term. In naval applications the $k - \epsilon$ model is usually preferred.

In the case of a wall bounded turbulent problem, turbulence models need to be adjusted in order to properly describe the behaviour of the flow near the wall. Often in these cases a wall function is coupled to the standard turbulence model. The simplest example is the wall function that imposes a logarithmic increase of the velocity with respect to the distance from the wall. Otherwise it is possible to modify the turbulence model by applying a no-slip condition directly at the wall. This approach requires a higher computational time but leads to a more accurate solution.

2.2 TWO-PHASES FLOWS

In the previous section, a brief summary of the principles and equations governing the behaviour of an incompressible flow have been presented. Usually the numerical method used to solve the flow through a volume surrounding an object is the so-called *finite volume method*. This approach is based on the discretization of the domain in a great number of elementary little volumes of fluid, which can be of different shapes. In other words, the domain is represented by a mesh made up of a lot of cells. The governing equations are then applied to each cell and the process is iterated until the solution converges. This method can be used to study the flow field around a ship, but there is an additional complication because two fluids are involved, air and water. From a numerical standpoint, the way to deal with a two-phases flow is not straightforward: the governing equations need to be rearranged properly.

2.2.1 FREE SURFACE MODELING

In the case of a two-phases flow, the numerical code has to resolve the governing equations, as in a basic single-phase problem, but in addition it has also to locate the position of the interface and its evolution in time if the analysis is unsteady. There are some different approaches to deal with this issue. A possible classification of these is depicted in Figure 2.2, where abbreviations stand for *marker-and-cell (MAC)*, *volume of uid (VOF)* and *constrained interpolation prole (CIP)*.

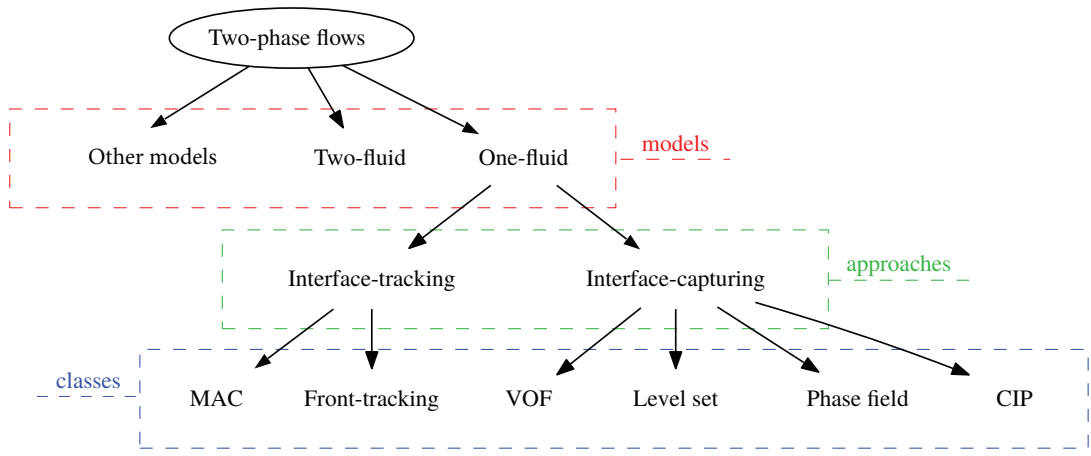


Figure 2.2: Free surface modeling approaches. Adapted from [21].

The most widely adopted methods are based on the one-fluid model, in which all fields are defined in both phases and are assumed continuous across the interface. To distinguish the two phases, the volume fraction α is introduced, whose value lies between 0 and 1. Every cell of the mesh is characterised by a value of α proportional to the volume of water contained in the cell itself. Cells that are completely immersed in water present $\alpha = 1$, while $\alpha = 0$ stands for only air inside the cell. In theory the interface is located where α changes abruptly from 0 to 1 but in practice, according to the free surface modeling method chosen, it may be more or less difficult to obtain such a perfectly sharp interface: usually α varies continuously from 0 to 1 within a certain number of cells at the free surface. Obviously the accuracy of the simulation grows if the number of cells which define the interface is reduced. This is especially important for a numerical simulation of a ship because in this case the interface coincides with the wave pattern and, as has been said in Chapter 1, waves are responsible for a substantial share of the total drag. The density field ρ , the dynamic viscosity field μ and the velocity field \mathbf{U} are then defined through the following relations:

$$\begin{aligned} \rho &= \alpha_1 + (1 - \alpha_2) \\ \mu &= \alpha_1 + (1 - \alpha_2) \\ \mathbf{U} &= \alpha \mathbf{U}_1 + (1 - \alpha) \mathbf{U}_2 \end{aligned} \quad 2.11$$

where the indices define the two different phases. These fields can be inserted into the RANS equations found out in Section 2.1.

Free surface modeling approaches based on the one-fluid model can be basically divided into two main groups: *interface tracking* and *interface capturing* methods. The latter are the more often used. A brief description of the main interface capturing methods is provided [22] below. Two-phases φ_1 and φ_2 are here considered and the interface is defined as $\varphi = 0$.

- LEVEL SET METHOD:

In the level set method, the interface position is captured by the signed distance function defined as follows:

$$\begin{aligned} \varphi(\mathbf{x}) = & \begin{cases} d & \text{if } \mathbf{x} \in \varphi_1 \\ 0 & \text{if } \mathbf{x} \text{ on the interface} \\ -d & \text{if } \mathbf{x} \in \varphi_2 \end{cases} \end{aligned} \quad 2.12$$

Here d is the shortest distance to the nearest point on the interface and \mathbf{x} is the position vector. The interface is reconstructed as the set of points for which $\varphi(\mathbf{x}) = 0$, which is called the *zero level set*.

- PHASE FIELD METHOD:

The so-called phase field φ is defined as:

$$\varphi(\mathbf{x}) = \tanh \frac{d}{\sqrt{2}} \quad 2.13$$

where φ is the signed distance function defined above and σ is a user controlled parameter that conditions the smearing of the interface. The phase field function is bounded between -1 and 1 and presents an hyperbolic tangent profile across the interface. The interface is located where $\varphi(\mathbf{x}) = 0$ as before.

- VOLUME OF FLUID METHOD:

The volume of fluid method relates directly to the volume fraction α which defines the two different phases in equations 2.11. Here the volume fraction is defined as a function of the phase field φ as follows:

$$\alpha(\mathbf{x}) = 0.5(sgn(\varphi) + 1) \quad 2.14$$

where $sgn(\varphi)$ is the signum function. From a numerical perspective, the reconstruction of the free surface with this method is often a hard task because of numerical instabilities. Smearing of the interface is usually reached with compressive schemes or additional compressive terms.

These three free surface modeling methods are schematically depicted in Figure 2.3.

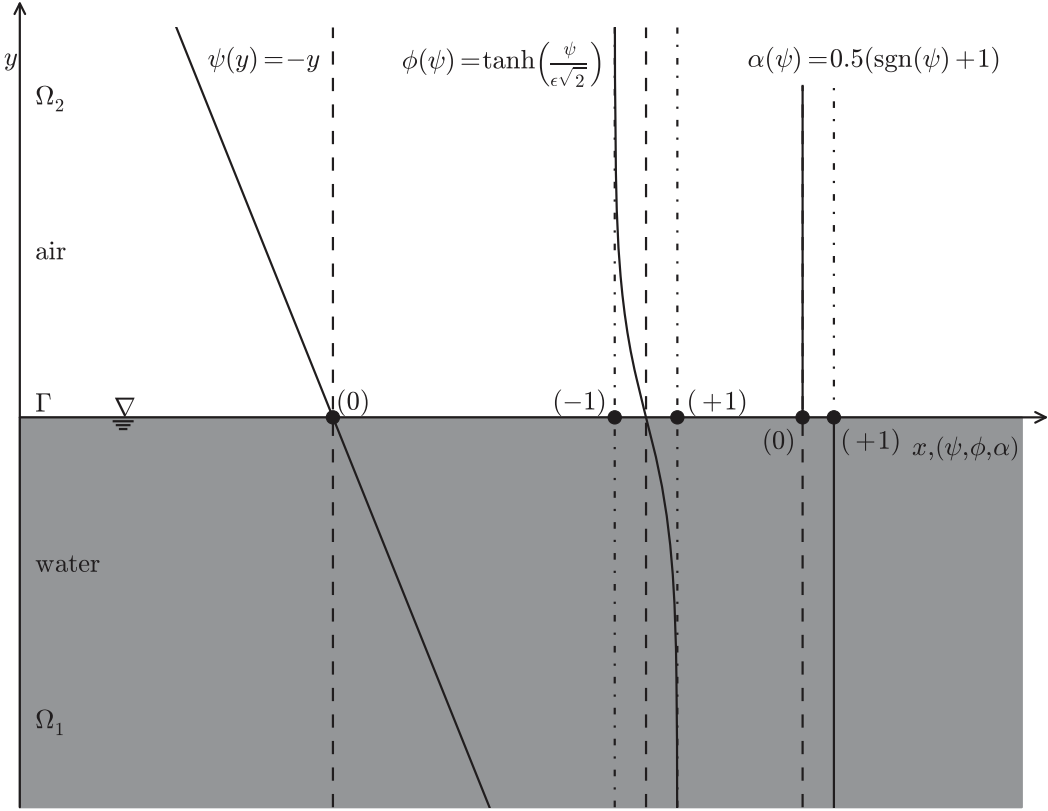


Figure 2.3: Sketch of the main interface capturing methods [22].

2.3 CFD ANALYSIS WITH OPENFOAM

OpenFOAM, which stands for *Open Source Field Operation and Manipulation*, is an open source C++ library where a great collection of precompiled applications is available to perform different types of analyses and where users are free to develop their own or modify existing ones. Tools to deal with pre- and post-processing are provided too. Two main groups of applications are available: *solvers* and *utilities*. The former deal with a large number of fluid dynamics problems but also continuum mechanics and other subjects, while the latter concern pre- and post-processing, meshing and data manipulation. The structure of OpenFOAM is shown in Figure 2.4.

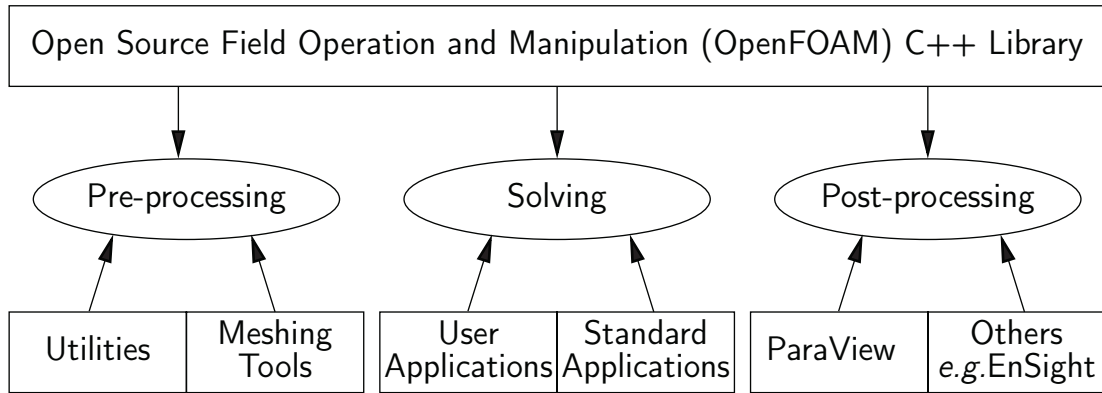


Figure 2.4: Basic structure of OpenFOAM [23].

The standard solvers provided by OpenFOAM can be divided into the following categories:

- Basic CFD codes
- Incompressible flow
- Compressible flow
- Multiphase flow
- Direct numerical simulation(DNS)
- Combustion
- Heat transfer and buoyancy-driven flows
- Particle-tracking flows
- Discrete methods
- Electromagnetics
- Stress analysis of solids
- Finance

Utilities, instead, deal with the following topics:

- Pre-processing
- Mesh generation
- Mesh conversion
- Mesh manipulation
- Other mesh tools
- Post-processing
- Post-processing data converters
- Surface mesh tools
- Parallel processing

The libraries are written in C++, an object-oriented language which provides the mechanism to declare types and associated operations for each mathematical object. Objects are for example scalars, vectors and tensors that appear in equations. This peculiarity makes numerical codes clearer, more compact and concise. For instance in a fluid dynamics solver, the velocity \mathbf{U} is an object of the class `vectorField`. This class derives from two

other classes, `vector` and `field`, and it inherits all their properties. Hence through the definition of a certain number of different classes and through the combination of them, it is possible to describe the features of every mathematical, geometrical, algebraic, physical object. Another example is the pressure P which belongs to the class `scalarField`.

2.3.1 COMPILING OPENFOAM APPLICATIONS

It has been said that users can modify every piece of code contained in OpenFOAM or write their own. To do this the `wmake` compiler executes all the instructions contained in the code and provides access to the components of the OpenFOAM library that are needed to compile the new application. This compiler is based on the `UNIXmake` utility, which is the most common compiler used in UNIX/Linux systems, but it is easier to use and more versatile.

Every new application or library written in OpenFOAM, for instance `newObject`, is treated as a new class and its properties are specified in the `newObject.c` file which is the so-called class *definition*. The `.c` file can be compiled independently of other codes into a binary executable library file known as a shared object library. In other words, the compiler creates an object with `.so` extension, for example `newObject.so`, which allows to compile pieces of code that use the `newObject` class without recompiling the `newObject.c` file. This is called *dynamic linking*.

Every `.c` file has a `.H` associated file, for instance `newObject.H`, which is called class *declaration*. In this file, the name of the class and its functions are listed. Every piece of code that uses the `newObject` class has to include the `newObject.H` file writing the command `#include "newObject.H"` at the beginning of the `.c` file. A piece of code contained in a `.c` file may need the properties and functions of a lot of classes: each of them are included at the beginning of the file. Moreover every class included in the considered `.c` file may include other classes and so on. For this reason, the `.H` files are called *dependencies*. The compilation process is sketched in Figure 2.5.

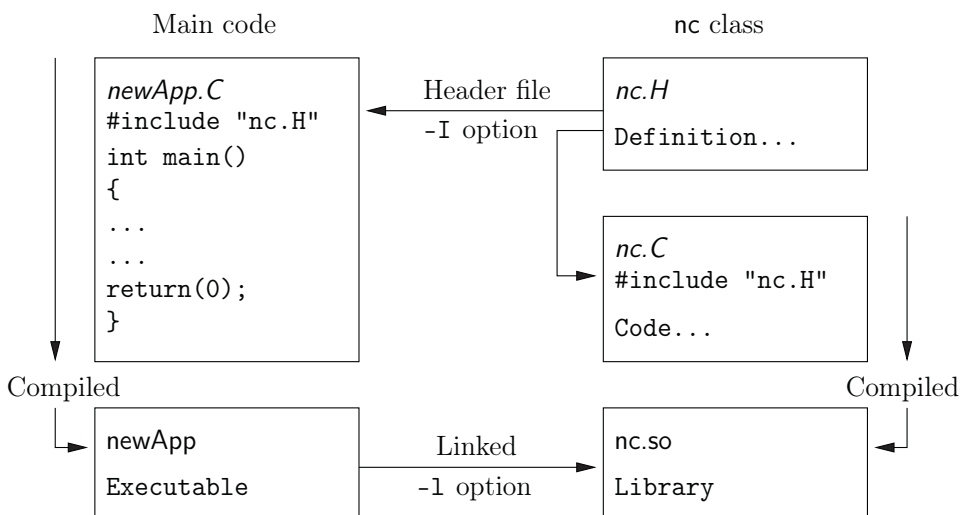


Figure 2.5: Compilation process of an OpenFOAM application [23].

OpenFOAM applications are made up of two files, a `.c` and a `.H`. However `wmake` needs some other instructions to compile the `.c` file and these are contained in two other files called `options` and `files`. The former contains the paths of all the `.H` and `.so` files that are needed to compile the application. In the latter, the `.c` source files that have to be compiled are listed together with the path and the name of the compiled executable. The files `options` and `files` are located in the `Make` directory. Hence the directory of an OpenFOAM application is organised as in Figure 2.6.

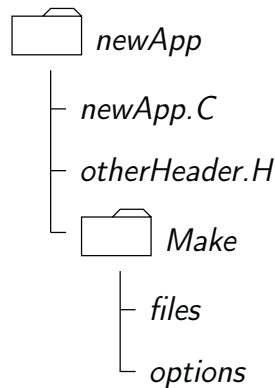


Figure 2.6: Directory structure for an OpenFOAM application [23].

The convention is to name the application's directory and all the application's files as the application itself. For example, the files of an application called `newObject` are contained in the `newObject` directory and their names are `newObject.c` and `newObject.H`. To compile the application it is sufficient to run the command `wmake`, adding the path of the `.c` file if the command is run from a different directory. When the compilation process is completed, in the `Make` directory of the application, a new file with `.dep` extension is created where the dependencies are listed. Finally if the `.c` file is modified and has to be recompiled, it is necessary to delete the `.dep` file with the command `wclean`. Once the application is compiled, it can be executed from a terminal command line.

2.3.2 ORGANIZATION OF AN OPENFOAM CASE

To run an OpenFOAM analysis it is necessary to organize the `CASE` directory, which shall contain files and directories where the parameters of all the applications involved are set up. A `CASE` directory is organized as shown in Figure 2.7: it typically contains two directories, `system` and `constant`, together with some time directories which are created during the simulation. All files controlling the simulation are organized as a list of keywords. For each keyword an entry can be specified. These files are called *dictionaries*.

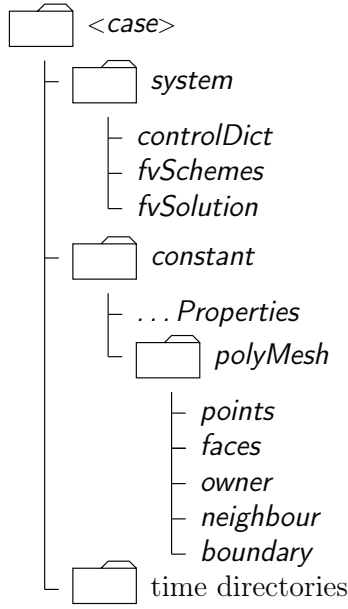


Figure 2.7: The basic structure of an OpenFOAM case [23].

- **THE system DIRECTORY:**

This directory contains several dictionary files, one for each application called during the simulation, where options and parameters can be set. Moreover there are three very important files: **controlDict**, **fvSchemes** and **fvSolution**. In the **controlDict**, time and data input and output are controlled, including start/end time, time step and time interval between saving data; in **fvSchemes**, the discretisation schemes used to express derivatives, gradients and so on may be selected; in **fvSolution** the equation solvers, convergence tolerances and other algorithm controls are specified.

- **THE constant DIRECTORY:**

Here physical properties such as the turbulence model or the value of the viscosity can be selected in appropriate files and the mesh is stored in the **polyMesh** directory.

- **TIME DIRECTORIES:**

Time directories are created at run-time and contain the simulation outputs at certain time steps. In the **controlDict**, users may decide how often simulation data have to be saved. If the analysis is run in parallel, during the simulation a directory is created for each processor which contains time directories of the decomposed simulation. Only at the end of the analysis the domain is recomposed and the time directories for the whole domain are created.

Once all files contained in **system** and **constant** directories are set, it is possible to start the simulation by writing a sequence of commands on the terminal window. Each command executes an application, which can be a solver or a utility, contained in the OpenFOAM library. All commands can be written into an executable file in order to simplify the process. Normally the simulation begins with the creation of the mesh, which

is carried out by using the proper OpenFOAM utility. Then it is possible to decompose the domain in order to run the solver in parallel. Also for this operation, there is the dedicated utility inside OpenFOAM. After that, the chosen solver is executed and the domain can be recomposed.

2.4 CONCLUSIONS

This chapter concerns numerical analyses used in naval applications to predict ship's performance.

The first part of the chapter briefly illustrates the equations involved. These are the well-known Navier-Stokes equations, which, for an incompressible flow, can be deduced by using the continuity law and the conservation of momentum. Until now there is no analytical solution to the Navier-Stokes, hence a numerical method is needed to solve them. Examples are the finite difference method, the finite element method or the the finite volume method. However today's computers are not powerful enough to allow either a numerical solution of these equations: they have to be simplified in some way. In RANS equations velocities and pressures are expressed as the sum of a time averaged term and a fluctuation term in order to describe statistically the effects of the turbulence. A turbulence model is then needed to represent turbulent phenomena. LES equations, instead, resolve the flow at a more detailed level than RANS: they use a turbulence model to represent only the smaller turbulent structures while the larger ones are resolved directly. Other equations which can be derived from the Navier-Stokes through the introduction of simplifying hypotheses are the Euler and the Laplace equations. In the former ones, the fluid is assumed to be inviscid whereas the latter ones are formulated under the assumption of potential flow.

In the second part of the chapter, numerical methods needed to handle two-phases flows are presented. The most commonly used in naval applications are the volume of fluid, the level set and the phase field method.

Finally, the third part of the chapter introduces the OpenFOAM framework. OpenFOAM is an open source C++ library where a great collection of precompiled applications is available to perform different types of analyses. Here the compiling of an OpenFOAM application is described and the organization of an OpenFOAM case is illustrated.

CHAPTER 3

THE CASE STUDY: HULL SIMULATION WITH INTERFOAM

The previous chapter summarizes briefly the laws of fluid dynamics, focusing in particular on numerical methods to deal with two-phases flows. Moreover the open source library OpenFOAM has been introduced, which has several capabilities and is a powerful tool to run CFD analysis. In this chapter the case study of this thesis is presented: DTMB 5415 hydrodynamics is studied performing CFD analysis with InterFoam, one of the multi-phase solvers of OpenFOAM. The OpenFOAM case set up to run the simulation is fully described. In addition, the validation of the model is carried out together with the analysis of the flow field, which is compared to the one provided by an experimental tank test.

3.1 INTRODUCTION

Ship geometry: The ship studied in this thesis is the U.S. navy combatant DTMB 5415, shown in Figure 3.1. The main features of the geometry are reported in Table 3.1. This ship is often used to conduct studies that involve CFD analysis because a large collection of experimental data, which is essential to validate numerical models, is available in literature together with the stl files of the geometry.

In this thesis, data provided by the Iowa Institute of Hydraulic Research of the University of Iowa (IIHR) [24], are considered to validate a CFD analysis. Experimental data refer always to a scaled model of the hull: IIHR model of DTMB 5415 presents a length between perpendiculars of 5.72m, corresponding to a geometrical scale factor λ of 24.8. Model's features are also indicated in Table 3.1.

From here on, the name DTMB 5415 will be used to label the ship's model, as the CFD analysis and all the further studies will be performed on the model itself. The frame of reference adopted in all the CFD simulations carried out in this chapter presents the origin located downstream of the stern, the horizontal axis aligned to the hull's longitudinal axis with positive direction towards the bow, the vertical axis directed upwards and y-axis directed outwards from the symmetry plane as can be seen in Figure 3.1.

The main characteristic of the hull is the presence of the so-called *sonar dome*, which is a particular kind of bulb located at the ship's bow. Its purpose is to house the electronic equipment used for navigation and detection. Usually it is positioned at the bow, but on smaller ships it may be mounted on the keel. In this thesis, the possibility to combine the functions of a sonar dome with the advantages of a bulbous bow (see Chapter 1) is

studied and for this purpose the influence of the bow's shape on the ship's performance is analysed. The other peculiarity of DTMB 5415 is the presence of a transom stern.

Description	Ship	Model
Scale factor (λ)	-	24.8
Length between perpendiculars (L_{PP}) [m]	142.0	5.72
Breadth (B) [m]	18.9	0.76
Draft (T) [m]	6.16	0.248
Wetted surface (S_W) [m ²]	2949.5	4.786

Table 3.1: Main dimensions of the full scale DTMB 5415 and of its model [24].

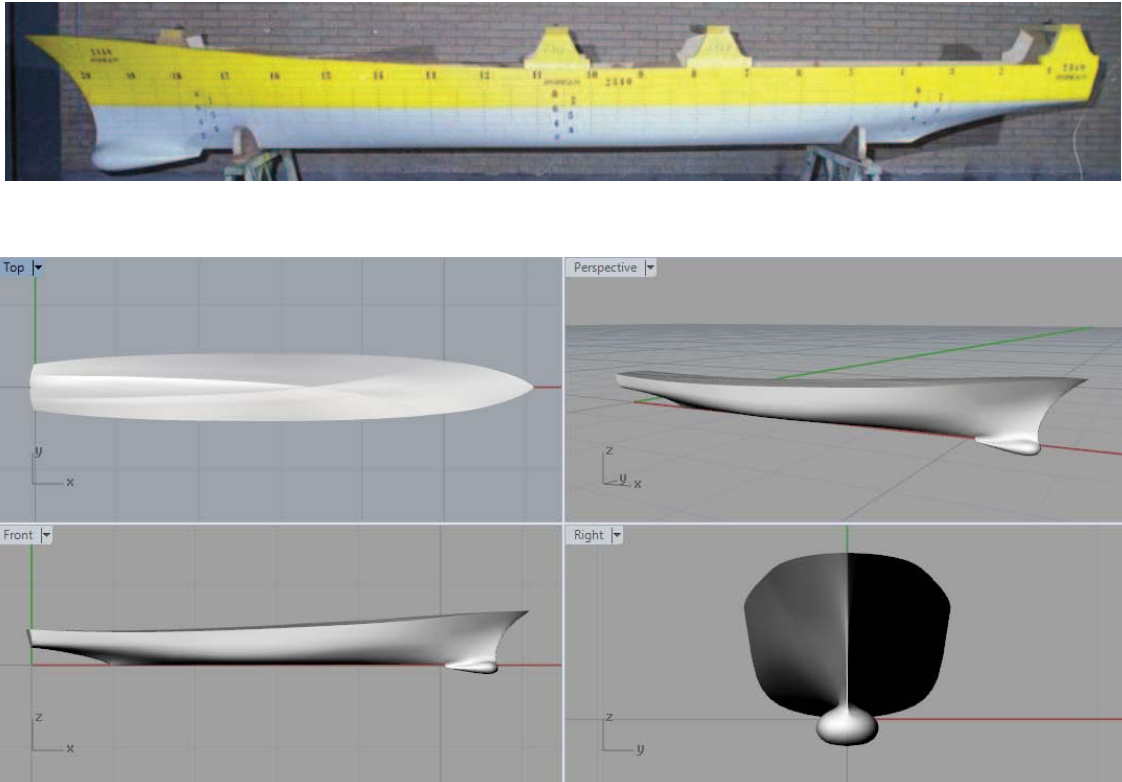


Figure 3.1: Above a photo of the DTMB 5415 model used in IIHR tank tests [24], below the stl file.

The InterFoam solver: The CFD analysis is performed by using the InterFoam solver of OpenFOAM. InterFoam is used for flows that involve two incompressible, isothermal, immiscible fluids, and adopts a volume of fluid method to track the interface. Another solver available in OpenFOAM to carry out naval CFD simulations is the InterDyMFoam, which provides optional mesh motion and mesh topology changes including adaptive remeshing and is used if sinkage and trim are free to change and need to be determined.

InterFoam computes the viscous and pressure resistance (R_V and R_P) along x , y and z direction as follows:

$$R_{Vx} = \sum_{n=1}^N x \quad R_{Vy} = \sum_{n=1}^N y \quad R_{Vz} = \sum_{n=1}^N z \quad 3.1$$

$$R_{Px} = \sum_{n=1}^N P n_x \quad R_{Py} = \sum_{n=1}^N P n_y \quad R_{Pz} = \sum_{n=1}^N P n_z \quad 3.2$$

where x , y , z and P are the tangential shear stresses and pressure acting on the elements of the mesh which correspond to the hull's surface – these are also called wall elements; n_x , n_y and n_z are the normals of these elements and ρ is the density of the water. The summations are performed over the wetted ($\alpha = 1$) wall elements (n). Then, the total resistance R can be calculated as $R = R_{Vx} + R_{Px}$.

In the CFD analysis, only one half of the hull is studied because the flow field is symmetrical with respect to the longitudinal axis of the ship. Hence all results are reported referring to one half of the hull.

The setting of the OpenFOAM simulation is based on the DTC hull InterFoam tutorial provided by OpenFOAM. This tutorial consists in meshing and simulating the flow field around a DTC hull model, which is 5.98m long. Some modifications have been necessary to adapt the DTC hull case to the DTMB 5415 geometry. These will be pointed out in Section 3.3.

3.2 THE DTMB 5415 OPENFOAM CASE

As it has been said in Chapter 2, the DTMB 5415 OpenFOAM case is structured as a directory containing the files that are necessary to run the various OpenFOAM applications involved in the analysis. These files are located in the `system` folder, together with `fvSchemes`, `fvSolution` and the `controlDict`. The other folders contained in the OpenFOAM case are `constant` and `0.orig`. The `stl` file of the DTMB 5415 is located in the `triSurface` subdirectory inside `constant` while the boundary conditions for the analysis are specified in files contained in the `0.orig` folder. These files simply describe the conditions of the flow field at the beginning of the simulation.

The DTMB 5415 case directory houses also two other files: `Allrun` and `Allclean`. The first contains all the commands to run the utilities and the solver that are needed to perform the simulation. These commands may be written one by one on the terminal windows. However this is not convenient: by running the `Allrun` file, all the commands reported inside are executed automatically. Instead, the `Allclean` file serves to remove all the files and directories created during the simulation, so that the OpenFOAM case can be modified and the analysis can be run again. To run the `Allrun` or the `Allclean` file, it is sufficient to type in the command windows `./Allrun` or `./Allclean`.

The `Allrun` file used to run the DTMB 5415 simulation is reported below and the main passages are explained.

```

1 #!/bin/sh
2 cd ${0%/} || exit 1
3
4 # Source run functions
5 . $WM_PROJECT_DIR/bin/tools/RunFunctions
6
7 runApplication surfaceFeatureExtract
8
9 runApplication blockMesh
10
11 for i in 1 2 3 4 5 6
12 do
13     runApplication -s $i \
14         topoSet -dict system/topoSetDict.${i}
15
16     runApplication -s $i \
17         refineMesh -dict system/refineMeshDict -overwrite
18 done
19
20 runApplication snappyHexMesh -overwrite
21
22 checkMesh -allTopology -allGeometry >log.checkMesh
23
24 rm -rf 0
25 cp -r 0.orig 0
26
27 runApplication setFields
28
29 runApplication decomposePar
30
31 runParallel renumberMesh -overwrite
32
33 runParallel $(getApplication)
34
35 runApplication reconstructPar

```

- **SOURCE CODE:** at line 5, the path to the source code of OpenFOAM is indicated. This is needed to execute OpenFOAM applications writing specific commands which would not be understood without the path specification.
- **surfaceFeatureExtract:** this command executes the OpenFOAM utility of the same name which is needed to extract the features of the geometry from the stl file. As for all the other applications called in the `Allrun` file, when the command that launches the application is executed, OpenFOAM searches in the `system` directory the associated dictionary file, which in this case is `SurfaceFeatureExtractDict`. Here a lot of options regarding the usage of the utility can be set. Once the application is run, OpenFOAM creates in the `constant` directory a folder named `extendedFeatureEdgeMesh`, which contains the geometric objects that have been extracted.
- **blockMesh:** this is the command needed to execute the `blockMesh` OpenFOAM utility. This application creates the domain of the simulation and a cartesian mesh

over the domain, whose characteristics may be specified in the `blockMeshDict`. In the case of DTMB 5415, the cartesian mesh becomes finer close to what will be the interface zone.

- `topoSet` AND `refineMesh`: these two OpenFOAM utilities are used inside the for loop in the `Allrun` file whose purpose is to refine the cartesian mesh in a certain zone of the domain where the hull will be situated. The `topoSet` utility selects a portion of the domain while `refineMesh` splits all mesh elements contained into the selected area in 8 smaller cells. After this process, the mesh is still cartesian. This process is repeated 6 times in increasingly smaller portions of the domain by using the for loop. Users can decide which areas of the mesh have to be refined in the `topoSetDict` files. In the `system` directory there is also a `refineMeshDict` file where some options can be set.
- `snappyHexMesh`: by using `blockMesh`, `topoSet` and `refineMesh`, the domain has been created, together with a cartesian mesh which has been refined in a certain area. However the hull has not yet been inserted into the mesh. To do this, OpenFOAM uses the `snappyHexMesh` utility. This application reads the `stl` file and the features of the geometry extracted by `surfaceFeatureExtract` – these they are located in sub-folders of the `constant` directory – and places them in the mesh. Then the so-called *snapping process* takes place: the mesh and the hull are joined together and some cell coats are added on the hull's surface to catch the boundary layer.
- `checkMesh`: at this point the mesh is ready. This utility verifies the goodness of the mesh by counting in how many cells the threshold values of some parameters are exceeded. For example some checks are the number of skew faces, of concave cells or of underdetermined cells. Their definition can be found in the OpenFOAM user's guide [23].
- SETTING OF THE ANALYSIS: at line 24 and 25 of the `Allrun` file, the time directory associated to the 0th time step is created as a copy of the `0.orig` folder. Then at line 27 the utility `setField` is executed to tell the solver what are the regions of the domain that are occupied by water or by air. This operation is controlled, as always, through the associated dictionary, which in this case is `setFieldDict`.
- RUNNING THE SOLVER: after the fields have been set, the simulation is ready. At line 29 and 31 of the `Allrun` file, the `decomposePar` and the `renumberMesh` utilities are executed to split the domain in different regions and launch the analysis in parallel over a certain number of processors. Finally at line 33, the `InterFoam` solver is called and at line 35, the domain is reconstructed once the solution has converged. The settings of the solver can be modified in the dictionaries `fvSchemes`, `fvSolution` and `controlDict`, located in `system` directory. The turbulence model chosen for the simulation is specified in the `turbulenceProperties` file which can be found in the `constant` folder.
- POST PROCESSING: useful tools to verify that all the steps of the simulation have been concluded without errors are the `log.files`: for each application called, OpenFOAM creates a file where all the operations that have been executed by the application are noted. For example, for the `blockMesh` utility a `log.blockMesh` file is

created. OpenFOAM provides also some post-processing tools to calculate quantities after the simulation has converged. Some post-processing utilities can be executed directly from the terminal windows, otherwise a GUI interface, ParaView, is available to perform more complex operations. Hence after the CFD analysis has converged, the values of the total drag acting on the hull and of the pressure and viscous components of resistance can be computed.

3.3 VALIDATION

The first step of the validation of a DTMB 5415 model has been the simulation of the DTC hull tutorial, in order to see if this case would have been a good starting point to develop a new model. The tutorial case has led to results in good agreement with experimental data, so the following step has been the simulation of the DTMB 5415 geometry using exactly the same settings as the DTC hull case. This first simulation, named DTMB01, has given a good prediction of the drag force. However the comparison between the wave profile at a certain distance from the ship's longitudinal axis obtained through the CFD analysis and the one obtained through experimental tests was not so good. In order to improve this aspect, a few changes have been applied to the mesh, operating in particular on the refinement process. These modifications have led to better results with the drawback of increasing the number of cells and, therefore, the computational time. The flow field around this new model, DTMB02, has been studied and compared with the experimental one. The main hydrodynamic phenomena are caught by the CFD analysis while some smaller vortex structures cannot be noticed on the simulation's contour. To catch them properly, a further increase of the number of cells would have been necessary. The DTMB02 model has been considered to be a good compromise between accuracy and computational time. This choice has been supported by the final purpose of this thesis, which is the study of the influence of some geometrical features on the ship's performance: the simpler way to evaluate the ship's performance is given by the drag force, which is reasonably well predicted by the DTMB02 model. In the following sections, the above-mentioned steps of the validation process are explained in more detail.

3.3.1 THE DTC HULL TUTORIAL

Ship geometry: Figure 3.2 shows the DTC hull shape, while the main dimensions of the full scale ship and the corresponding model are reported in Table 3.2. Experimental data for this ship can be found in the paper by el Moctar et al. [25].

Assumption: The simulation is carried out under the following assumptions: model-scale, calm water, no propeller and appendages, fixed trim condition, symmetry about the vertical longitudinal plane, constant temperature, constant fluid (air and water) properties.

Description	Ship	Model
Scale factor (λ)	-	59.4
Length between perpendiculars (L_{PP}) [m]	355.0	5.98
Breadth (B) [m]	51.0	0.86
Draft (T) [m]	14.5	0.244
Wetted surface (S_W) [m ²]	22032.0	6.243

Table 3.2: Main dimensions of the full scale DTC hull and of its model [24].

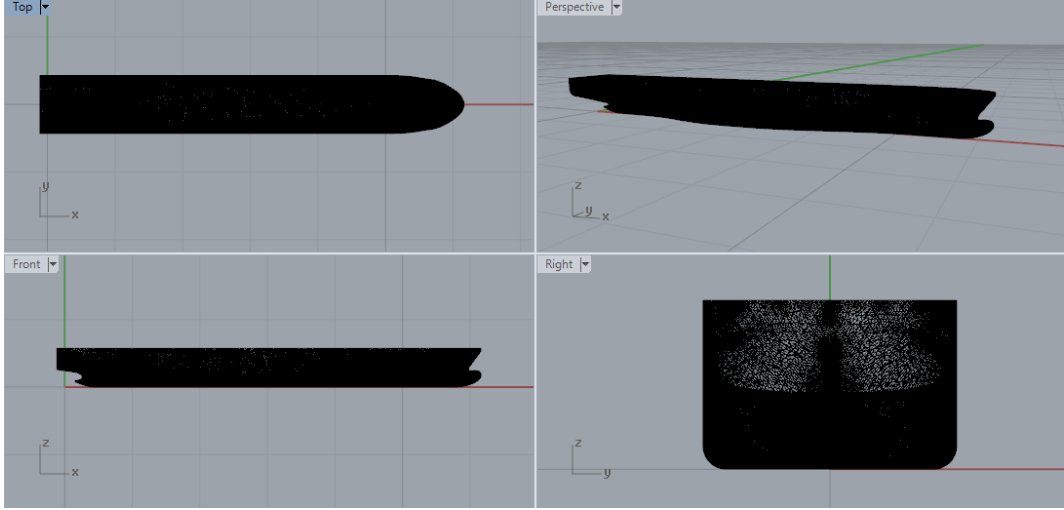


Figure 3.2: Geometry of the DTC hull.

The computational domain: It is defined in the `blockMeshDict`. Figure 3.3 shows the 6 blocks created by the `blockMesh` utility while the diagonal vertices defining them are listed in Table 3.3. The interface is located at $z = 0.244m$ and lies between two thin blocks which are not clearly visible in the figure. After the execution of the `blockMesh` application, the mesh consists of 42 cells along the longest side of the domain and 19 cells along the shortest one for a total of 134 064 elements. Figure 3.4 shows how the mesh looks like at this point of the meshing process.

Block number	Inferior vertex coord. [m]	Superior vertex coord. [m]
1 ■	(-26 -19 -16)	(16 0 -1)
2 ■■	(-26 -19 -1)	(16 0 0.185)
3 ■■■	(-26 -19 0.185)	(16 0 0.244)
4 ■■■■	(-26 -19 0.244)	(16 0 0.3)
5 ■■■■■	(-26 -19 0.3)	(16 0 1.6)
6 ■■■■■■	(-26 -19 1.6)	(16 0 4)

Table 3.3: Diagonal vertices of the blocks created by `blockMesh`. Colours correspond to the ones in Figure 3.3.

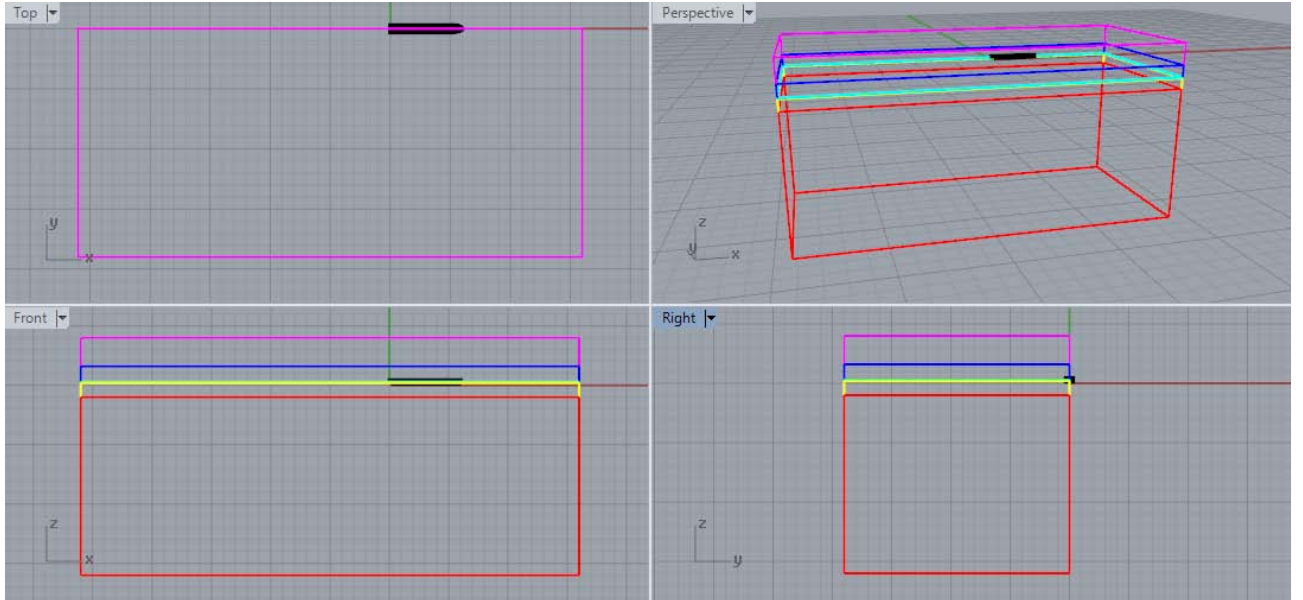


Figure 3.3: Blocks created by `blockMesh`.

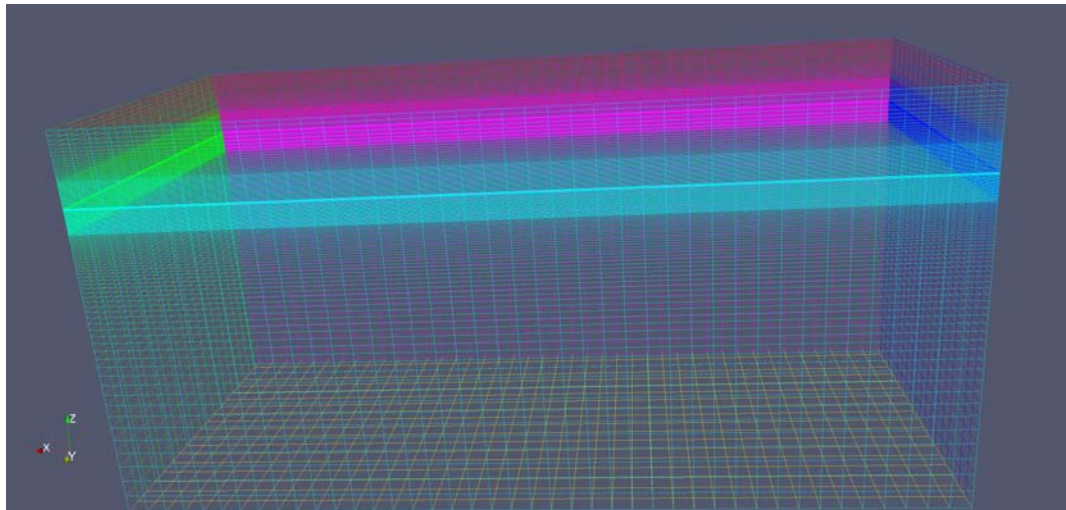


Figure 3.4: Computational domain after the execution of `blockMesh`.

Mesh refinements: In Figure 3.5 are highlighted the domain's portions involved in the refinement process, while in Table 3.4 the diagonal vertices of the refinement boxes are reported. When all the refinements are completed, the mesh consists of 513 216 cells.

The final mesh: The final mesh, which is the one obtained after `snappyHexMesh` is executed, consists of 848 025 elements. Figures 3.6 and 3.7 show particulars of the mesh where the refined regions and the cells added on the hull's surface to catch the boundary layer are clearly visible.

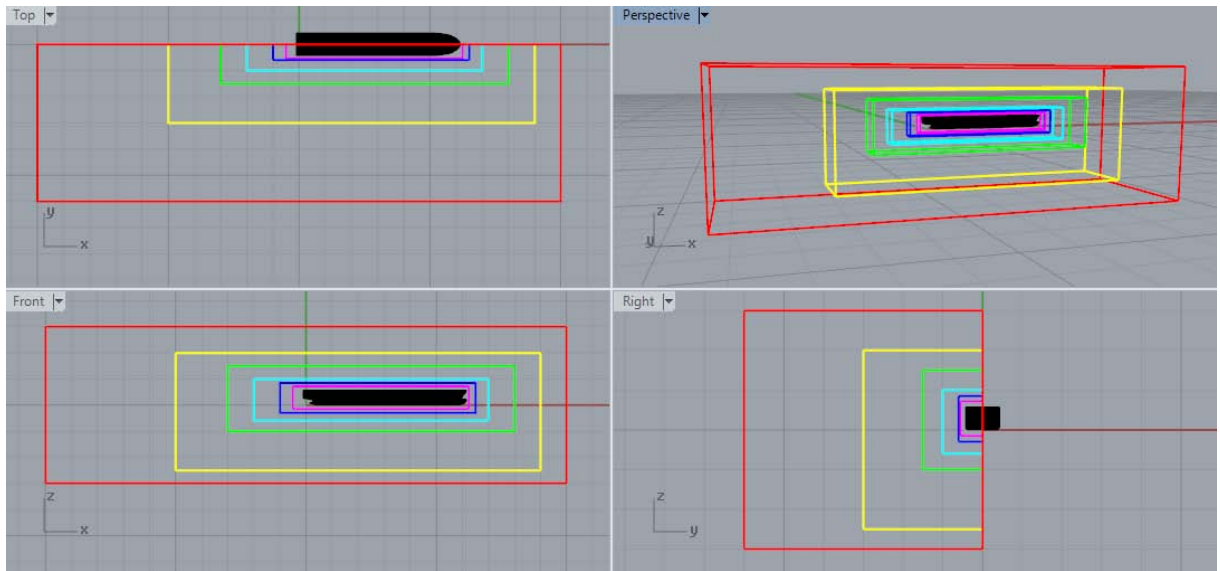


Figure 3.5: Regions where the mesh is refined.

Refinement	Inferior vertex coord. [m]	Superior vertex coord. [m]
1 ■	(-10 -6 -3)	(10 0 3)
2 ■■	(-5 -3 -2.5)	(9 0 2)
3 ■■■	(-3 -1.5 -1)	(8 0 1.5)
4 ■■■■	(-2 -1 -0.6)	(7 0 1)
5 ■■■■■	(-1 -0.6 -0.3)	(6.5 0 0.8)
6 ■■■■■■	(-0.5 -0.55 -0.15)	(6.25 0 0.65)

Table 3.4: Diagonal vertices of the refinement boxes. Colours correspond to the ones in Figure 3.5.

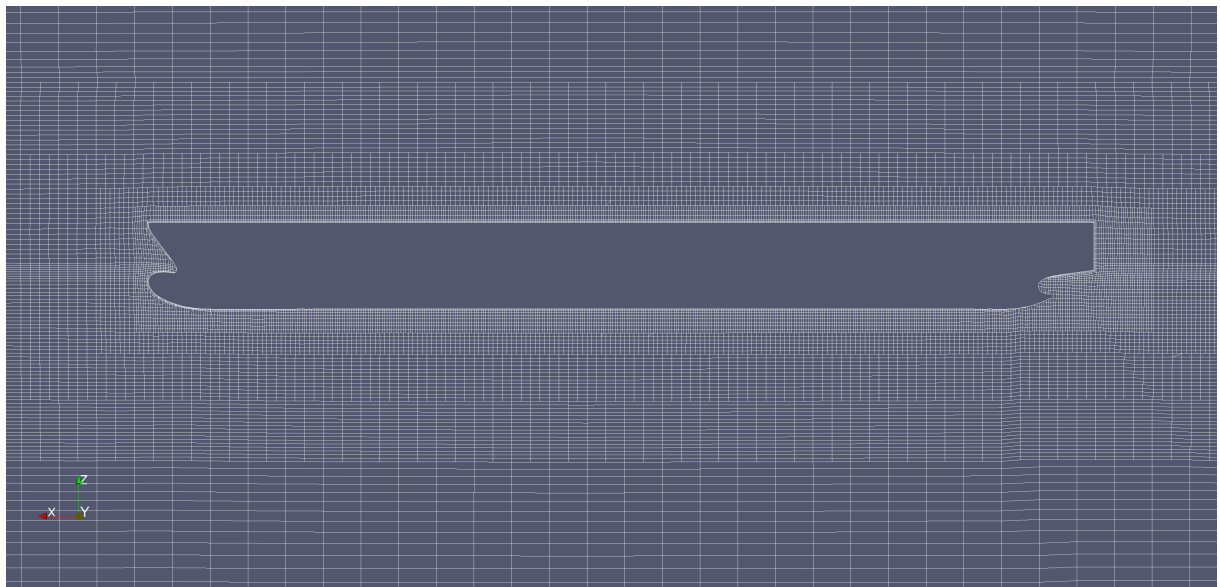


Figure 3.6: A particular of the final mesh: the refined regions are clearly visible.

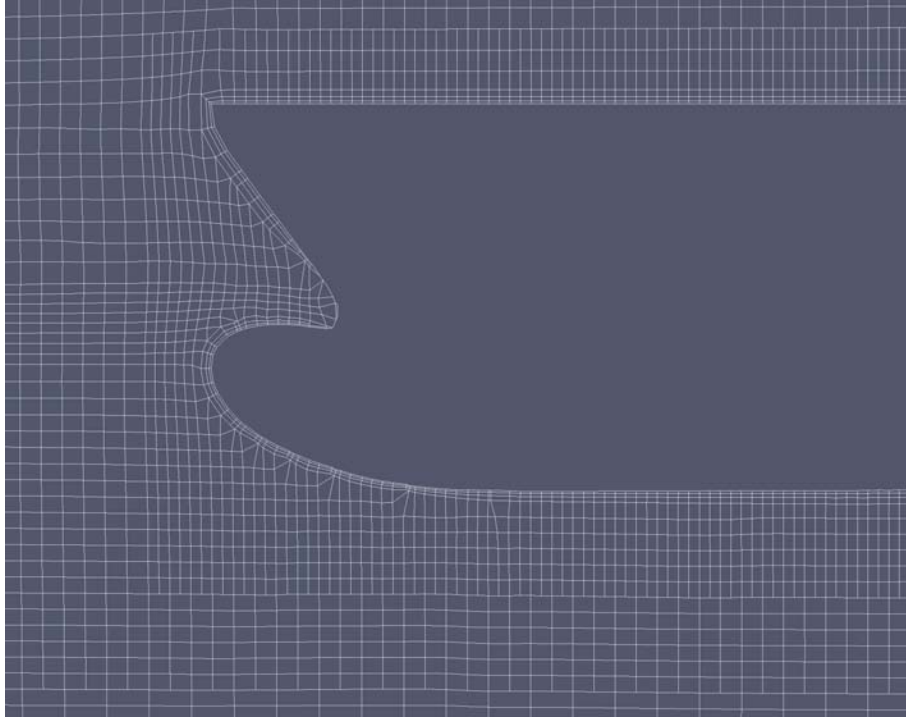


Figure 3.7: A particular of the final mesh: the cells added on the hull's surface to catch the boundary layer are clearly visible.

Boundary condition: The simulation is performed at a velocity equal to $\mathbf{U} = 1.668m/s$, which corresponds to a Froude number $Fr = 0.218$. The full scale ship at this Froude number moves at a velocity equal to $\mathbf{U} = 25kn = 12.86m/s$.

Turbulence model and transport properties: The turbulence model adopted for the simulation is OmegaSST. The kinematic viscosity and the density of water and air are reported in Table 3.5.

Phase	Density [kg/m ³]	Kinematic viscosity [m ² /s]
Air	1	$1.48 \cdot 10^{-5}$
Water	998.8	$1.09 \cdot 10^{-6}$

Table 3.5: Transport properties for the DTC hull simulation.

Results: The simulation converges after 4000 iterations. Table 3.6 reports the drag force given by the CFD simulation of the just described OpenFOAM DTC hull tutorial and the drag force provided by experimental data. It is possible to observe that there is good agreement between the two values as the percentage error amounts to 0.6%. For this reason, this case has been taken as a starting point to build a DTMB 5415 numerical model.

CFD drag [N]	Experimental drag [N]
15.82	15.92

Table 3.6: Comparison between the CFD result and the experimental data for the DTC hull.

3.3.2 THE DTMB01 MODEL

In this simulation, everything is kept as in the previous case and only the ship's geometry is replaced by the DTMB 5415. Since the two ships share similar dimensions – the DTC hull is $5.98m$ long while the DTMB 5415 is $5.72m$ long – no modifications have been necessary to adapt the domain to the new geometry. The hull has been positioned in the proper location inside the domain by changing its position with respect to the origin in the stl file.

Boundary conditions: The CFD simulation is carried out at a Froude number $Fr = 0.28$, which corresponds to a velocity of $\mathbf{U} = 2.0974m/s$. The full scale ship's speed at this Froude number is $\mathbf{U} = 20.3kn = 10.45m/s$. From here on, all DTMB 5415 simulations will be carried out at this Froude number.

The ship has to be positioned on the free surface considering its dynamic trim and sinkage. These data can be found within IIHR tank test results and are summarized in Table 3.7: combining the trim angle and the sinkage elevation, the bow and the stern of the ship have to be moved respectively $11.8mm$ and $1mm$ upwards with respect to the undisturbed, no motion configuration.

Trim angle [degrees]	0.108	Sinkage [mm]	1.82
Bow elevation [mm]	11.8	Stern elevation [mm]	1

Table 3.7: Dynamic configuration of the ship at $Fr = 0.28$ [24].

Transport properties: The kinematic viscosity and the density of water and air adopted in the simulation are listed in Table 3.8. These values are reported in the experimental tests documentation.

Phase	Density [kg/m ³]	Kinematic viscosity [m ² /s]
Air	1	$1.48 \cdot 10^{-5}$
Water	998.8	$1.008 \cdot 10^{-6}$

Table 3.8: Transport properties for the DTMB01 simulation.

Results: The number of mesh elements for this simulation amounts to 513 216 cells before `snappyHexMesh` execution, as the mesh refinements are the same as before, and 896 917 cells after. The simulation converges after 4000 iterations. In Table 3.9 the result of the CFD analysis is reported and compared to experimental data. Once again it is possible to note that the CFD simulation predicts the ship performance with very good accuracy, as the percentage error is equal to 1.1%. Figure 3.8 depicts wave cuts at $y/L_{PP} = 0.172$. Comparing the wave profile obtained through CFD and the one provided by tank tests, it is possible to note that although the general trend is caught, there are some significant discrepancies in the peak zones. This problem has been related to an insufficient number of mesh elements near the hull's area. Therefore the model has been improved by increasing the number of cells in this region.

CFD drag [N]	Experimental drag [N]
22.33	22.58

Table 3.9: Comparison between the CFD result and the experimental data for DTMB01.

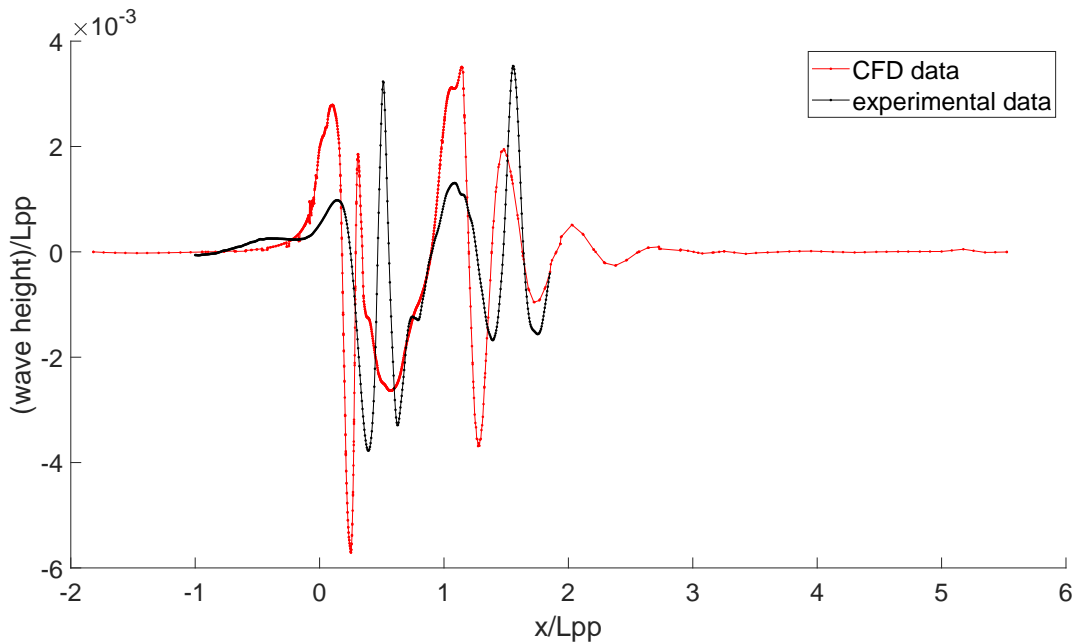


Figure 3.8: DTMB01: longitudinal wave cuts at $y/L_{PP} = 0.172$.

3.3.3 THE DTMB02 MODEL

Mesh refinements: To improve the wave profile of the CFD analysis, the refinement process of the mesh construction has been slightly modified by changing basically the dimensions of the refinement boxes. Figure 3.9 shows the new refinement boxes, while in Table 3.10 their diagonal vertices are listed. They can be compared to the original ones, listed in Table 3.4, to appreciate the differences. With these modifications the number of mesh elements is equal to 907 200 before the execution of `snappyHexMesh` and 2 356 423 after.

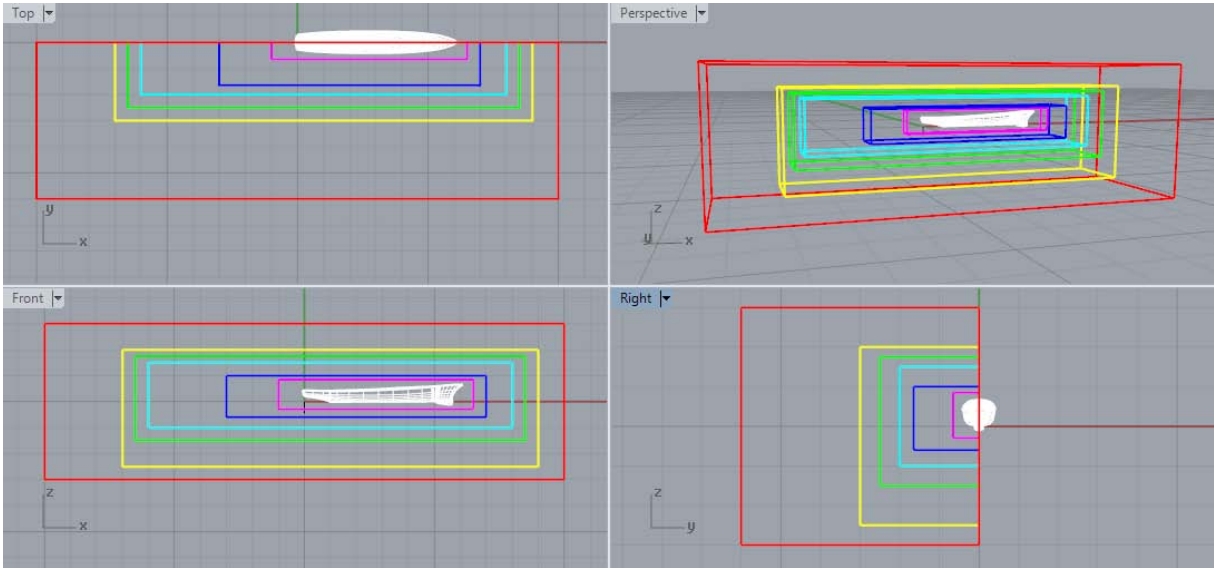


Figure 3.9: New refinement boxes for the `refineMesh` utility.

Refinement	Inferior vertex coord. [m]	Superior vertex coord. [m]
1 ■	(-10 -6 -3)	(10 0 3)
2 ■	(-7 -3 -2.5)	(9 0 2)
3 ■	(-6.5 -2.5 -1.5)	(8.5 0 1.75)
4 ■	(-6 -2 -1)	(8 0 1.5)
5 ■	(-3 -1.65 -0.6)	(7 0 1)
6 ■	(-1 -0.65 -0.3)	(6.5 0 0.85)

Table 3.10: Diagonal vertices of the new refinement boxes. Colours correspond to the ones in Figure 3.9.

Results: The simulation converges after 4000 iterations. Below, Table 3.11 reports the drag value provided by the simulation compared to the experimental one. The percentage error amounts to 1.2%. Figure 3.10 depicts the wave cut at $y/L_{PP} = 0.172$ and the one derived from tank tests. The modified mesh allows a better resolution of the wave profile

compared to the one obtained with the DTMB01 model, which is shown in Figure 3.8. In the following section the flow field provided by the DTMB02 CFD simulation is analysed and compared to the experimental one.

CFD drag [N]	Experimental drag [N]
22.86	22.58

Table 3.11: Comparison between the CFD result and the experimental data for DTMB02.

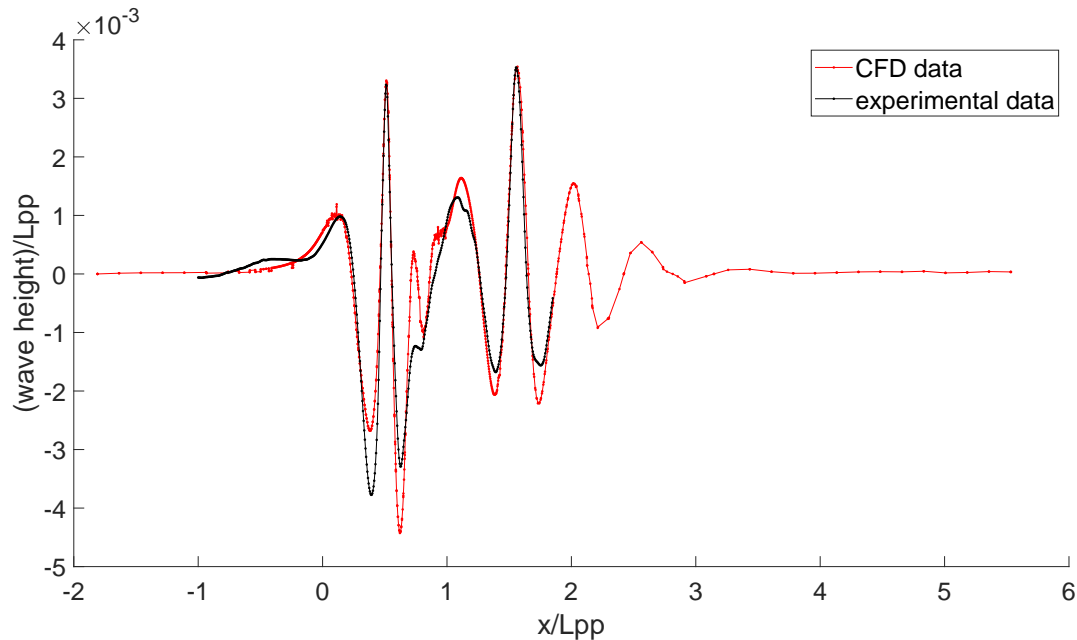


Figure 3.10: DTMB02: longitudinal wave cuts at $y/L_{PP} = 0.172$.

3.3.4 FLOW FIELD ANALYSIS

This section is based on the analysis carried out by Olivieri et al. in [24]. The study of the flow field is performed by considering some slices of the flow field where peculiar hydrodynamic phenomena occur. The considered sections are located at $x/L_{PP} = 0, 0.1, 0.2, 0.4, 0.6, 0.8, 0.9346, 1.1, 1.2$. The plane at $x/L_{PP} = 0$ coincides with the bow of the ship while the section at $x/L_{PP} = 0.9346$ is taken into account because it corresponds to the propeller plane. In Figures from 3.11 to 3.22 the velocity contours of the DTMB02 CFD analysis are reported for all the above-mentioned sections compared to the experimental flow field. The velocity scale is normalized with respect to the ship's speed while dimensional quantities are normalized with respect to the ship's length.

- SECTION AT $x/L_{PP} = 0$: at this section (Figure 3.11) it is possible to observe the stagnation point at the bulb extremity. Experimental data and CFD analysis are in good agreement.

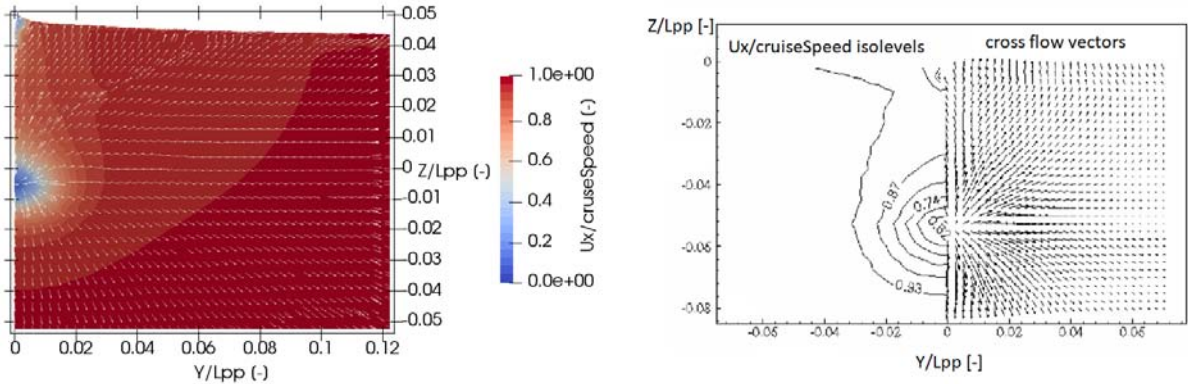


Figure 3.11: Velocity contours at $x/L_{PP} = 0$: CFD on the left and experimental on the right, adapted from [24].

- SECTION AT $x/L_{PP} = 0.1$: the experimental and numerical contours are once again similar, as can be seen in Figure 3.12. In this section two little counter-rotating vortices are forming in front of the sonar dome in symmetrical positions with respect to the longitudinal hull axes. These vortices are due to the lifting effect of the bulb, whose orientation is not parallel to the local direction of the velocity. In fact, by drawing over the considered plane the mean values of the vertical and longitudinal components of the local velocity and combining them, it is possible to estimate that the global flow around the sonar dome is oriented at an incidence angle of about $\alpha_i = 5^\circ$ as is depicted in Figure 3.13. The inclination of the local flow causes a non-zero circulation around the bulb itself and the appearance of the two vortices, which are called *bow bilge vortices*.
- SECTIONS AT $x/L_{PP} = 0.2, 0.4$: the vortices formed in the previous section are evolving downstream hence in these planes their development can be observed. Looking at Figures 3.14 and 3.15, it is possible to notice that the CFD simulation is still able to catch them, although not very clearly.

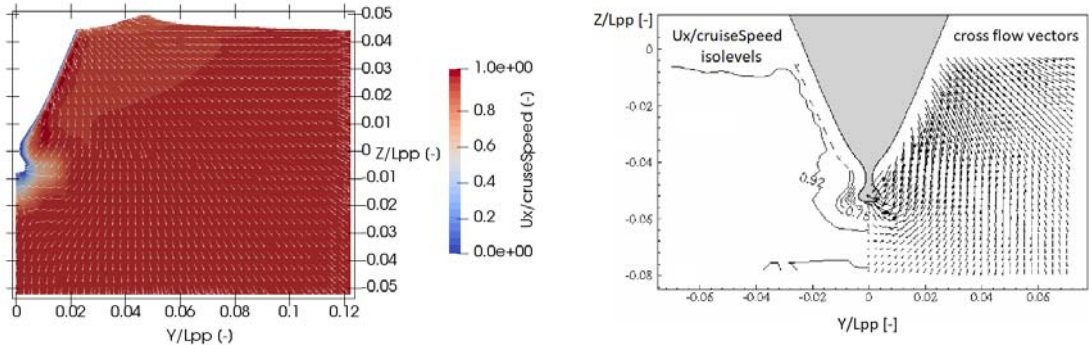


Figure 3.12: Velocity contours at $x/L_{PP} = 0.1$: CFD on the left and experimental on the right, adapted from [24].

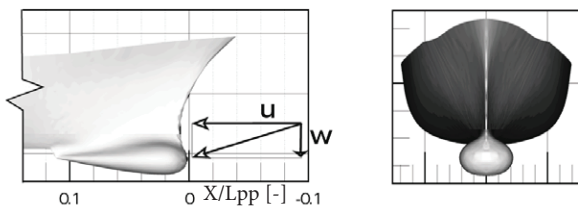


Figure 3.13: Velocity vector representing the flow at incidence to the bulb. Adapted from [24].

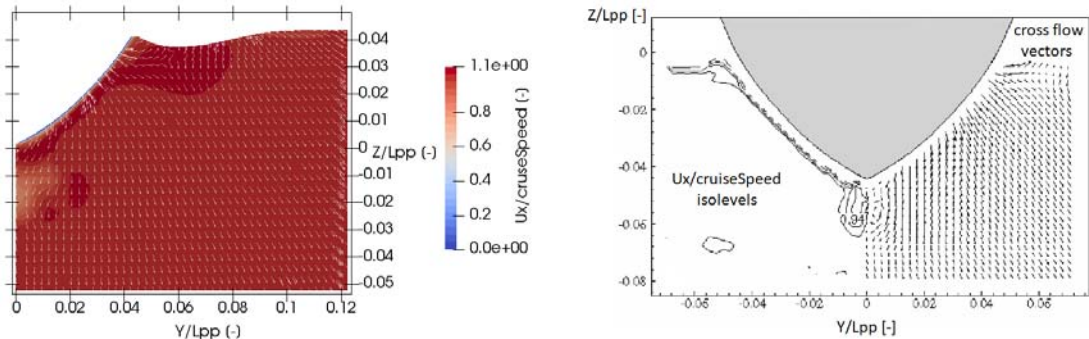


Figure 3.14: Velocity contours at $x/L_{PP} = 0.2$: CFD on the left and experimental on the right, adapted from [24].

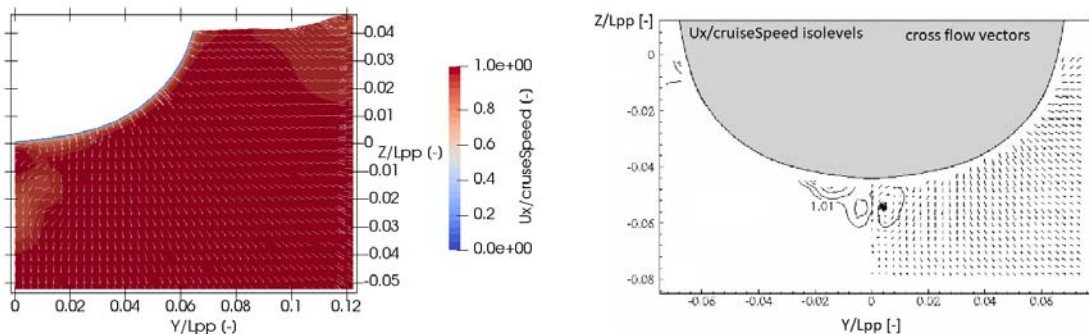


Figure 3.15: Velocity contours at $x/L_{PP} = 0.4$: CFD on the left and experimental on the right, adapted from [24].

- SECTION AT $x/L_{PP} = 0.6$: the experimental contour at this section, showed in Figure 3.16, suggests the formation of another pair of vortices in addition to those already introduced. These vortices are called *stern bilge vortices* and are due to the adverse pressure gradient in the aftbody, which causes the convergence of the limiting streamlines. By observing the CFD contour at this section, it is possible to notice that this phenomenon is not well caught by the simulation. In fact, CFD contours highlight the presence of only one bigger vortex, which can be better seen at section $x/L_{PP} = 0.55$, Figure 3.17. This is presumably due to a too coarse mesh.

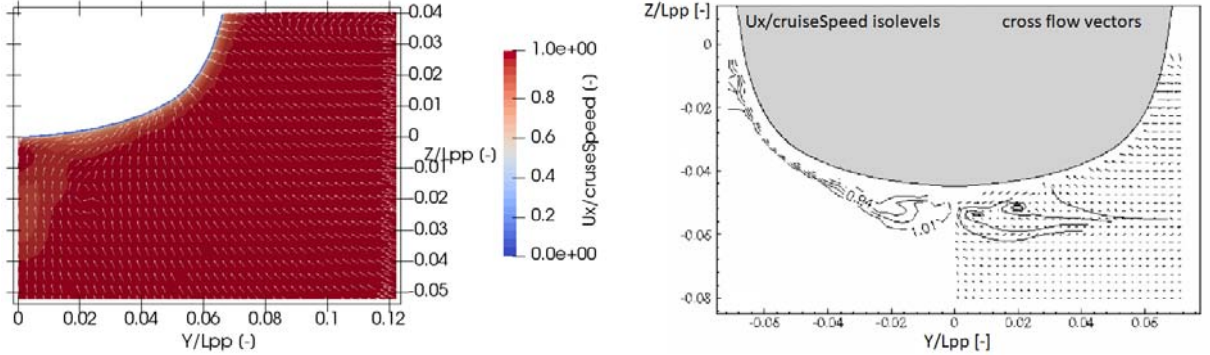


Figure 3.16: Velocity contours at $x/L_{PP} = 0.6$: CFD on the left and experimental on the right, adapted from [24].

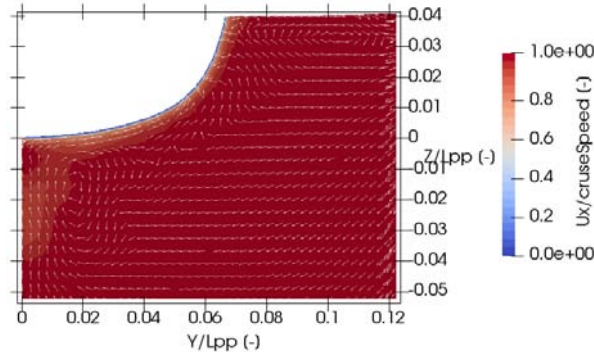


Figure 3.17: Velocity contours of DTMB02 at $x/L_{PP} = 0.55$.

- SECTIONS AT $x/L_{PP} = 0.8, 0.9346$: here all vortices disappear both in the experimental and in the numerical flow field. This can be seen in Figures 3.18 and 3.19, where a progressive growth of the boundary layer for viscous effects is also appreciable.
- SECTION AT $x/L_{PP} = 1$: this section corresponds to the stern. Figure 3.20 shows the unsteadiness of the flow around the transom area both in the CFD and in the experimental contour plot.

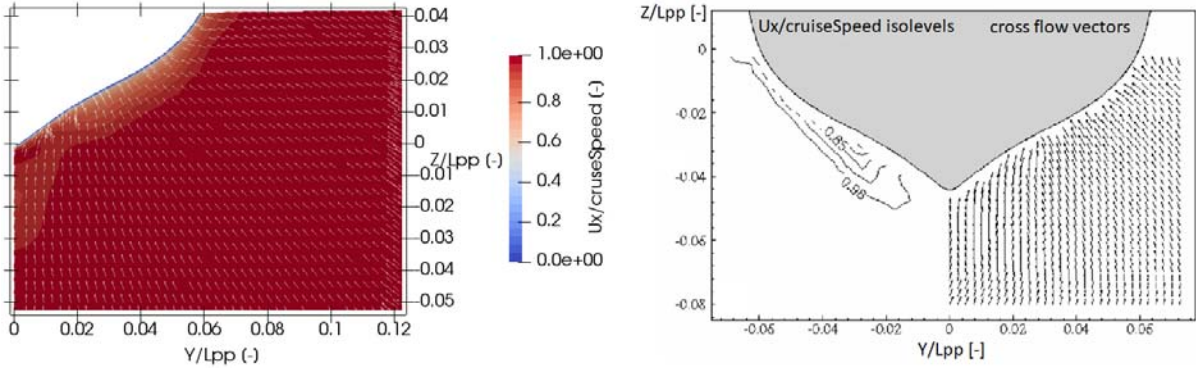


Figure 3.18: Velocity contours at $x/L_{PP} = 0.8$: CFD on the left and experimental on the right, adapted from [24].

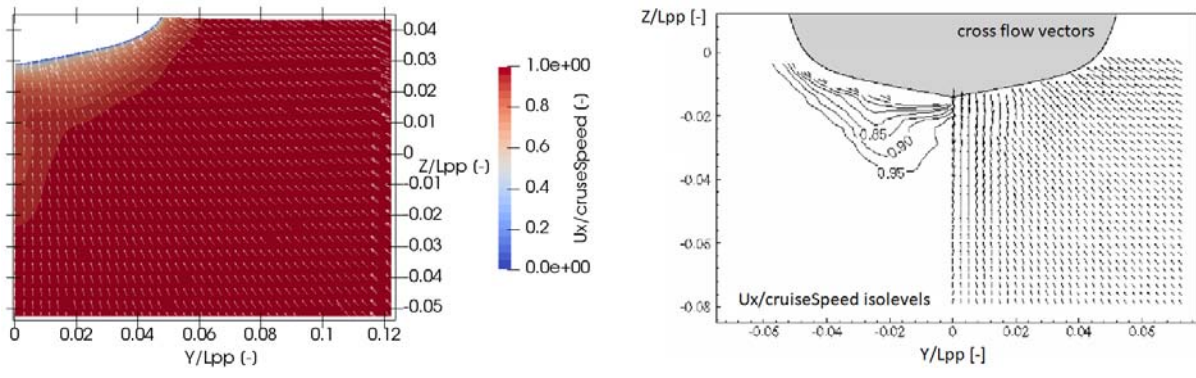


Figure 3.19: Velocity contours at $x/L_{PP} = 0.9346$: CFD on the left and experimental on the right, adapted from [24].

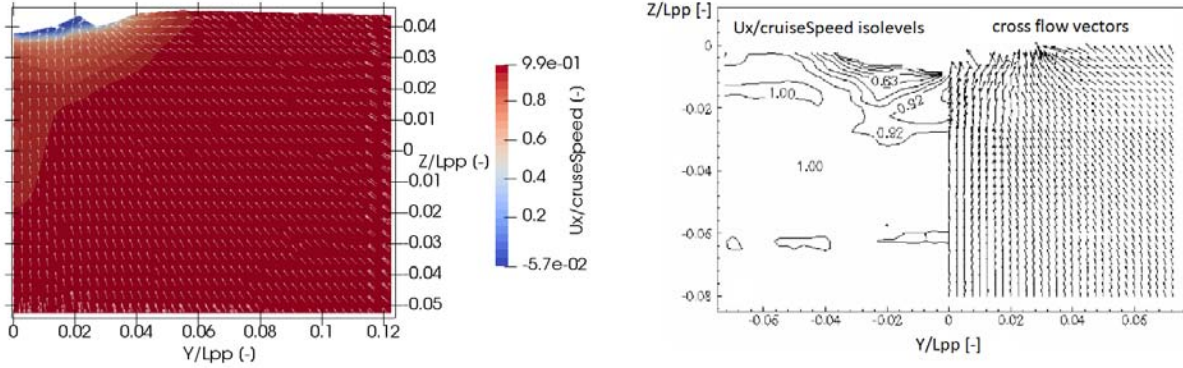


Figure 3.20: Velocity contours at $x/L_{PP} = 1$: CFD on the left and experimental on the right, adapted from [24].

- SECTIONS AT $x/L_{PP} = 1.1, 1.2$: downstream of the stern, a pair of counter-rotating big vortices appear. These vortices are well caught by the numerical analysis in the section located at $x/L_{PP} = 1.1$, Figure 3.21, while they disappear in the following plane, Figure 3.22. This is as before due to an insufficient number of mesh elements.

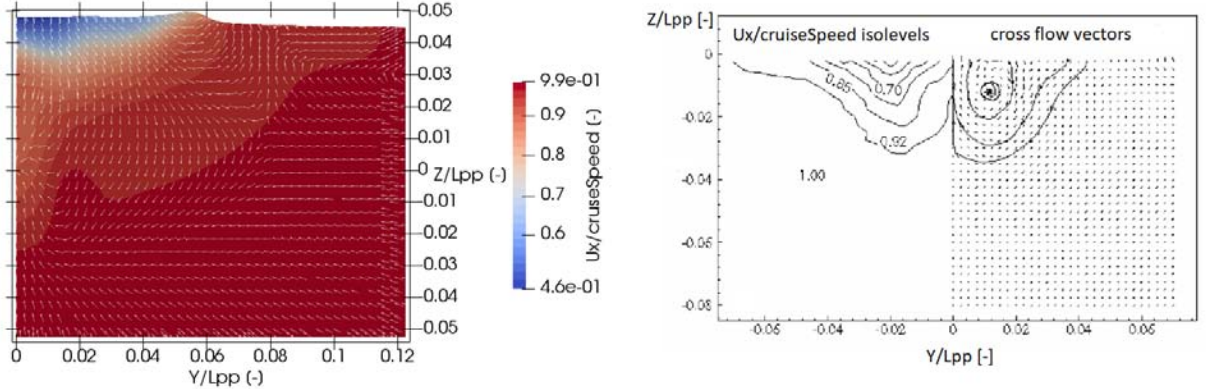


Figure 3.21: Velocity contours at $x/L_{PP} = 1.1$: CFD on the left and experimental on the right, adapted from [24].

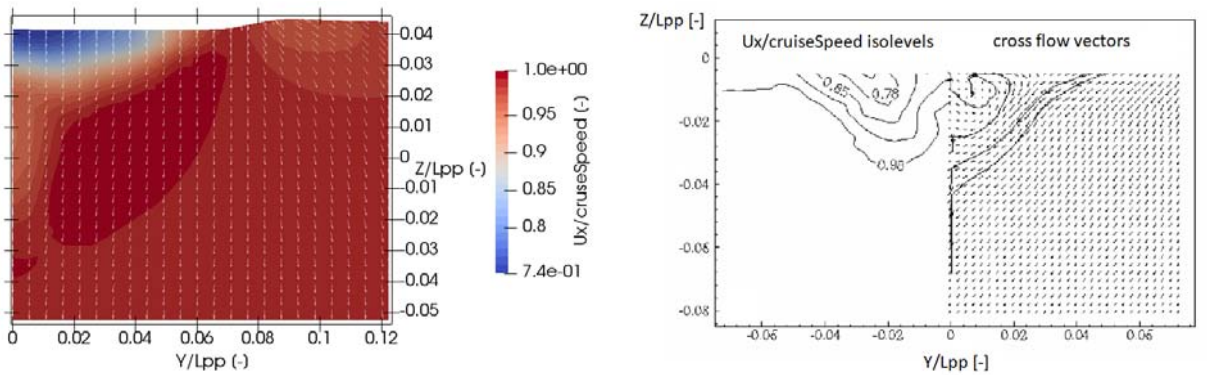


Figure 3.22: Velocity contours at $x/L_{PP} = 1.2$: CFD on the left and experimental on the right, adapted from [24].

The above analysis shows that the hydrodynamic phenomena that affect the flow field have been generally well caught by the CFD simulation. More specifically, although the vortical structures are clearly captured by the numerical analysis only in some regions, the trend is always followed. This should be considered a good result, especially in relation to the aim of this work: only a good estimation of the drag force is necessary to the studies that will be carried out in the following chapters. Therefore the DTMB02 numerical model has been considered to be validated for the purposes of this thesis. The DTMB01 provides a good estimation of the resistance too. Nevertheless the DTMB02 model has been preferred because it provides a better approximation of the wave pattern which, as shown in Chapter 1, has a strong influence on the drag.

3.4 CONCLUSIONS

In this chapter a numerical model for the DTMB 5415 ship has been validated in OpenFOAM. The work described here is totally original.

At the beginning of the chapter a detailed description of the OpenFOAM case and of the `Allrun` file needed to run the CFD analyses is provided, to gain a better understanding of the subsequent sections.

The CFD simulations have been performed by using the InterFoam solver of OpenFOAM under the following assumptions: calm water, no propeller and appendages, fixed trim condition, constant temperature and constant fluid (air and water) properties. The turbulence model adopted for the simulations is the OmegaSST. Only one half of the hull has been studied because the flow field is symmetrical with respect to the longitudinal axis of the ship. Hence all results refer to one half of the hull.

The mesh has been built by using the `blockMesh`, `refineMesh` and `snappyHexMesh` utilities available in OpenFOAM. The first creates the domain of the simulation and a cartesian mesh over the domain. The second splits all the mesh elements contained into selected regions in order to obtain a finer mesh close to the hull. The third inserts the ship's geometry in the domain: the mesh and the hull are joined together and some cell coats are added on the hull's surface to catch the boundary layer.

The validation has been carried out in three steps. The DTC hull tutorial case available in OpenFOAM has been run to see if this model could be a good starting point. Then, the DTMB 5415 geometry has been inserted in the tutorial case and the simulation, named DTMB01, has been performed without any modification. Finally the mesh has been improved to reach a better result. This last model is denoted by DTMB02.

All CFD analyses refer to a model scale ship. The scale factors λ are the ones adopted in experimental tank tests reported in [24] and [25]. For the DTC hull this parameter is equal to 59.4 and, therefore, the scaled model is 5.98m long. For the DTMB 5415, λ is set to 24.8 and the scaled model is 5.72m long.

The DTC hull simulation has been performed at a velocity equal to $\mathbf{U} = 1.668m/s$, which corresponds to a Froude number $Fr = 0.218$. The CFD analyses of the DTMB 5415 have been carried out at a velocity equal to $2.0974m/s$, which corresponds to a Froude number $Fr = 0.28$. The DTMB 5415 has been positioned on the free surface considering its dynamical trim and sinkage. These data are available in [24].

The simulation of the DTC hull tutorial case has led to results in good agreement with experimental data, as can be seen in Table 3.12. The following step has been the simulation of the DTMB 5415 geometry using exactly the same settings as in the DTC hull case. This has been possible because the DTC hull model and the DTMB 5415 model share similar dimensions. This simulation, DTMB01, has given a good prediction of the drag force – see Table 3.12. However, by comparing the wave profile at a certain distance from the ship's longitudinal axis obtained through CFD and the one provided by tank tests, significant discrepancies in the peak zones can be noticed. In order to improve this aspect, the refinement process of the mesh construction has been slightly modified by changing the dimensions of the refinement boxes. These modifications have led to a better wave profile with the drawback of increasing the number of mesh elements – these are

reported in Table 3.12 – and, therefore, the computational time.

Case	N_{pre} [-]	N_{post} [-]	CFD drag [N]	Experimental drag [N]	Error (%)
DTC	513 216	848 025	15.82	15.92	0.6
DTMB01	513 216	896 917	22.33	22.58	1.1
DTMB02	907 200	2 356 423	22.86	22.58	1.2

Table 3.12: Results of the CFD simulations. N_{pre} and N_{post} denote respectively the number of mesh elements before and after the execution of `snappyHexMesh`.

The flow field of this new model, DTMB02, has been studied and compared with the experimental one. The main hydrodynamic phenomena are caught by the CFD analysis while some smaller vortex structures cannot be noticed on the simulation’s contour. To catch them properly, a further increase of the number of cells would have been necessary. The DTMB02 model has been considered to be a good compromise between accuracy and computational time. This choice has been supported by the final purpose of this thesis, which is the study of the influence of some geometrical features on the ship’s performance: the quantity upon which the attention will be focused is the drag force, which is reasonably well predicted by the DTMB02 model. The DTMB01 provides a good estimation of the resistance too. Nevertheless, the DTMB02 model has been preferred because it provides a better approximation of the wave pattern which, as shown in Chapter 1, has a strong influence on the drag. Therefore the DTMB02 numerical model has been considered to be validated for the purposes of this thesis.

CHAPTER 4

GEOMETRY PARAMETRIZATION

Ship design changed considerably over the recent few years. The traditional approach was based on the designer's experience and know-how and was basically a trial and error process. The design was guided by empirical rules and some empirical methods were available to roughly predict the performance of the ship. Then tank tests were a fundamental step to check and verify the design. Today, thanks to the introduction of CFD analysis, the process has become much more flexible. Numerical simulations may provide all sorts of data in few hours, hence it is possible to try different configurations and to choose the best one. In this respect, optimization techniques, based on geometry parametrization, are useful tools: the shape of the hull has to be described by a small number of parameters which can be used to generate new ship geometries. This chapter deals with this issue: traditional and innovative modeling strategies are summarized and a parametrization for DTMB 5415 is proposed. A brief description of the traditional design process is also provided for the sake of completeness.

4.1 TRADITIONAL HULL FORM DESIGN

To begin with, a brief summary of the main principles of ship's design is useful to gain a better understanding of the following sections. The classical design process is carried out through three steps. Firstly, the main dimensions are established; secondly, the values of some coefficients are imposed in order to satisfy all the requirements; finally, the shape of the so-called sectional area curve or SAC curve is defined and the hull's geometry is modeled. Often the process is iterative.

4.1.1 MAIN DIMENSIONS

The main dimensions of a ship, which are shown in Figure 4.1, are length (L), breadth (B), draught (T), depth (D) and free-boards (F). These have to be set such that the hull displaces a prescribed volume of water ∇ according to the following relation:

$$\nabla = L \cdot B \cdot T \cdot c_B \quad 4.1$$

where c_B is the block coefficient, implicitly defined by this relation. The first stage of ship design is therefore the estimation of the displacement weight $\Delta = \rho \nabla$, where ρ is water density. The displacement weight is a function of the ship's type and owner's requirements.

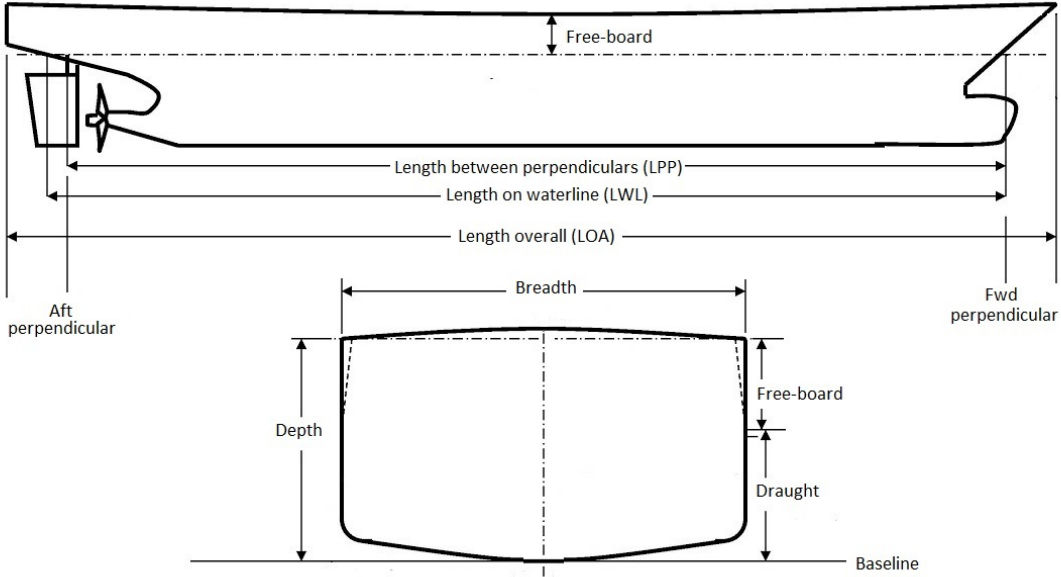


Figure 4.1: Main ship's dimensions.

Once the ship's displacement has been established, the proper combination of ship's dimensions has to be chosen in order to satisfy equation 4.1. The solution is not unique, so other arguments are needed to choose the best configuration. These concern the influence of ship's dimensions on performance and economic efficiency and the possible presence of constraints. The aspects which have to be taken into consideration are hydrodynamic characteristics, fuel consumption, stability, hold capacity, structural strength and construction cost. Constraints deal with the size of ports, canals, slipways and bridges. Some of them are reported in Table 4.1.

Canal	$L_{max}[m]$	$B_{max}[m]$	$T_{max}[m]$
Panama canal	289.5	32.3	12.04
Kiel canal	315	40	9.5
St Lawrence Seaway	222	23	7.6
Suez Canal	-	-	18.29

Table 4.1: Examples of constraints for ship's dimensions [18].

Length: Length has a great influence on the hull's weight, which is strictly related to production costs, and on the hull's drag. Keeping the ship's speed fixed, when length is increased, residuary drag R_R decreases, while friction drag R_F increases because of a higher wetted surface. Hence, an optimum length which ensures the minimum resistance can be reached. This behaviour can be observed in Figure 4.2.

However, length must be considered in conjunction with displacement since there is a mutual influence between these factors. For this reason a parameter which has to be taken into account at this design stage is the *slenderness ratio* defined as L/\sqrt{D} . Figure 4.3 shows the effect of this parameter on the ship's resistance.

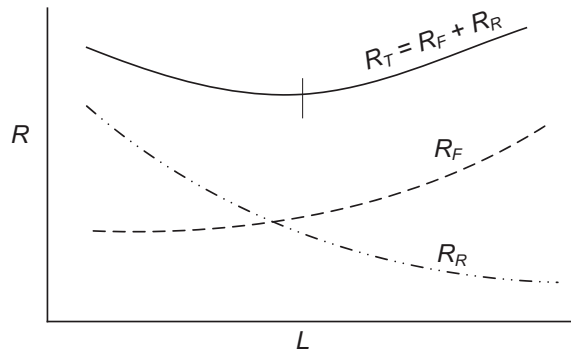


Figure 4.2: Hydrodynamic optimum length [16].

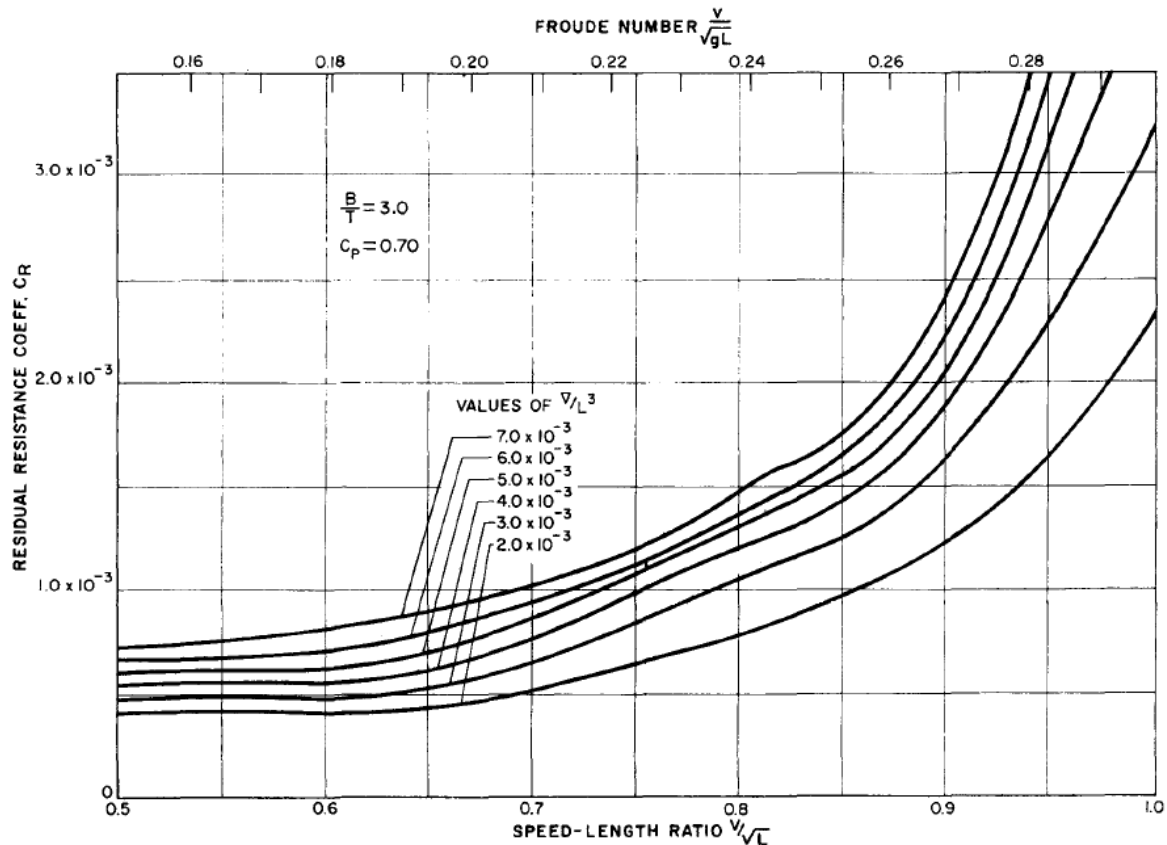


Figure 4.3: Influence of the slenderness ratio on the ship's resistance. Adapted from [26].

There are several approaches to establish the hull's length, but usually the choice is based on a database of similar ships or is guided by empirical formulas which give an estimation of the economic efficiency. For example Schneekluth's formula gives the hull's length that minimizes the construction cost. Once length and cruise speed have been decided, wave interference effects have to be evaluated to verify that cruise Froude's number is favourable.

Breadth: Draught and depth are inversely proportional to breadth. When the value of this parameter is increased, ship's stability grows but resistance grows too. Moreover, draught decreases together with the propeller's dimension, leading to a decrease in the propeller's efficiency. Another aspect to consider is weight, which increases as breadth increases. Hence, usually the minimum breadth which guarantees an adequate stability is chosen.

Draught, depth, free-boards: The value of draught is deduced from Equation 4.1 once c_B has been established (this parameter will be defined in the following section). Depth is useful to adjust the storage capacity of the ship and to guarantee a buoyancy reserve. This is the dimension which has less impact on weight and cost but it affects the mechanical behaviour of the ship: by decreasing this parameter, longitudinal strength decreases.

4.1.2 COEFFICIENTS OF FORM

Coefficients of form are adimensional numbers which have been introduced to relate the hull's shape to its properties. They are strictly related to ship's performance such as resistance, stability, mechanical properties, etc. Usually the designer chooses the value of these parameters by considering a database of similar ships.

- **BLOCK COEFFICIENT:** it is defined as the ratio between the displacement volume of the submerged hull, showed in Figure 4.4, and the parallelepiped with dimensions L , B and T . The analytical definition is the following:

$$c_B = \frac{\nabla}{LBT} \quad 4.2$$

This coefficient is indicative of how the parallelepiped is filled by the submerged hull. A schematic representation is reported in Figure 4.5.

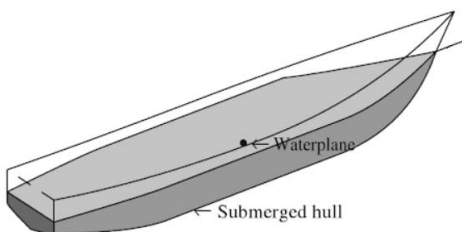


Figure 4.4: Displacement volume of the submerged hull [27].

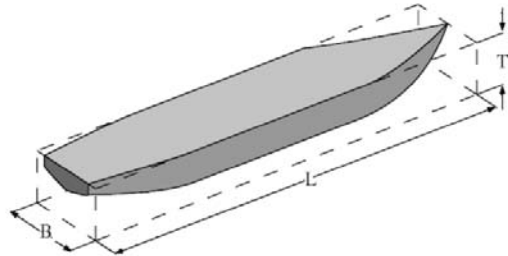


Figure 4.5: Block coefficient [27].

- **MIDSHIP COEFFICIENT:** it is defined as:

$$c_M = \frac{A_M}{BT} \quad 4.3$$

where A_M is the midship section area. The physical meaning of this coefficient can be shown in Figure 4.6.

- PRISMATIC COEFFICIENT: it is the ratio between the submerged displacement volume of the hull and a semi-cylinder of section A_M and length L :

$$c_P = \frac{\nabla}{A_M L} = \frac{c_B}{c_M} \quad 4.4$$

It tells how much the semi-cylinder is filled by the submerged part of the ship. This can be seen in Figure 4.7.

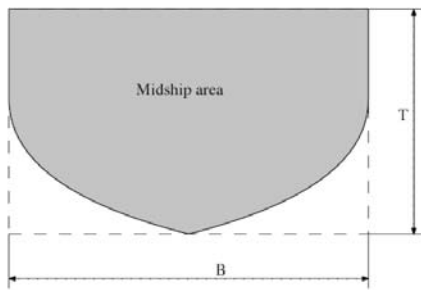


Figure 4.6: Midship coefficient [27].

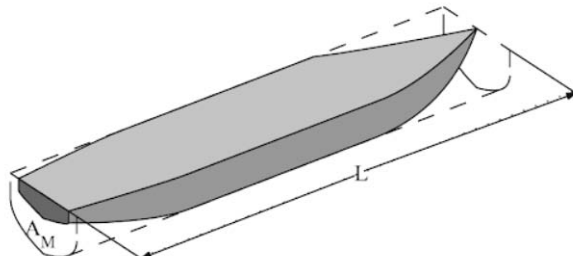


Figure 4.7: Prismatic coefficient [27].

- WATERPLANE-AREA COEFFICIENT: it is defined as follows:

$$c_{WL} = \frac{A_W}{LB} \quad 4.5$$

where A_W is the waterplane area. Figure 4.8 shows schematically its physical meaning.

- VERTICAL PRISMATIC COEFFICIENT: it is defined by the following relation:

$$c_{VP} = \frac{\nabla}{A_W T} \quad 4.6$$

This coefficient is depicted in Figure 4.9.

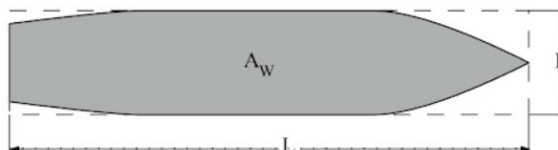


Figure 4.8: Waterplane-area coefficient [27].

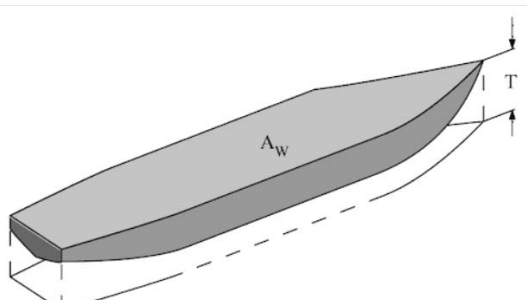


Figure 4.9: Vertical prismatic coefficient [27].

4.1.3 TRADITIONAL MODELING APPROACH

Once the main dimensions and the coefficients of form have been established, the designer has to model the shape of the hull. The first step is the sketch of the sectional area curve or SAC curve. This provides the area of each transversal section of the ship and has to be drawn in order to respect the coefficients of form decided above and the desired displacement. Then the modeling of the hull's shape consists in the lines drawing: the ship is considered as cut by a certain number of parallel planes in order to obtain several bi-dimensional sections in different directions. These sections have to be drawn taking into account the SAC curve and the form coefficients. When the drawing is completed, all parameters have to be evaluated and, if the design presents some discrepancies between the established and the calculated values, the process has to be iterated.

Hull's geometry is defined through cuts in three directions: transversal, longitudinal and horizontal. These sections are called respectively *stations*, *buttocks* and *waterlines* and can be seen in Figures 4.10, 4.11 and 4.12. All resulting bi-dimensional curves have to be drawn in order to satisfy two basic principles: they have to be *coordinated* and *smooth*. The first requirement concerns the respect of the rules governing projections in descriptive geometry while the second means that the curves must be regular and "pleasing to the eye", with no abrupt changing in curvature when no required. Hull's curves that fulfil these two conditions are said to be *fair*. In Figure 4.13 an example of lines drawing is reported.

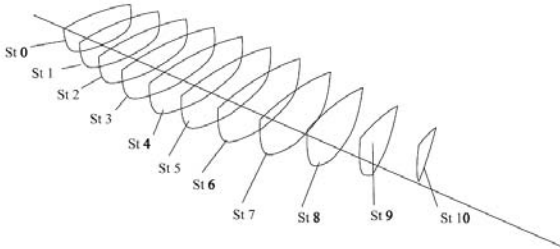


Figure 4.10: *Stations* [27].

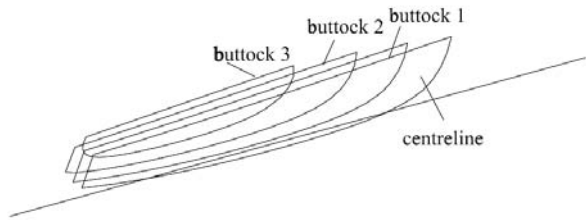


Figure 4.11: *Buttocks* [27].

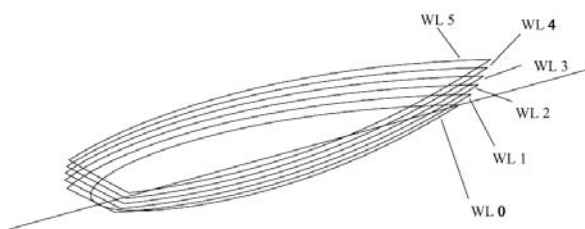


Figure 4.12: *Waterlines* [27].

When ship's drawings were done by hand, it was not straightforward to obtain smooth curves because for example an error of 0.1mm in a $1 : 200$ scaled sketch would have meant an error of 20mm in the full-scale hull. For this reason, in the final step a $1 : 1$ drawing was prepared to correct errors and conclude the fairing process. Later, magnifying glasses

were adopted to draw the curves and the final sketch was photographed on a glass plate and projected above the workshop to enable a more precise cutting. Nowadays, the fairing process is easier thanks to computer-aided design softwares (CAD) which offer a lot of useful tools like algebraic-defined curves, curvature calculations, rendering, etc. A lot of different modeling methods are available with different advantages and drawbacks. The following section is focused on this aspect of the design process.

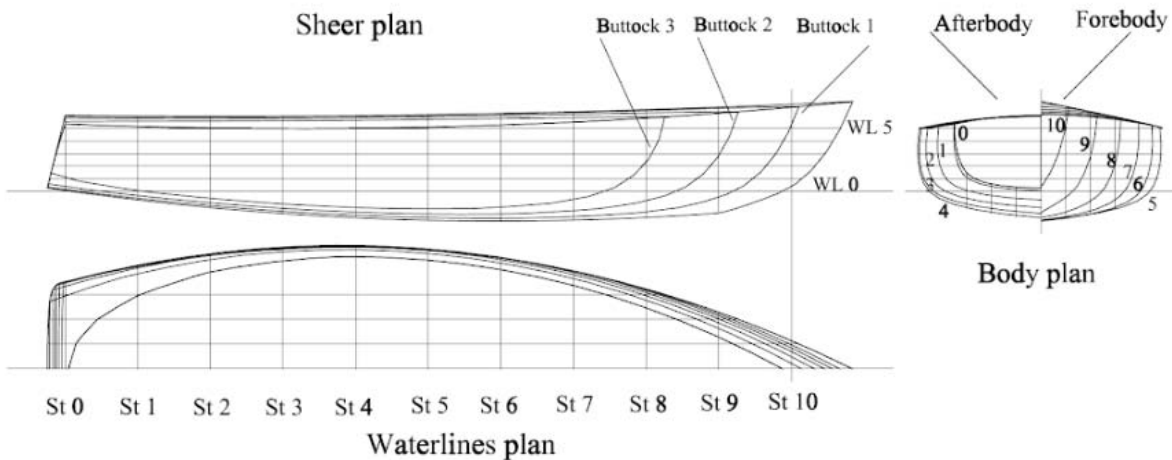


Figure 4.13: An example of lines drawing [27].

4.2 MODERN MODELING METHODS

In this section, modern modeling techniques are introduced and discussed focusing on the most suitable ones in an optimization process. The choice of a good modeling method is essential in optimization problems, as it directly influences the goodness of the results. Some methods are more flexible, allowing a great variability of the shape and, therefore, a better exploration of all the possible design configurations. Others instead are less flexible but more efficient, as they provide the possibility of modifying the geometry by working on only a few parameters. In [28], flexibility and efficiency are defined respectively as "the ability to cope with any possible shape" and "the swiftness with which information (here geometry) is generated". Usually these are competing goals: the choice of the modeling method depends on the aim of the study at hand and often a compromise between these two objectives is pursued. Figure 4.14 classifies the most common modeling methods according to their performance.

In Figure 4.15 a possible classification of the main modeling approaches is depicted. These are basically divided into two groups: conventional and parametric methods. In the former ones the coordinates of the geometric objects are provided by functions, while in the latter ones by equations which involve one or more independent variables called parameters.

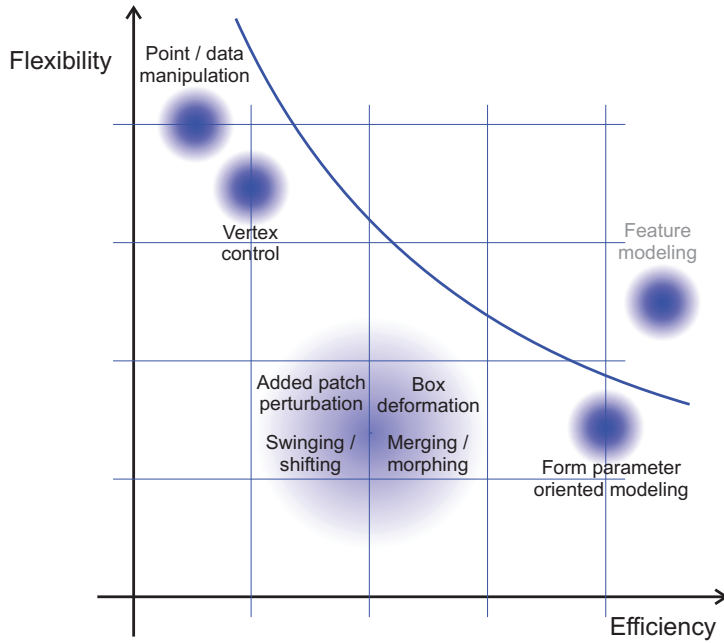


Figure 4.14: Qualitative assessment of flexibility vs. efficiency in geometric modeling [28].

- CONVENTIONAL MODELING:

These modeling approaches are based on a low-level definition of geometry and consist in defining points to build curves and, eventually, surfaces. This procedure is the natural development of the traditional modeling approach described in Section 4.1.3. To modify the shape of an object, the designer can move the single points but there is no control on the relevant feature of the ship geometry such as length, wetted surface, immersed volume and so on. Surfaces may also be modeled directly through the definition of a polyhedron of vertices. These are the so-called Bezier and B-spline surfaces whose shape can be modified by working on the vertices' positions. Also in this case, the effects of the modifications cannot be properly controlled. The advantage of these approaches is a good flexibility: geometries can be varied indefinitely, so an infinite number of alternatives could be ideally evaluated. However, to define the hull's shape, a huge number of control points is required and this results in a high computational effort both to create and to modify objects. Moreover, when shapes are modified, it is not straightforward to obtain smooth geometries: a lot of constraints are needed to guarantee this property, further complicating the problem.

- PARAMETRIC MODELING:

Here geometric objects are created through the definitions of parameters, which can be lengths, angles, volumes, areas and so on. These can be user-defined or computed from a formula, they might depend on certain conditions or can be determined from a set of equations. Geometries are therefore described by high-level entities, which are strictly related to the problem at hand, allowing a better control on the effects of shape modifications. Moreover the production of geometric variation become much more efficient and time saving. The main disadvantage is a lower flexibility: only relatively small modifications are possible.

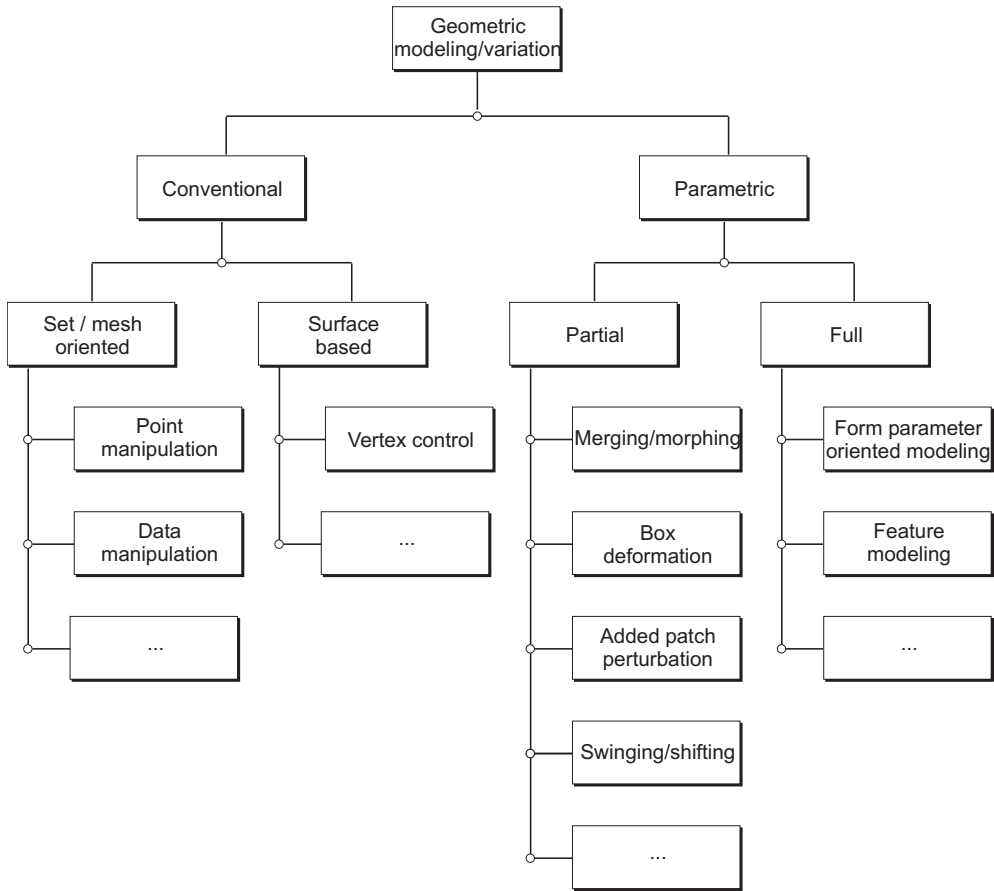


Figure 4.15: Classification of modeling methods [28].

Partial parametric approaches lie somewhere in between conventional and parametric modeling methods, as they consist in applying a parametric modification to a non-parametric object. Examples are listed in Figure 4.15. In Figure 4.14 it is possible to observe that they represent an excellent compromise between flexibility and efficiency. For this reason, some of these methods will be introduced and briefly described in the following section and one of them will be adopted in Section 4.3 to produce DTMB 5415 variations.

4.2.1 PARAMETRIC HULL FORM VARIATIONS

The most used global parametric shape modification method in naval applications is the *Lackenby transformation* or *shifting method* developed by Lackenby in 1950. In this section a short overview of this technique is provided. Another geometry variation approach, which can be used either to obtain local and global modifications, is the *free form deformation (FFD) method* proposed by Sederberg and Parry in 1986. This technique is versatile and offers great advantages, however it is still not very popular in naval applications. A brief description of this method is reported below.

Lackenby transformation: It is a global parametric shape variation method which consists in modifying the sectional area curve form by moving the stations of the initial hull along the longitudinal direction. This means moving the displacement volume of the ship forward or backwards producing a variation of the prismatic coefficient. The position of the centre of buoyancy and the length of the parallel mid-body are also changed through this operation, leading to different hydrodynamic characteristics. The transformation is formally described as follows:

$$f^n(x) = f^0(x) + g(x, \alpha_1, \alpha_2) \quad 4.7$$

where $f^0(x)$ is the function defining the initial shape of the sectional area curve, $f^n(x)$ is the modified shape, $g(x, \alpha_1, \alpha_2)$ is the function which realizes the transformation, called *shape function*, and α_1, α_2 represent respectively the sectional area curve slope and the location of the fixed stations. An example of shape function is reported below and the corresponding transformation is showed in Figure 4.16.

$$g(x, \alpha_1, \alpha_2) = \begin{cases} \alpha_1 & 0.5 & 1 - \cos 2\pi \frac{x - \alpha_2}{\alpha_2 - x_1} & \text{if } x_1 < x < \alpha_2 \\ -\alpha_1 & 0.5 & 1 - \cos 2\pi \frac{x - \alpha_2}{\alpha_2 - x_2} & \text{if } \alpha_2 < x < x_2 \\ 0 & & & \text{elsewhere} \end{cases} \quad 4.8$$

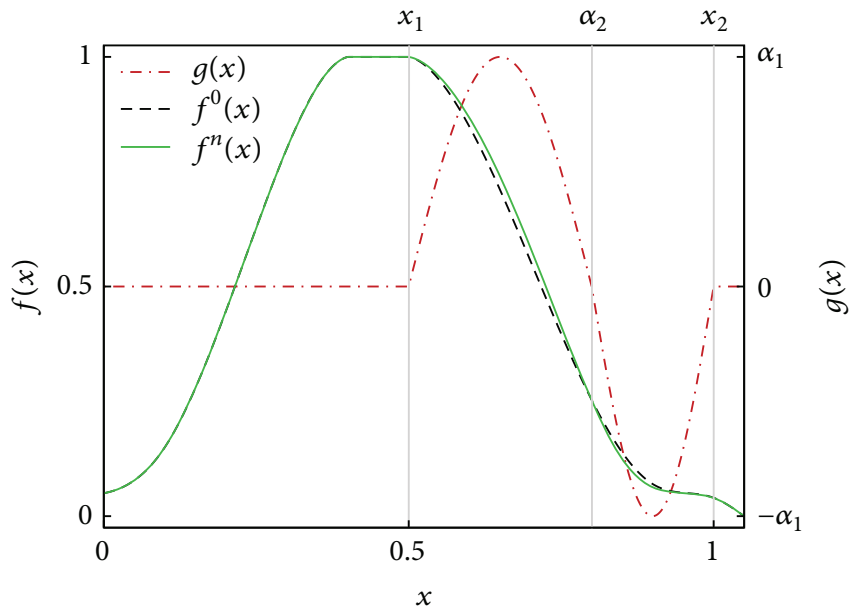


Figure 4.16: Example of a Lackenby transformation [29].

Free form deformation method: This shape modification technique consists in the creation of a grid of points around the geometric object. This grid is then connected to the object, so that when its vertices are moved, a variation of the object's shape is produced. Mathematically, this transformation is based on trivariate Bernstein polynomials and is obtained through the following steps.

Firstly a local coordinate system STU is defined. Each point \mathbf{P} of the geometric object may be expressed in the global space as:

$$\mathbf{P} = P_0 + s\mathbf{S} + t\mathbf{T} + u\mathbf{U} \quad 4.9$$

where s , t and u are the point's coordinates in the local system. These can be easily found by using linear algebra.

Then a three-dimensional grid is defined around the object: its vertices \mathbf{P}_{ijk} form $l+1$ planes in \mathbf{S} direction, $m+1$ planes in \mathbf{T} direction and $n+1$ planes in \mathbf{U} direction and can be expressed in the global system as:

$$\mathbf{P}_{ijk} = P_0 + \frac{i}{l}\mathbf{S} + \frac{j}{m}\mathbf{T} + \frac{k}{n}\mathbf{U} \quad 4.10$$

Finally the transformation is performed by moving the vertices of the grid: the new position \mathbf{X}_{ffd} of an arbitrary object's point \mathbf{X} is found by evaluating the vector valued trivariate Bernstein polynomial as follows:

$$\mathbf{X}_{ffd} = \sum_{i=0}^l \sum_{j=0}^m \sum_{k=0}^n (1-s)^l i s^i (1-t)^m j t^j (1-u)^n k u^k \mathbf{P}_{ijk} \quad 4.11$$

The control points \mathbf{P}_{ijk} are, therefore, the coefficients of the Bernstein polynomial. Other polynomial bases could be used to obtain this deformation as well.

The procedure is schematically depicted in Figure 4.17. Further informations can be found in the original paper by Sederberg and Parry [30].

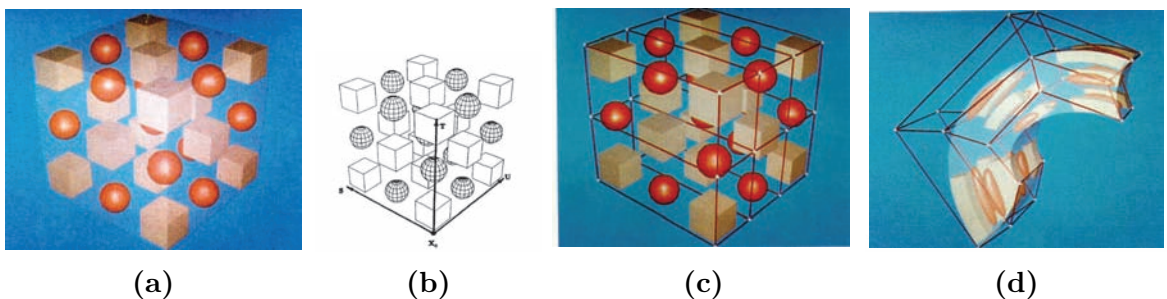


Figure 4.17: Free form deformation method. In (a) the initial object, in (b) the local coordinate system, in (c) the three-dimensional grid, in (d) the grid is modified and the object deforms accordingly [30].

4.3 PARAMETRIZATION OF DTMB 5415

Since the aim of this thesis is to study and improve the hydrodynamic performance of DTMB 5415, the geometry of the ship has to be parametrized in order to produce efficiently different shapes by using a small number of variables. Then these new ship geometries will be analysed through the CFD model validated in Chapter 3 to understand how each variable influences the hull's behaviour. This study will be performed in Chapter 5.

It has been decided to focus the attention on two details of ship's geometry: the bulbous bow and the transom stern. Hence, a local parametric shape modification technique is needed.

For the reasons explained in the previous sections, the free form deformation method has been adopted to produce variations of the bulb's shape. In fact, this approach represents a good compromise between flexibility and efficiency: a lot of different geometries can be produced by using only a few number of parameters.

For the stern, the literature suggests that the most influential geometry's feature is the depth of the transom region. Free form deformation has proven unsuitable to act on this variable, hence a conventional approach – such approaches have been described in Section 4.2 – has been used: stern's geometry has been reconstructed with points and lines, taking as variable the z-coordinates of the points.

The parametrization of the geometry has been performed by using the commercial software CAESES, since it offers a lot of useful tools for the hull's parametrization and optimization. For example, the free form deformation method and the Lackenby transformation are implemented in the software and they are easy to use in CAESES's framework.

4.3.1 PARAMETRIZATION OF THE BULBOUS BOW

The method adopted to produce different bulb's geometries is, as said, free form deformation. In CAESES, this technique may be applied through the following steps.

1. *Creation of the deformation box:* it is the three-dimensional grid whose function has been explained in Section 4.2.1. Users may decide the number of control points along each direction. Figure 4.18 shows the deformation box defined for the bulb of DTMB 5415: it counts 12, 5 and 10 points along x , y and z directions respectively.
2. *Selection of the control points:* users can decide which points of the grid have to be moved to realize the deformation. This is useful in particular to guarantee the surfaces to be continuous, tangent or characterized by the same curvature. For the problem at hand, the same curvature has been imposed along z direction and the same tangent along x direction, deselecting respectively three and two rows of control points.
3. *Definition of the deformation:* at this stage the control points which have been selected can be moved by applying one or more operations. For example scaling or rotating deformations are available.

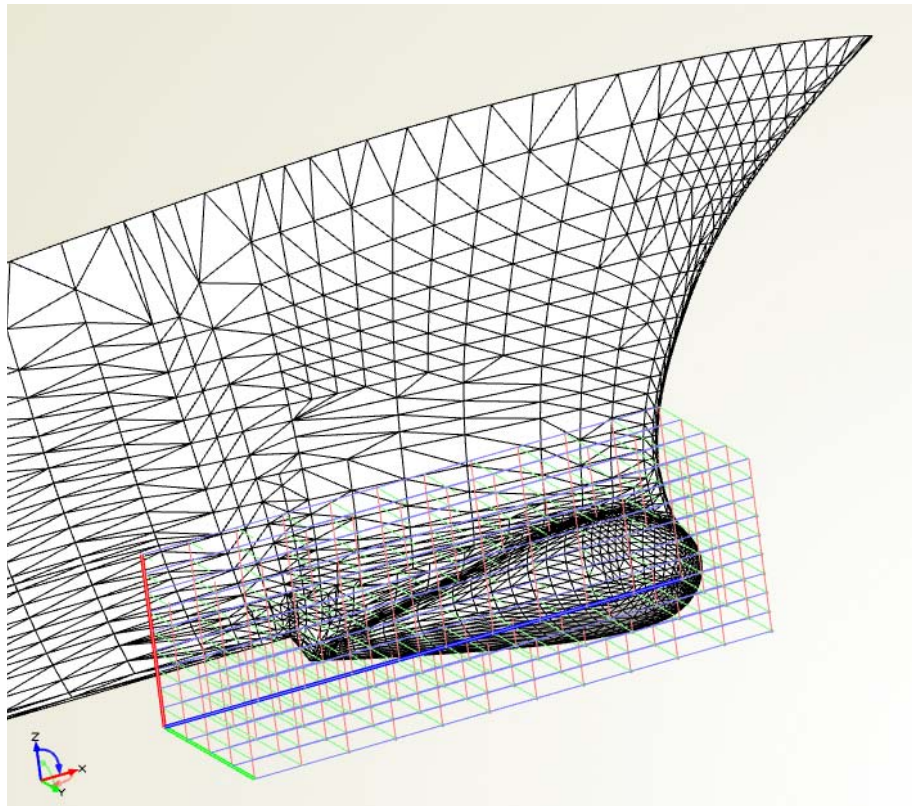


Figure 4.18: Free form deformation grid used for the bulb of DTMB 5415.

For the problem at hand, the variables chosen to control and modify the bulb's form are its length, width, depth and angle.

The first three parameters can be modified by applying a stretch deformation along x , y and z direction respectively. The scale factors applied in the corresponding free form deformations are the design variables, equal to one in the non-deformed configuration.

Instead, a rotation of the control points around the bulb's centre of gravity is applied to modify the angle. In this case, the design variable is the rotation angle which is equal to zero for the baseline.

Figures from 4.19 to 4.24 show, for each variable, the activated control points and an example of deformed configuration. For length and angle, different control points have been selected to extend/shorten the bulb or to apply a positive/negative rotation. This can be seen in Figures from 4.19 to 4.22.

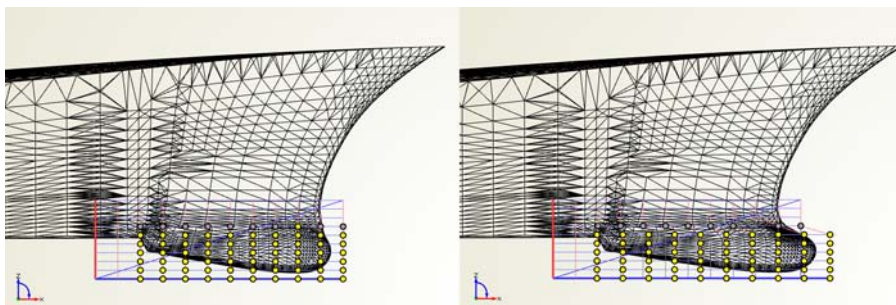


Figure 4.19: Bulb's length, expansion: on the left the selected control points can be seen in yellow, on the right an example of deformed configuration is reported.

Figure 4.20: Bulb's length, contraction: on the left the selected control points can be seen in yellow, on the right an example of deformed configuration is reported.

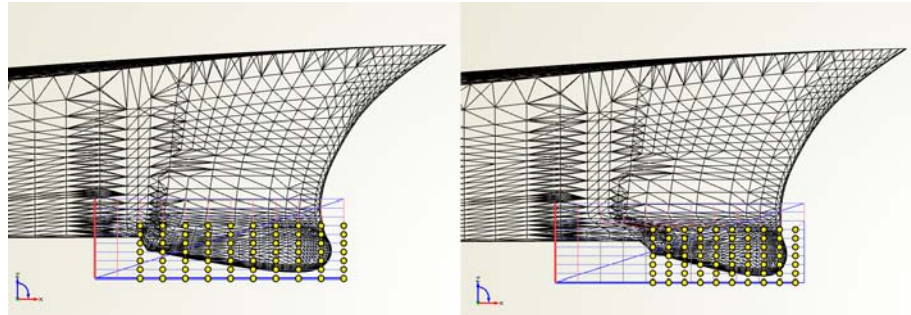


Figure 4.21: Bulb's angle, upwards rotation: on the left the selected control points can be seen in yellow, on the right an example of deformed configuration is reported.

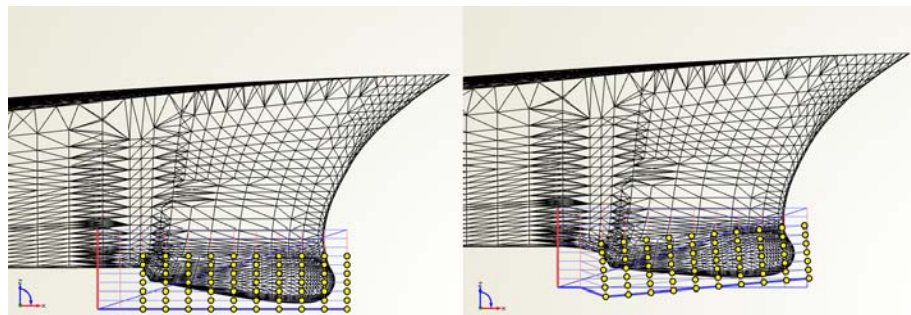


Figure 4.22: Bulb's angle, downwards rotation: on the left the selected control points can be seen in yellow, on the right an example of deformed configuration is reported.

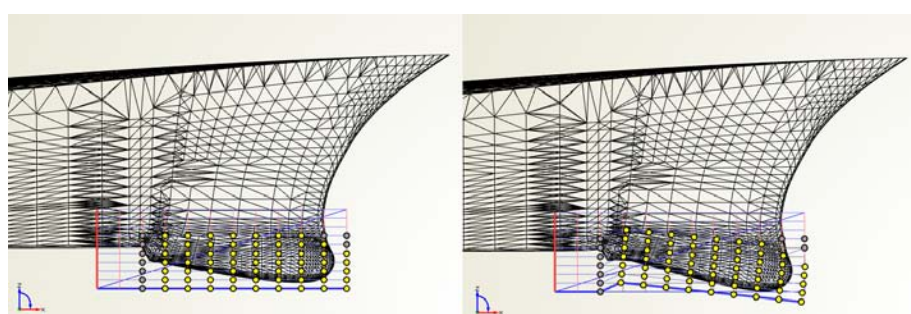
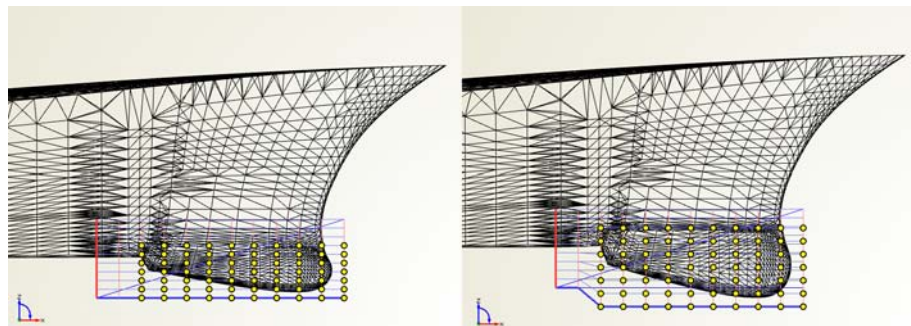


Figure 4.23: Bulb's depth: on the left the selected control points can be seen in yellow, on the right an example of deformed configuration is reported.



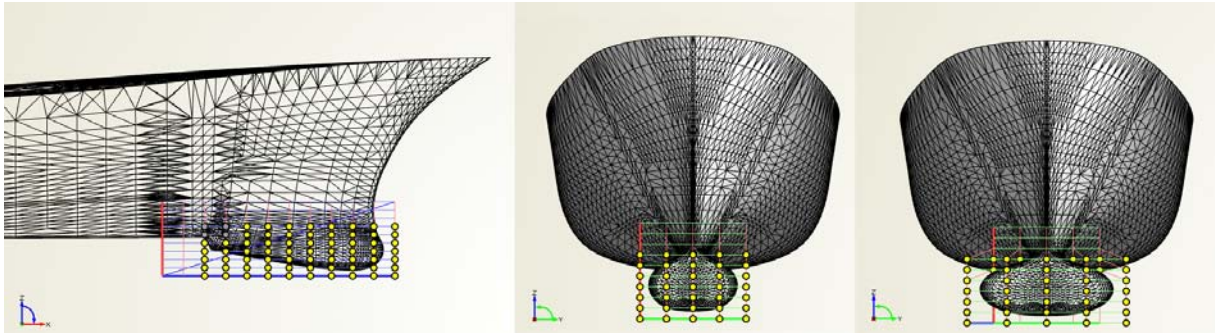


Figure 4.24: Bulb's width: on the left the selected control points can be seen in yellow, on the right an example of deformed configuration is reported compared to the baseline.

4.3.2 PARAMETRIZATION OF THE STERN

The parametrization of the stern of DTMB 5415 is obtained by using a conventional approach where the stations of the forebody are extracted and used to rebuild the geometry. The proceeding is the following.

1. *Extraction of the forebody's stations*: the stations of the forebody are extracted by cutting the hull with 7 parallel planes. The last curve is simply extrapolated from the initial geometry. In this way, 8 curves are obtained.
2. *Selection of the control points*: some points are defined on the curves obtained with the previous operation. The value of the y-coordinates of the points lying on the last station is taken as a design variable: it can be used to modify the transom's depth. When this parameter is varied, the y-coordinates of all the other control points change proportionally.
3. *Reconstruction of the forebody's sections*: the forebody's sections are then reconstructed as NURBS curves by using the above defined control points and other points of the original stations.
4. *Loft surface and closure of the geometry*: a loft surface is created by using the re-built station curves. Then another surface is created to close the stern and the obtained geometry is mirrored with respect to the hull's longitudinal axis.

Figure 4.25 shows details of the stern parametrization. In Figure 4.26 the stern stations can be observed attached to the hull. With this procedure, different ship geometries can be created, characterized by different values of the transom's depth.

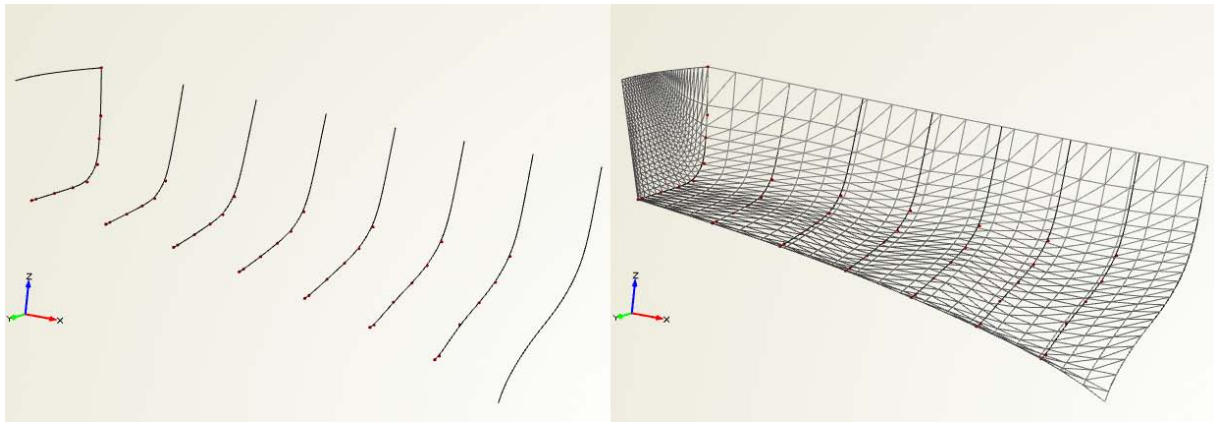


Figure 4.25: On the left, the control points, highlighted in red, and the NURBS curves built upon them; on the right, the loft surface and the surface used to close the geometry.

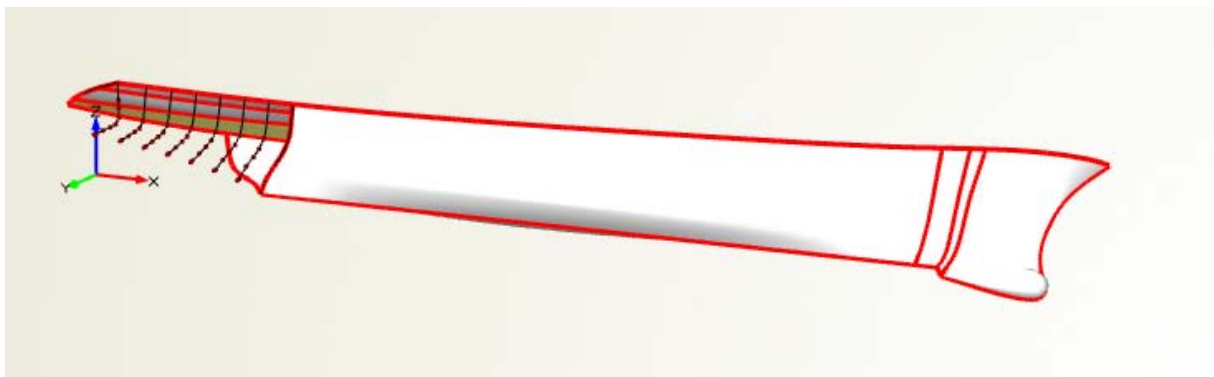


Figure 4.26: Stern stations attached to the hull.

4.4 CONCLUSIONS

This chapter deals with the parametrization of a ship geometry.

Firstly the traditional hull form design process is summarized, to gain a better understanding of the subsequent sections. The attention is focused on its main steps, which consist in establishing the ship's main dimensions and coefficients of form, in the sketch of the sectional area curve and in the lines drawing.

Then the modern modeling approaches are introduced. These can be split into conventional and parametric methods. The former ones are flexible but not efficient, as they require a huge number of control points to define the hull's shape and this results into a high computational effort both to create and modify objects. The latter ones, instead, are more efficient: geometries are described by high-level entities which are strictly related to the problem at hand, allowing a better control on the effects of shape modifications.

Partial parametric approaches, which consist in applying a parametric modification to a non-parametric object, are a good compromise between flexibility and efficiency. Among them, the most commonly used in naval applications is the Lackenby transformation. Instead, the free form deformation method is still not very popular in ship optimization problems but it is versatile and offers great advantages.

The original part of this chapter consists in the parametrization of the DTMB 5415 shape. The attention has been focused on two details of the geometry: the bulbous bow and the transom stern. In fact, as said in Chapter 1, both these elements influence strongly the hydrodynamics of the ship. The parametrization has been carried out by using the commercial software CAESES.

The free form deformation method has been adopted to produce modifications of the bulbous bow. The parameters involved are the bulb's length, width, depth and angle. For width, length and depth, the design variables correspond to the scale factors used to obtain the deformation, hence they are equal to one in the non-deformed configuration. Instead, for the bulb's angle, the design variable is the rotation angle applied to the deformation box, which is equal to zero for the baseline.

The free form deformation method has proven to be unsuitable for the stern parametrization, hence a conventional approach has been used: the stern's shape has been reconstructed by using points and NURBS curves, taking as design variable the z-coordinates of the points. This allows to modify the stern's depth.

The parametrization proposed for the DTMB 5415 does not take into consideration any constraint, i.e. it does not guarantee that the length, the displacement volume and other geometrical features of the modified hulls are kept as in the baseline. In principle, this approach is not correct because the ship's main dimensions influence the hydrodynamic performance and the mechanical behaviour. However, constraints have not been taken into account to simplify the problem. This thesis actually treats all the steps of hull form optimization and is intended to serve as a reference for similar problems. The development of a parametrization method which considers geometrical constraints may be a further development of this work.

CHAPTER 5

DESIGN OF EXPERIMENTS

Once the geometry has been parametrized, it is necessary to estimate how much the different variables influence the performance of the ship. This can be done through a design of experiments and a sensitivity analysis. This chapter briefly summarizes the different possible approaches to deal with this issue. Then a procedure to analyse the specific case study of this thesis is set up and some interesting results are reached.

5.1 WHAT IS A DESIGN OF EXPERIMENTS?

The term *design of experiments* refers to a series of statistical techniques whose purpose is the analysis of a system evaluating how much one or more input factors influence one or more output variables. This can be useful to obtain a deeper knowledge of the system, to understand which are the parameters of greatest interest and to develop theoretical models to predict the behaviour of the system. Montgomery in [31] writes: "Statistical design of experiments refers to the process of planning the experiment so that appropriate data will be collected and analysed by statistical methods, resulting in valid and objective conclusions". Hence, design of experiments consists in methods for setting a series of experiment in order to evaluate the influence of some input parameters on the system response. Usually it consists of two phases: initially a group of individuals to be tested is selected; then, once the dependent variable has been evaluated for each individual, the influence of the input factors on the system is estimated. These two steps are called *sampling* and *sensitivity or uncertainty analysis*. However, design of experiment is a very complicated field: the list of methods and approaches considered in this chapter is far from being complete.

Design of experiments methods may be helpful in many engineering branches. Some typical applications, listed in [31], are: the evaluation and comparison of basic design configurations, the evaluation of material alternatives, the selection of design parameters so that the product will work well under a wide variety of field conditions, the determination of key product design parameters that impact product performance and the formulation of new products.

In this thesis, a design of experiments method is used to sample a certain number of different hull's shapes by changing the values of the variables defined in Chapter 4 and to estimate how these variables influence the ship's resistance. To evaluate the drag force associated to each individual of the sample, the geometries have been tested on a CFD analysis based on the DTMB02 model, which has been validated in Chapter 3.

5.1.1 SAMPLING TECHNIQUES

The aim of the sampling step is to generate a sequence of inputs to study the objective function at hand. This phase is fundamental to perform a sensitivity analysis, whose quality and computational cost strongly depend on the sampling method adopted. The sensitivity analysis must satisfy two requirements: on the one hand, there is the need to explore the variation ranges of each variable thoroughly in order to achieve an adequate knowledge of the system; on the other hand, the computational expense cannot be excessively high so the number of sampling points required has to be as small as possible. To fulfil these two conditions a proper sampling method has to be chosen.

A lot of sampling methods are available. The simplest is the so-called *random sampling*. This technique situates the sampling points randomly throughout the variable's domain. However, the locations of points are determined by the random number generator of the computer and, for technical aspects, they cannot be exactly random leading to a distribution of points which is not uniform in the variables' space. Clusters and gaps are present and this may compromise the goodness of the sensitivity analysis. To reduce the associated uncertainty by a factor of 10, the number of sampling points has to be increased by a factor of 10^2 causing a considerable raise of the computational effort.

Quasi-random sampling methods have been developed to improve the distribution of points in the variables' space. Here the locations of points are established with a much more complex algorithm than the basic random points generator. The most common algorithms are the Halton and the Sobol sequences. Figure 5.1 shows how the same number of points is distributed according to a random and a Sobol sampling. The great advantage of quasi-random methods is that, unlike in the case of random sampling, the uncertainty of the associated sensitivity analysis decreases with the number of points in the sample.

Other common sampling techniques are the *factorial sampling*, the *latin hypercube sampling* and the *multivariate stratified sampling*. For further details about these methods refer for example to [32].

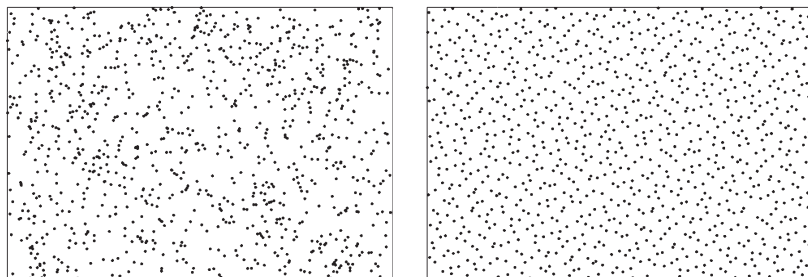


Figure 5.1: Comparison between a random sample, on the left, and a Sobol sample, on the right. Adapted from [33].

5.1.2 SENSITIVITY ANALYSIS METHODS

A sensitivity analysis consists in evaluating the effect of a certain number of factors on a system and how their interactions affect the system response. In the case of an engineering problem, this enables the designer to select only the relevant variables and parameters and, thus, to simplify the design process.

The simplest and basic sensitivity analysis method is the so-called *one-at-a-time* method. It consists in changing the value of one variable at a time, keeping all the others fixed to evaluate the output variation and, thus, the effect of each single factor on the system output. Although this approach is very easy to understand, it enables only a local study of the variables' domain because it requires the choice of a starting point. A global knowledge of the system can be achieved only by increasing significantly the number of output evaluations and, so, the computational cost. Moreover this method is not able to catch the interactions between factors.

Several more accurate sensitivity analysis methods are available. Here the attention is focused on the *analysis of variance* method, as this approach will be used in Section 5.2. Other sensitivity analysis methods are the *elementary effect*, the *derivative based* and the *variance based*. A lot of documentation is easily available on these approaches. Refer for example to [32] for further informations.

Analysis of variance: In engineering problems, a commonly used approach to evaluate the effects of some input factors on a system is the *analysis of variance* or *ANOVA* method. To apply it, factors' ranges are split into a discrete number of levels and data are collected for each factor/level combination. Then, the *F*-test is used to evaluate factors' main effects and interactions.

The simplest case is the *one-way ANOVA* or *single-factor ANOVA*, which studies the effect of only one input variable. Considering a sample of data composed by N observations ($j = 1, \dots, N$) distributed over K levels ($i = 1, \dots, K$), the ij -th observation can be expressed as:

$$y_{ij} = \bar{y} + \epsilon_{ij} \quad 5.1$$

where \bar{y} is the *overall mean* and ϵ_{ij} is a random error which incorporates all other sources of variability in the experiment. The overall mean is a constant term hence all observations are seen as random variations about this parameter. Equation 5.1 is called *reduced model*.

The ij -th observation may also be expressed in an alternative way:

$$y_{ij} = \mu_i + \epsilon_{ij} \quad 5.2$$

where μ_i is the *i-th treatment effect* representing the deviation of the system response from the overall mean when the factor belongs to the i -th level. Equation 5.2 is called *full model*.

If the input factor is significant, the full model represents better the system behaviour. This can be establish through the *F*-test, which consists in the evaluation of the *F* parameter:

$$F = \frac{(RSS_{reduced} - RSS_{full})/(K - 1)}{(RSS_{full})/(N - K)} \quad 5.3$$

where RSS is the residuals sum of squares. "If F is significantly non-zero then the full model has a significantly smaller error variance than the reduced model. That is to say, the full model is a significantly better model, or the main effect of the factor is significant" [34].

To apply the ANOVA method, errors distribution is assumed to be a zero mean Gaussian distribution, i.e. errors are assumed to be normally and independently distributed random variables with zero mean and variance σ^2 . Moreover, the variance σ^2 is assumed to be constant for all levels.

This approach can be extended to a larger number of input factors and to levels as continuous variables – in the just described case the number of levels was discrete. The mathematical demonstration can be found in the literature.

5.2 A DOE FOR THE DTMB 5415

The purpose of this thesis is to study and improve the hydrodynamics of the DTMB 5415 by focusing in particular on the bulbous bow and on the transom stern. To do so, in Chapter 3, a CFD model to analyse the flow field has been validated. Then in Chapter 4, the bow and the stern geometries have been parametrized and some variables have been selected. By changing the value of these variables, it is possible to create new hull geometries which are similar to the baseline, the DTMB 5415, but presents a different bulb and transom shape.

Now a deeper knowledge of how the selected parameters influence the ship's hydrodynamics is requested. To do so, a design of experiment is set up: a sample of new hull geometries is selected and then a sensitivity analysis is carried out. To select new shapes for the hull, the Sobol sampling technique has been adopted because, as it has been said in Section 5.1.1, this method is able to place the sample points uniformly throughout the variables' domain. Then, the results have been studied through an ANOVA analysis, that seems to be particularly suitable to handle with a random or quasi-random sample of points.

Two design of experiments have been performed. In the first, DoE1, 40 individuals have been generated and simulated. This analysis has been useful to adjust the bounds of each variables and to draw the first conclusion: one of the parameters has been excluded from the subsequent analysis because of its poor influence on the objective function. Then, a second analysis has been performed, DoE2, to better catch the trends, i.e. how the value of the resistance changes according to the values of the input parameters.

5.2.1 THE FIRST DESIGN OF EXPERIMENTS: DoE1

Variables bounds: The variables involved in DoE1 are the ones defined in chapter 4, that is bulb angle (a), width (w), length (l), depth (d) and stern depth (Δz). It should be recalled that the free form deformation technique has been used to parametrize the bulb. For width, length and depth, the design variables correspond to the scale factors used to obtain the deformation and, therefore, they are expressed as adimensional numbers. Instead the bulb angle and the stern depth are expressed in degrees and meters respectively. Table 5.1 reports the upper and the lower bounds for each variable. Ranges have been set rather wide to enable a proper exploration of the variable's domain. In Figures from 5.2 to 5.6, for each variable the baseline configuration is compared to the geometries obtained by using the upper or the lower bound. By using these settings, 40 different hull geometries have been generated through a Sobol sampling algorithm available in the software CAESES and simulated in OpenFOAM by using the DTMB02 numerical model.

	$a[^\circ]$	$\Delta z[m]$	$w[-]$	$l[-]$	$d[-]$
Lower bound	-5	-0.05	0.5	0.7	0.5
Upper bound	6	0.05	1.5	1.15	1.5

Table 5.1: Variables' bounds in DoE1.

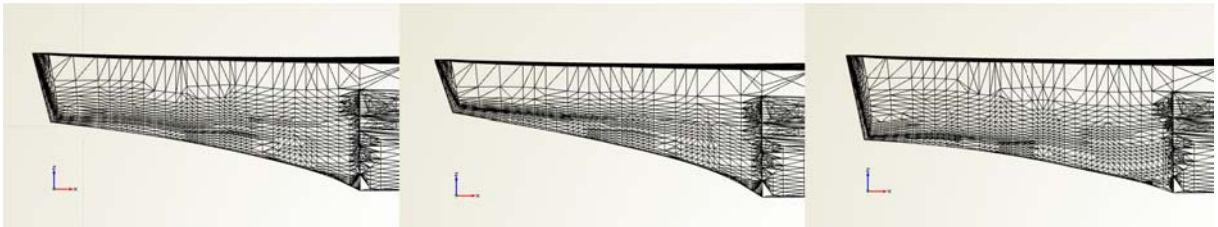


Figure 5.2: Stern depth: from left to right the baseline, the upper bound and the lower bound configurations.

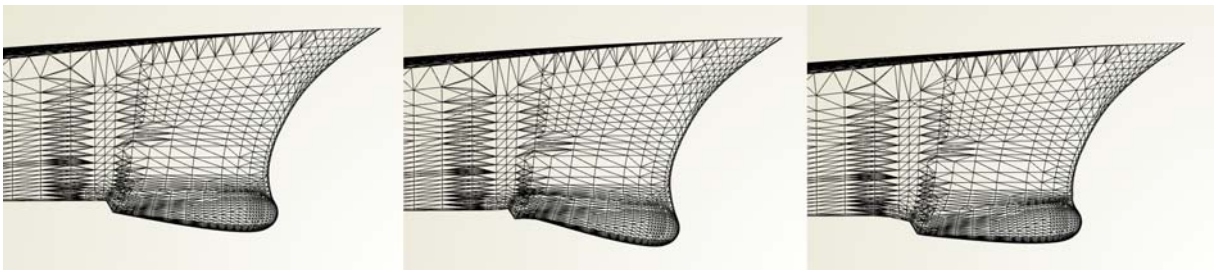


Figure 5.3: Bulb's angle: from left to right the baseline, the upper bound and the lower bound configurations.



Figure 5.4: Bulb's width: from left to right the baseline, the upper bound and the lower bound configurations.

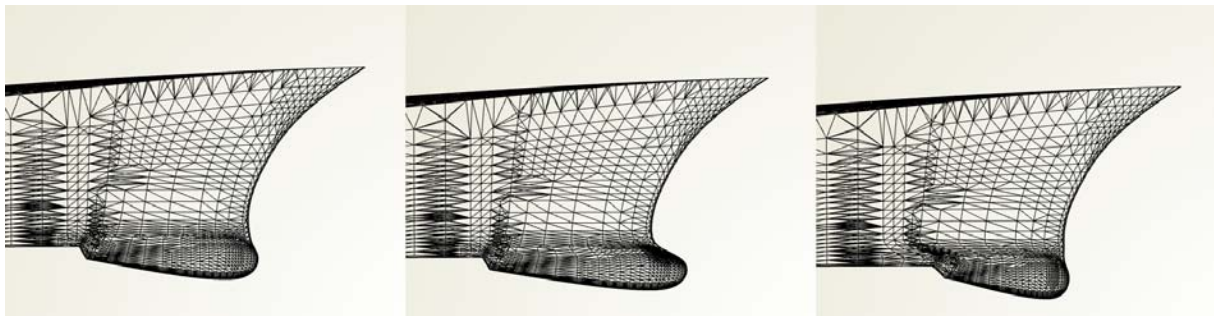


Figure 5.5: Bulb's length: from left to right the baseline, the upper bound and the lower bound configurations.

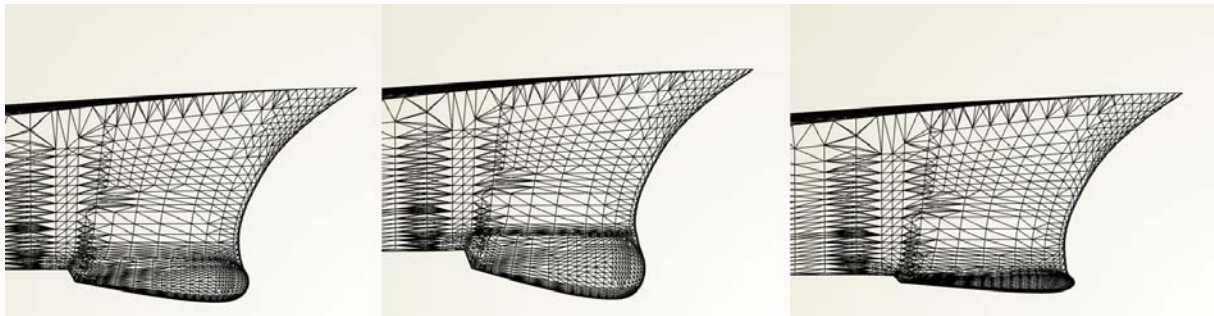


Figure 5.6: Bulb's depth: from left to right the baseline, the upper bound and the lower bound configurations.

Results: Figure 5.7 shows the CFD results of this first design of experiments, reporting in particular for each individual of the sample the values of the total resistance R , the pressure resistance R_P and the viscous resistance R_V as a function of each single variable. This is the simplest method to appreciate the variables' influence on the objective functions and it is a way to depict graphically the main effects of the factors. Instead, interactions between factors cannot be appreciated by looking at these plots. In this figure all quantities are normalized: variables values are between zero and one while resistance values are normalized with respect to the baseline: in each plot, the baseline is represented as a black filled square and its value on the vertical axis is equal to one. Hence each individual that presents a value lower than 1 on the vertical axis has better performance than the baseline and vice-versa.

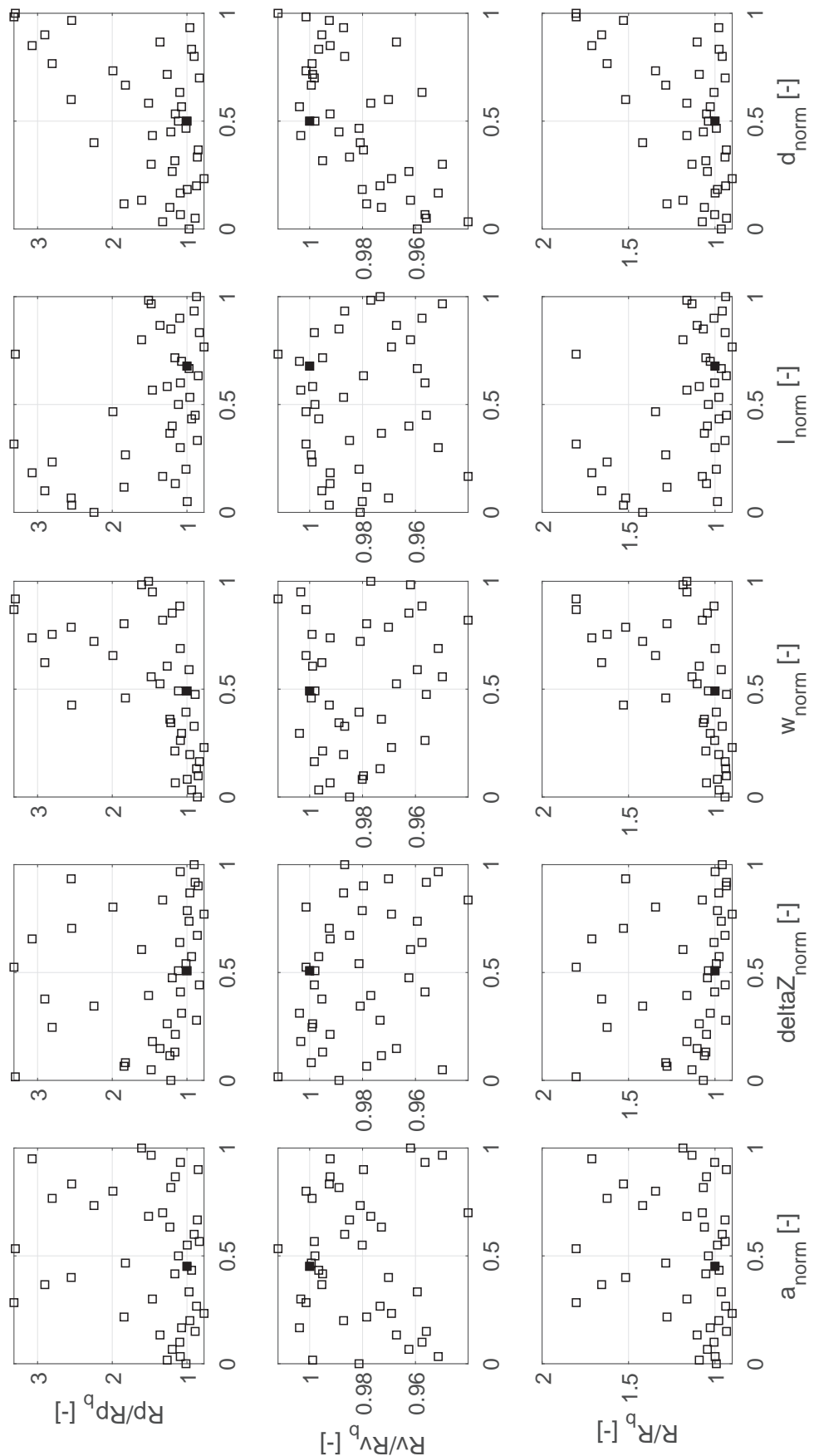


Figure 5.7: Results of DoE1. Variables values are normalized between zero and one. The baseline is represented by the black filled square. R_b denotes the baseline resistance.

Firstly, it is possible to observe that the plots of R_P and R share the same trends because R_V value is similar for all the geometries and does not affect the total resistance. Hence, to analyse the results it is possible to focus on R only. This result can be better seen in Figure 5.8, where the relations between R , R_P and R_V are highlighted.

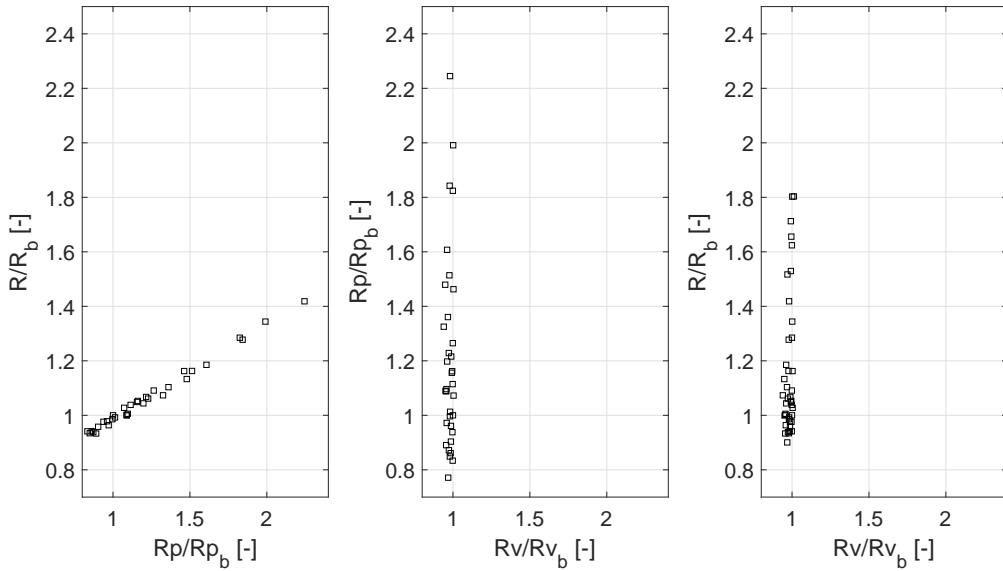


Figure 5.8: Relation between R , R_P and R_V in DoE1.

Then, some informations about the trend of resistance as a function of single parameters may be deduced. The factor that seems to have more influence on the resistance value is the width: resistance grow with it. An ANOVA study based on a linear model has been carried out with the statistical software R to better understand the behaviour of the system. As a first approach to the problem, only the main effects have been considered. The results are summarized in Figure 5.9: the ANOVA table ranks the variables according to their influence on the system, highlighting the more significant factors with a higher number of stars.

Analysis of Variance Table

Response: R					
	Df	Sum Sq	Mean Sq	F value	Pr(>F)
angle	1	70.68	70.68	8.7673	0.005558 **
width	1	465.29	465.29	57.7141	7.952e-09 ***
depth	1	375.62	375.62	46.5921	7.443e-08 ***
length	1	176.90	176.90	21.9433	4.391e-05 ***
deltaZ	1	40.01	40.01	4.9629	0.032619 *
Residuals	34	274.10	8.06		

Signif. codes: 0 ‘***’ 0.001 ‘**’ 0.01 ‘*’ 0.05 ‘.’ 0.1 ‘ ’ 1					

Figure 5.9: ANOVA table for DoE1: degrees of freedom (Df), sums of squares (Sum Sq), mean sums of squares (Mean Sq), F parameters (F value) and p-values (Pr(> F)) are reported for each input variable. Further explanations on the meaning of these parameters can be found in the literature.

It is possible to notice that the stern depth Δz does not have a significant influence on the resistance value. Moreover the flow field in the transom region is highly turbulent and – it has been shown in Chapter 3 – the DTMB02 model is not able to catch the exact form and location of the vortical structures. For these reasons this variable has not been taken into account in the following analysis.

Looking again at the plots in Figure 5.7, it is possible to deduce how the variables' bounds have to be adjusted to perform another design of experiments in order to better catch the trends of the system. In particular, the geometries in width and length plots seem to be clustered near the lower and upper bound respectively. Hence, the width lower bound has to be decreased while the length upper bound has to be raised.

Finally in Table 5.2, a comparison between the characteristics of the best individual of the sample, BEST1, and the baseline is reported. In Figure 5.10 their geometries are showed. BEST1 presents a percentage reduction of the total resistance of 9.94%.

Individual	$a[^\circ]$	$\Delta z[m]$	$w[-]$	$l[-]$	$d[-]$	$R_P[N]$	$R_V[N]$	$R[N]$
Baseline	0	0	1	1	1	7.914	14.949	22.863
BEST1	-2.25	0.025	0.75	1.0375	0.75	6.104	14.486	20.590

Table 5.2: Characteristics of the baseline and of the best individual in DoE1.

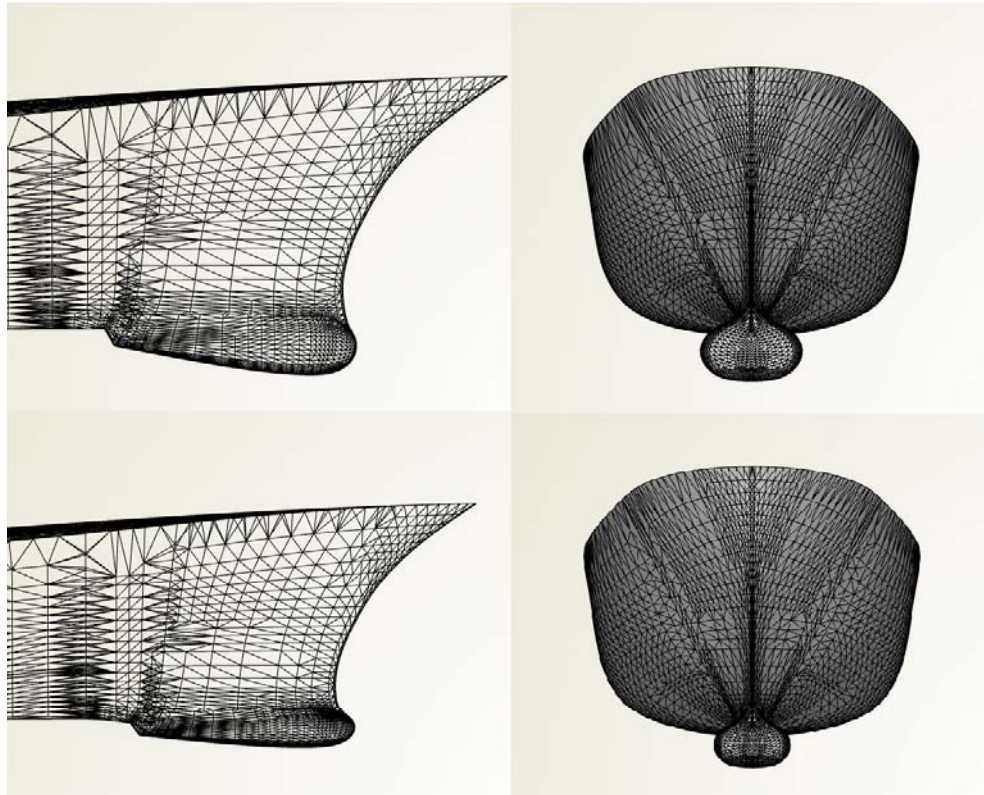


Figure 5.10: Comparison between the shape of BEST1 (second row) and the baseline (first row).

5.2.2 THE SECOND DESIGN OF EXPERIMENTS: DoE2

Variables bounds: The parameters involved in this design of experiments are bulb angle (a), width (w), length (l) and depth (d). The stern depth Δz is no longer considered, as it has been demonstrated to have a negligible effect on the ship's resistance. Variables bounds have been adjusted in accordance with the results of DoE1. Upper and lower bounds are reported in Table 5.3 for each parameter. A Sobol sampling of 60 individuals has been generated in the variables' domain through the software CAESES, then each hull geometry has been simulated in OpenFOAM by using the DTMB02 numerical model validated in Chapter 3.

	$a[^\circ]$	$w[-]$	$l[-]$	$d[-]$
Lower bound	-3.5	0.3	0.7	0.5
Upper bound	5	1.15	1.2	1.5

Table 5.3: Variables' bounds in DoE2.

Results: In Figure 5.12 the results of this design of experiment are reported. All quantities are normalized as in Figure 5.7, which refers to DoE1. The relation between the total resistance R , the pressure resistance R_P and the viscous resistance R_V can be appreciated in Figure 5.11: the same conclusions deduced for DoE1 apply in this case, so the attention can be focused on the total resistance only.

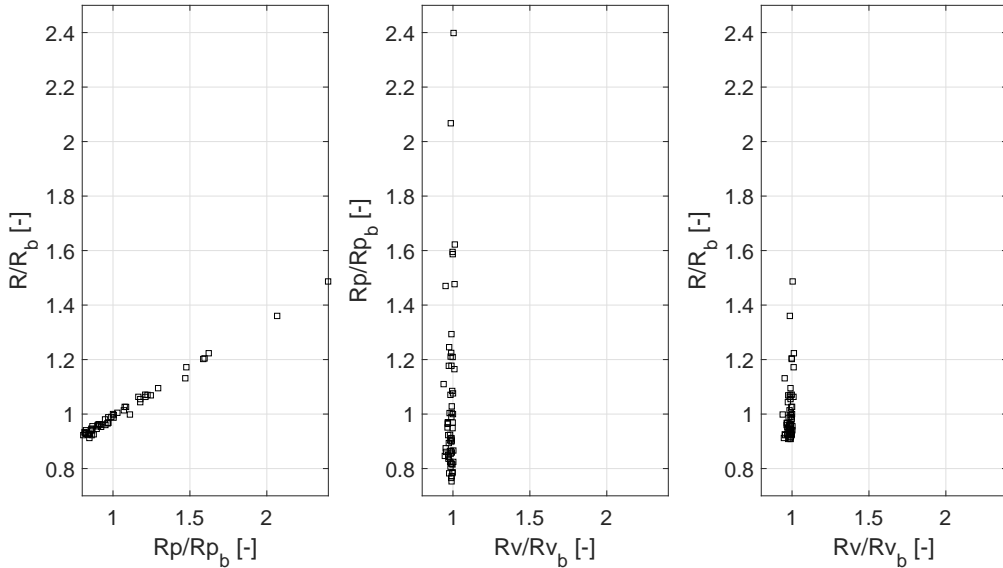


Figure 5.11: Relation between R , R_P and R_V in DoE2.

By examining the plots obtained for DoE2, it is possible to note that this time the trends of R as a function of the single variables are better caught than in DoE1. Hull resistance

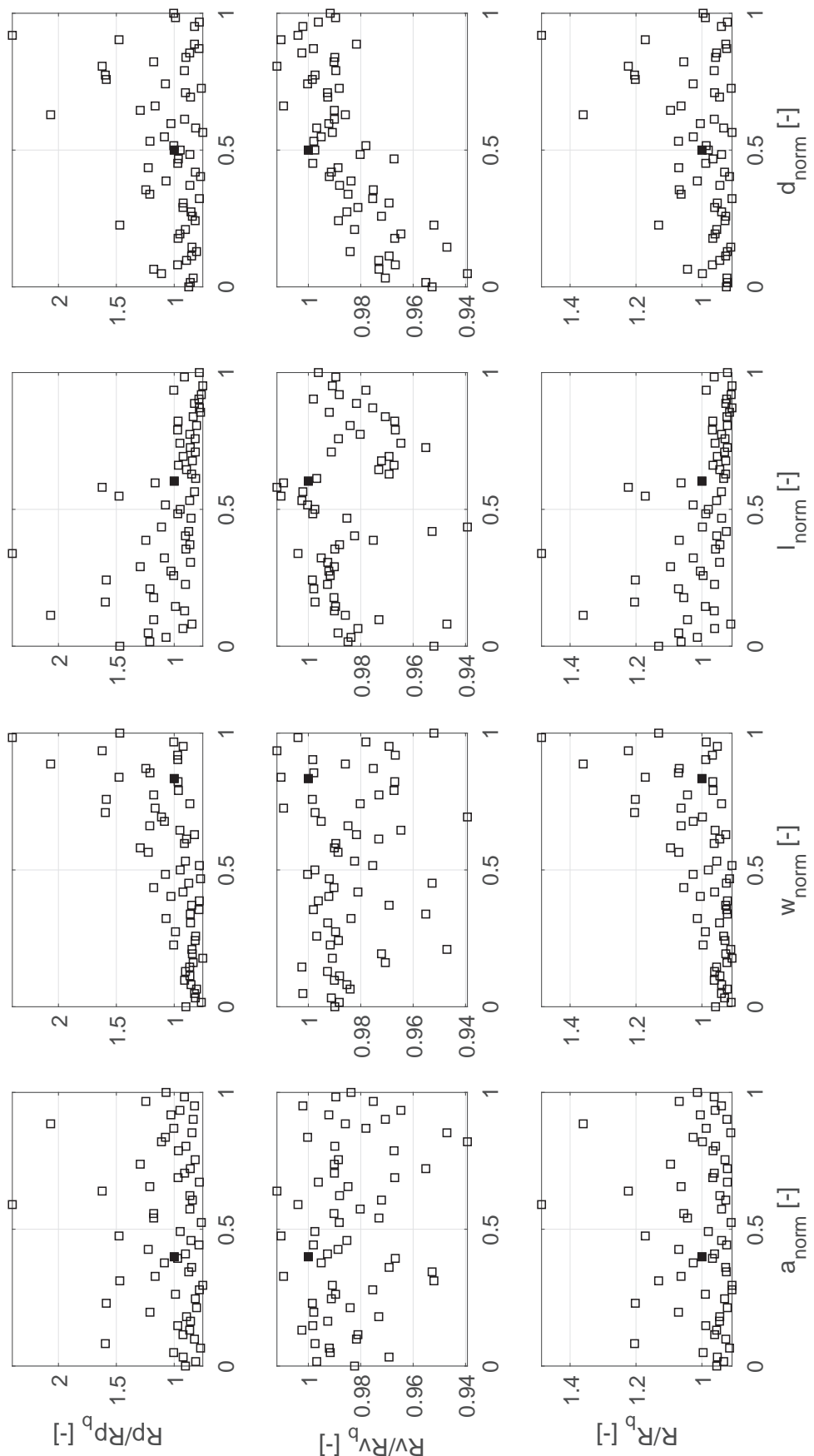


Figure 5.12: Results of DoE2. Variables values are normalized between zero and one. The baseline is represented by the black filled square. R_b denotes the baseline resistance.

clearly grows with the bulb's width and decreases with the bulb's length. The other two parameters seem to have less influence on the ship's resistance.

To better understand these plots, an ANOVA study based on a linear model has been carried out by using the software R. In this analysis, the interactions between input factors have been considered as well. The corresponding ANOVA table is reported in Figure 5.13. As for DoE1 the variables or variables' combinations that mostly influence the system are highlighted with a higher number of stars on the right-hand side column of the table. As suggested by the plots in Figure 5.12, the bulb's angle has a negligible influence on the ship's resistance, both considering main effects and interactions. Instead, the bulb's depth has a significant effect on the system.

Analysis of Variance Table

Response: R						
	Df	Sum Sq	Mean Sq	F value	Pr(>F)	
angle	1	3.535	3.535	3.9793	0.05164	.
width	1	126.785	126.785	142.7195	3.984e-16	***
length	1	65.130	65.130	73.3157	2.671e-11	***
depth	1	47.824	47.824	53.8349	1.996e-09	***
angle:width	1	4.405	4.405	4.9585	0.03059	*
angle:length	1	1.380	1.380	1.5538	0.21850	
angle:depth	1	0.547	0.547	0.6152	0.43660	
width:length	1	34.494	34.494	38.8289	1.029e-07	***
width:depth	1	33.643	33.643	37.8713	1.355e-07	***
length:depth	1	18.496	18.496	20.8207	3.399e-05	***
Residuals	49	43.529	0.888			

Signif. codes: 0 ‘***’ 0.001 ‘**’ 0.01 ‘*’ 0.05 ‘.’ 0.1 ‘ ’ 1						

Figure 5.13: ANOVA table for DoE2: degrees of freedom (Df), sums of squares (Sum Sq), mean sums of squares (Mean Sq), F parameters (F value) and p-values (Pr(> F)) are reported for each input variable. Further explanations on the meaning of these parameters can be found in the literature.

Finally in Table 5.4, a comparison between the characteristics of the best individual of DoE2, BEST2, and the baseline is reported. In Figure 5.14 their geometries are showed. BEST2 presents a percentage reduction of the total resistance of 9.15%.

Individual	$a[\circ]$	$w[-]$	$l[-]$	$d[-]$	$R_P[N]$	$R_V[N]$	$R[N]$
Baseline	0	1	1	1	7.914	14.949	22.863
BEST2	-0.8437	0.4594	1.1687	1.0625	5.96	14.812	20.772

Table 5.4: Characteristics of the baseline and of the best individual in DoE2.

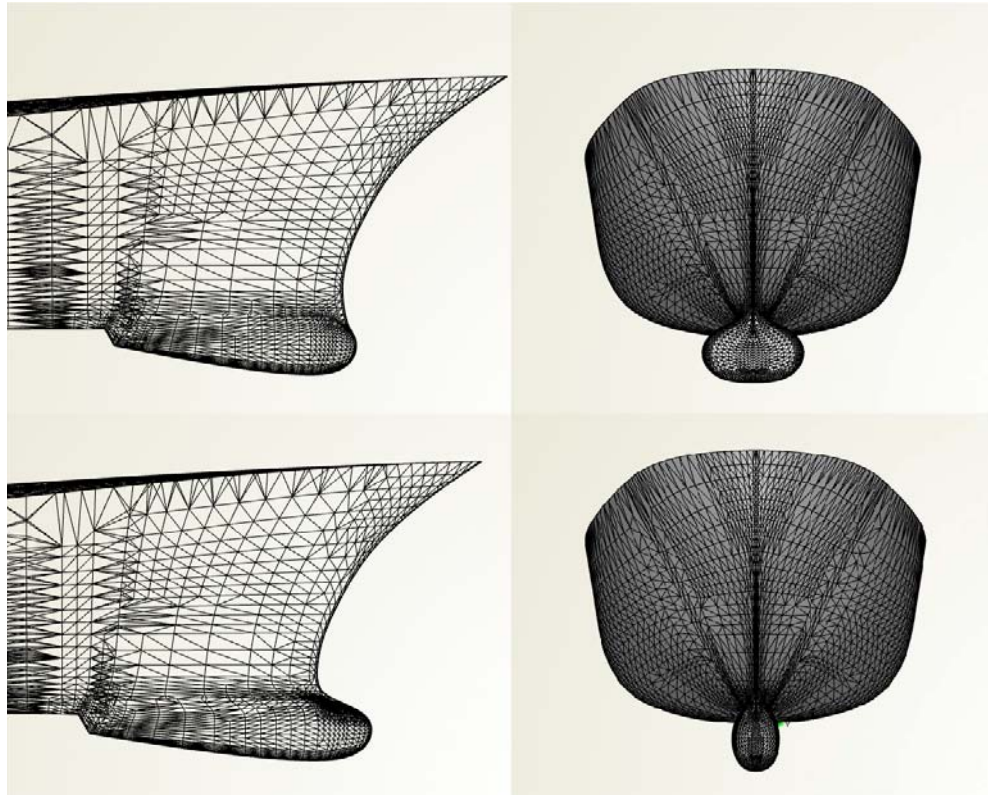


Figure 5.14: Comparison between the shape of BEST2 (second row) and the baseline (first row).

Comparing data reported in Tables 5.4 and 5.2 and hull's geometries showed in Figures 5.14 and 5.10, it is possible to observe that BEST1 and BEST2 present a similar value of the drag force but quite different shapes. Further analyses are then necessary to understand whether a global minimum exists. These will be carried out in the following chapter.

5.3 CONCLUSIONS

This chapter is about design of experiments techniques adopted in engineering problems to evaluate how one or more input factors influence one or more output variables in a physical system.

Usually, a design of experiments consists of two phases: the sampling phase, to select a group of individuals to be tested, and a sensitivity analysis, to evaluate the main effects of factors and their interactions. Here, the attention is focused on the Sobol sampling technique and on the analysis of variance approach, as these methods are then used to perform a design of experiments on DTMB 5415.

The original part of this chapter consists in a design of experiments for the DTMB 5415. The design variables involved in this analysis are the ones selected in Chapter 4, that is bulb angle (a), width (w), length (l), depth (d) and stern depth (Δz). The analysis has been carried out in two phases: DoE1 and DoE2.

In both cases, a sample of individuals has been selected by using the Sobol sampling technique available in the software CAESES. Then, each hull geometry has been tested in OpenFOAM by using the DTMB02 numerical model validated in Chapter 3. The CFD simulations have provided for each individual the values of the total resistance R , viscous resistance R_V and pressure resistance R_P . In both DoE1 and DoE2, viscous resistance has proven a negligible component of the total drag, as the latter and the pressure resistance have shown the same trends. Therefore, the attention has been focused on the total resistance only. Finally, the analysis of variance method, available in the statistical software R, has been used to analyse the results.

The first design of experiments, DoE1, has been performed by using a sample of 40 individuals and setting the variables' ranges rather wide, to enable a proper exploration of the domain. The analysis of variance has been carried out by considering only the main effects. The result has shown that the stern's depth has a negligible influence on the total resistance. Moreover, the flow field in the transom region is highly turbulent and – it has been shown in Chapter 3 – the DTMB02 model is not able to catch the exact form and location of the vortical structures. For these reasons, this variable has not been taken into account in the further analysis. The best individuals of this first design of experiments have been found to be clustered in a region of the variables' domain.

The second design of experiments, DoE2, has been performed by using a sample of 60 individuals and adjusting the variables' bounds in accordance with the results of DoE1. The stern depth Δz has no longer been considered. The effects of the variables on the total resistance have been better caught than in DoE1: hull resistance clearly grows with the bulb's width and decreases with the bulb's length, while the other two parameters seem to have less influence. The ANOVA analysis has been carried out by considering factors' main effects and interactions. The result has shown that the bulb's angle has a negligible influence on the ship's resistance.

Tables 5.5 and 5.6 report the variables' bounds and the characteristics of the best individuals for DoE1 and DoE2. By comparing BEST1 and BEST2 data, it is possible to observe that they present a similar value of the drag force but quite different shapes. Further analyses are then necessary to understand whether a global minimum exists.

		$a[\circ]$	$\Delta z[m]$	$w[-]$	$l[-]$	$d[-]$
DoE1	Lower bound	-5	-0.05	0.5	0.7	0.5
	Upper bound	6	0.05	1.5	1.15	1.5
DoE2	Lower bound	-3.5	-	0.3	0.7	0.5
	Upper bound	5	-	1.15	1.2	1.5

Table 5.5: Variables' bounds in DoE1 and DoE2.

Individual	$a[\circ]$	$\Delta z[m]$	$w[-]$	$l[-]$	$d[-]$	$R_P[N]$	$R_V[N]$	$R[N]$	$\Delta R(\%)$
Baseline	0	0	1	1	1	7.914	14.949	22.863	-
BEST1	-2.25	0.025	0.75	1.0375	0.75	6.104	14.486	20.590	9.94
BEST2	-0.8437	-	0.4594	1.1687	1.0625	5.96	14.812	20.772	9.15

Table 5.6: Characteristics of the baseline and of the best individuals in DoE1 and DoE2. R denotes the percentage reduction of the total resistance.

CHAPTER 6

RESPONSE SURFACES AND OPTIMIZATION

Often, when dealing with problems that involve CFD analyses, computing time is a critical issue. A single simulation may actually require hours to converge, while time-to-market is usually short. Hence, only a small number of simulations can be performed. This problem may be resolved through the construction of a response surface or surrogate model which is able to predict the ship's performance in few seconds. In this chapter, three different regressive models are introduced and used to predict the drag force of new DTMB 5415 geometries. At this point, another problem arises, that is to determine whether a global minimum exists. A lot of optimization techniques are available to handle this issue. Here, a genetic algorithm is used on the surrogate models to find the best DTMB 5415 geometry.

6.1 RESPONSE SURFACES

A response surface is a mathematical model of a physical system. Physical systems are normally characterized by one or more outputs whose values change according to several input factors. The simpler case, which is a system with one output and two inputs, can be represented by the following relation:

$$y = f(x_1, x_2) + \epsilon \quad 6.1$$

where x_1 and x_2 are the input parameters, y is the system's output and ϵ is the error or noise observed in y . The function $E(y) = f(x_1, x_2)$ is the expected response, hence the surface defined as $\hat{y} = f(x_1, x_2)$, shown in Figure 6.1, is called a *response surface*.

In engineering problems the functional relation which links the inputs and the outputs is unknown. Therefore the purpose of the *response surface methodology* is to find a suitable approximation of this function by using several mathematical and statistical techniques.

Once the response surface of the system has been built, some statistical parameters can be calculated to evaluate its accuracy. The main are listed below. Considering a sample of n observations, the known values of the system output are denoted by y_i while the values estimated by the response surface are denoted by \hat{y}_i .

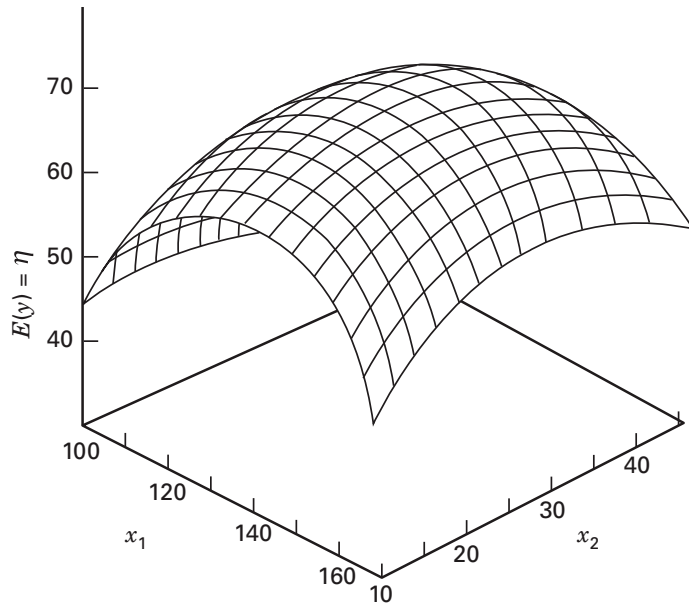


Figure 6.1: Example of response surface. Adapted from [31].

- RESIDUALS: they are defined as the difference between the known and the estimated values of the system output, that is $r_i = y_i - \hat{y}_i$. If the model is adequate, the residuals should be structureless: they should contain no obvious patterns. Hence the graphical analysis of residuals may reveal model inadequacies.
- ROOT MEAN SQUARE ERROR: it is defined by the relation 6.2. It is always a non-negative quantity, and values close to zero mean that the model provides a good approximation of the system at hand.

$$RMSE = \sqrt{\frac{\sum_{i=1}^n (y_i - \hat{y}_i)^2}{n}} = \sqrt{\frac{\sum_{i=1}^n (r_i)^2}{n}} \quad 6.2$$

- COEFFICIENT OF DETERMINATION: it is denoted by the symbol R^2 . The definition is the following:

$$R^2 = 1 - \frac{SS_{res}}{SS_{tot}} \quad 6.3$$

where SS_{res} is the sum of squares of residuals and SS_{tot} is the total sum of squares. These two quantities are defined respectively as: $SS_{res} = \sum_{i=1}^n (y_i - \hat{y}_i)^2 = \sum_{i=1}^n (r_i)^2$ and $SS_{tot} = \sum_{i=1}^n (y_i - \bar{y})^2$, where \bar{y} is the mean value of the sample. The better the model fits the data, the closer the value of R^2 is to 1.

6.1.1 POLYNOMIAL MODELS

The easiest method to predict the response of a system consists in describing its behaviour through a polynomial relation. The simplest case is the *first-order polynomial*, which is used if the function linking the input parameters and the system output is linear. In this case the response surface is defined as follows:

$$y = _0 + _1x_1 + _2x_2 + \dots + _kx_k + \dots + _nx_n \quad 6.4$$

where x_k are the independent variables and $_k$ are the polynomial parameters. This model is able to represent only the main effects of the input factors. If interactions between variables have a significant influence on the response as well, another model is needed to describe the behaviour of the system. In this case the *first-order polynomial with interaction terms*, defined as follows, is suitable.

$$y = _0 + \sum_{i=1}^n _ix_i + \sum_{i < j} _{ij}x_i x_j \quad 6.5$$

If the behaviour of the system is more complicated, a polynomial of higher degree must be used. For example the *second-order polynomial* is defined as:

$$y = _0 + \sum_{i=1}^n _ix_i + \sum_{i=1}^n _{ii}x_i^2 + \sum_{i < j} _{ij}x_i x_j \quad 6.6$$

To obtain a reliable model, the coefficients of the polynomial are estimated by using a certain number of known solutions through the *least square method*.

Polynomial models are very simple, hence it is unlikely that they will be a reasonable approximation of the true functional relationship over the entire space of the independent variables. However, for a relatively small region, they may work quite well.

6.1.2 KRIGING MODELS

A *Kriging model* or *gaussian process model* is a response surface introduced in geoscience by Krige in 1951 to predict the mineral distribution in the subsoil by using soil samplings. It is basically a spatial interpolation method. In the original formulation, the input factors were only two, the spatial coordinates. Later, the method was enhanced as a tool to deal with engineering problems and a formulation accepting more input variables was developed. The significant advantage of this response model is that it provides an exact fit to the observed values and requires the estimation of only one parameter for each factor considered in the experiment.

By considering a sample of n points where $\mathbf{X} = \mathbf{x}^{(1)}, \dots, \mathbf{x}^{(n)}$ denote the inputs and $\mathbf{y} = (y(\mathbf{x}^{(1)}), \dots, y(\mathbf{x}^{(n)}))$ identifies the known output values, the system response can be represented in the following form:

$$y(\mathbf{x}) = \mu(\mathbf{x}) + Z(\mathbf{x}) \quad 6.7$$

where $\mu(\mathbf{x})$ is a deterministic trend function and $Z(\mathbf{x})$ is a Gaussian stochastic process with covariance matrix or kernel $\sigma^2 R(\theta)$. Here σ^2 is a parameter called process variance while the elements of $R(\theta)$, r_{ij} , are the correlations between the outputs of two sample points. As said before, the Kriging model is a spatial correlation model: the correlation between two observations decreases as the design points become more distant. The parameters of the function $\mu(\mathbf{x})$ and the kernel's parameters θ_i are set by using the maximum likelihood method. The obtained estimates are denoted as $\hat{\mu}(\mathbf{x})$ and $\hat{\theta}_i$. Thus, the values of the response can be predicted by using:

$$y(\mathbf{x}) = \hat{\mu}(\mathbf{x}) + Z(\mathbf{x}) \quad 6.8$$

For further details about the Kriging model, refer for example to [35].

6.1.3 ARTIFICIAL NEURAL NETWORKS

Artificial neural networks are surrogate models developed around 1950 which are inspired, as the name suggests, to animal biological neural networks. In particular, the characteristics that these models want to copy from animals' brain are the structure, made up of a lot of elementary units, and the ability to learn something, which is a capability computers do not have. Kriesel in [36] writes: "The study of artificial neural networks is motivated by their similarity to successfully working biological systems, which – in comparison to the overall system – consist of very simple but numerous nerve cells that work massively in parallel and have the capability to learn". Hence, artificial neural networks consist in a certain number of units, the neurons, which are interconnected to form a network. Informations, travelling through the network, are modified and, by inserting some input parameters, the network is able to produce an output. The network is thus comparable to a transfer function able to predict the response of a physical system.

Neuron model: Each neuron of an artificial neural network is actually a simple mathematical function and each connection is actually a weight. Figure 6.2 reports a schematic representation of a neuron model. Here, some input signals produced by other cells, denoted by x_1, x_2, \dots, x_m , are transmitted to the neuron. The transmission of information between neurons is possible thanks to *connections* or *synapses*, which are characterized by a *weight* or *strength*. These in the figure are denoted by $w_{k1}, w_{k2}, \dots, w_{km}$. Then a weighted sum of the m input information is performed to produce a unique input value. This operation is represented in the figure as the summing junction and corresponds to a linear combination of the neuron inputs. The obtained input value can then be increased or lowered by using the *bias* b_k . Finally, the neuron produces an output by applying an *activation function* or *squashing function* $\phi(\cdot)$ to the input. Mathematically, these operations can be represented by the following relations:

$$\begin{aligned} u_k &= \sum_{j=1}^m w_{kj} x_j \\ v_k &= b_k + u_k \\ y_k &= \phi(v_k) \end{aligned} \quad 6.9$$

where u_k is the result of the linear combination, v_k is the value obtained through the application of the bias and y_k is the neuron output.

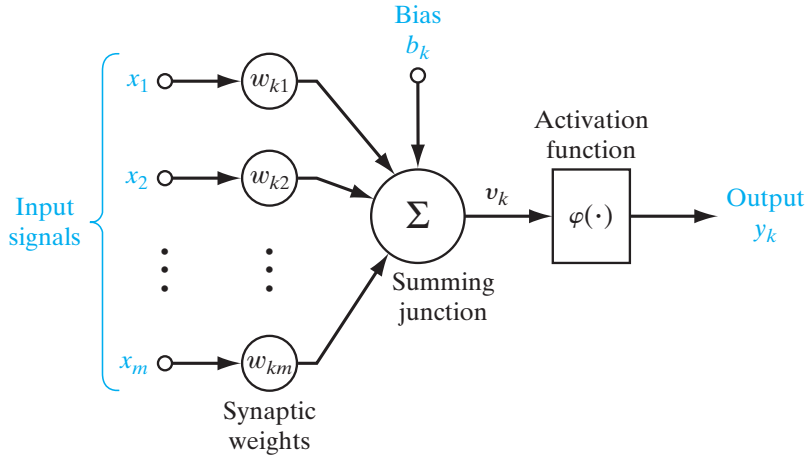


Figure 6.2: Schematic representation of a neuron in artificial neural networks [37].

Activation functions: A lot of activation functions are available. Two simple examples are reported here and their graphics can be observed in Figure 6.3. The first is the *threshold function* or *Heaviside function*, defined as:

$$y_k = \varphi(v_k) = \begin{cases} 1 & \text{if } v_k \geq 0 \\ 0 & \text{if } v_k < 0 \end{cases} \quad 6.10$$

The second is the *sigmoid function*, defined as:

$$y_k = \varphi(v_k) = \frac{1}{1 + \exp(-av_k)} \quad 6.11$$

where a is called *slope parameter*. The activation function thus limits the permissible amplitude range of the output. Typical output's intervals are $[0,1]$ or $[-1,1]$.

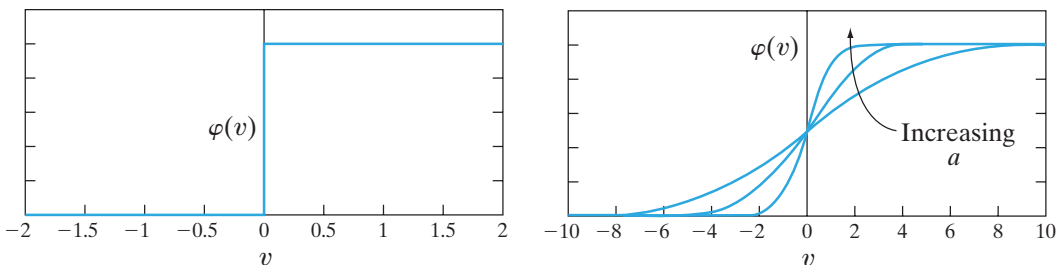


Figure 6.3: Examples of activation function: on the left the threshold function, on the right the sigmoid function [37].

Topology: The neurons of an artificial neural network are organized into layers. Basically there are three types of layers, which are *input*, *output* and *hidden* layers. The input layer presents one neuron for each input variable of the system that the network wants to model, while the output layer is composed of a number of neurons equal to the number of objective functions. Through these layers the network can receive signals, elaborate informations and produce some outputs. Hidden layers are necessary when the system is complicated and cannot be modeled by using only the input and the output layer. The simpler neural networks usually present at least one hidden layer. The number of neurons in the hidden layers can be arbitrarily chosen. An example of neural network topology is shown in Figure 6.4.

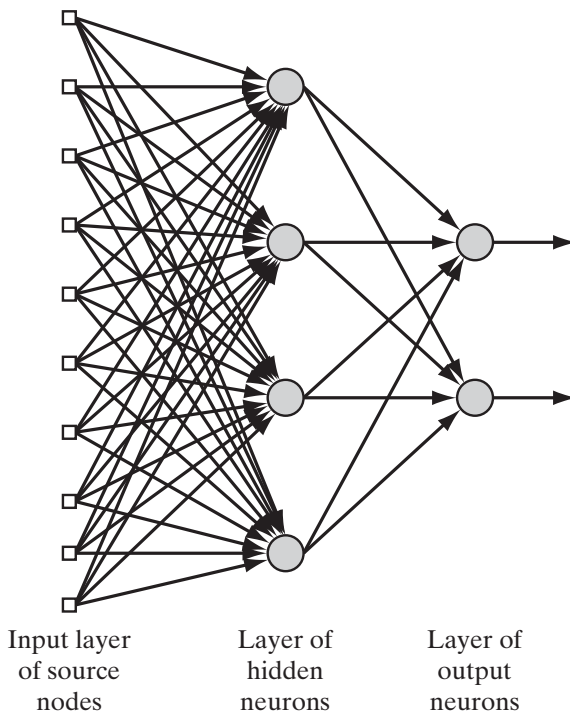


Figure 6.4: Topology of a neural network [37].

Training and testing: Once the topology of the network has been decided and the activation functions of the neurons have been chosen, the network is still unable to predict the response of the system at hand. In fact, the network has to be trained to set the values of the connection weights, the biases and the parameters of each activation function. Usually, a certain number of known design points are available for this purpose and specific algorithms are used to estimate the constants. Finally, the network has to be tested to check its accuracy and reliability. Some known design points are excluded from the training phase and are used at this stage to verify the goodness of the response prediction.

6.2 OPTIMIZATION TECHNIQUES

An optimization problem can always be expressed as the research of the global minimum or maximum of a function. Generally speaking, to introduce this topic it is possible to distinguish between traditional and modern optimization methods. The first are typically mathematical gradient or derivative based algorithms, while the second are usually characterized by a stochastic, random component.

The most commonly used non-traditional optimization methods for the resolution of engineering problems are *genetic algorithms*. One of them will be used in Section 6.3 to optimize the DTMB 5415 geometry. Optimization is a very complex subject which is constantly evolving. Therefore, only a brief explanation of the operating principles of a genetic algorithm is proposed here. Further details can be easily found in literature, for example in [38].

6.2.1 GENETIC ALGORITHMS

These algorithms are suited when the design space is discontinuous and not convex. In these cases in fact, traditional optimization techniques are computationally expensive, inefficient and often unable to find the global minimum.

Genetic algorithms are based on the concepts of biological evolution and, more specifically, on Darwin's theory of *survival-of-the-fittest*. They try to copy from the genetics some mechanisms such as reproduction, crossover and mutation.

In a genetic algorithm the design variables of each design point are written as binary numbers and form a string. This string is the so-called *chromosome* of the individual. An example is reported in Figure 6.5.

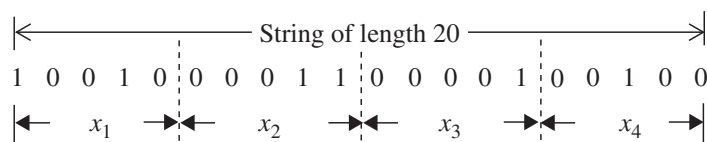


Figure 6.5: Example of chromosome in a genetic algorithm [38].

A typical genetic algorithm consists of the following steps.

Initialization of the population: The first step is the definition of the initial population. Usually individuals are placed randomly in the design space. The population size suggested in literature is of $2n$ or $4n$, where n is the number of the design variables. Once the initial design points have been chosen, the objective or fitness function is evaluated for each individual.

Selection of the parents: This operation consists in the selection of good strings of the population to form a mating pool. There are several selection methods. One of the most

used is the *roulette wheel* where a string is selected from the population with a probability proportional to its fitness. This principle is schematically depicted in Figure 6.6. Thus, probabilistically, design points with high fitness values in the population get more copies in the mating pool. This ensures the respect of the survival-of-the-fittest theory: individuals with a lower value of the objective function will reproduce and live, while the others will die.

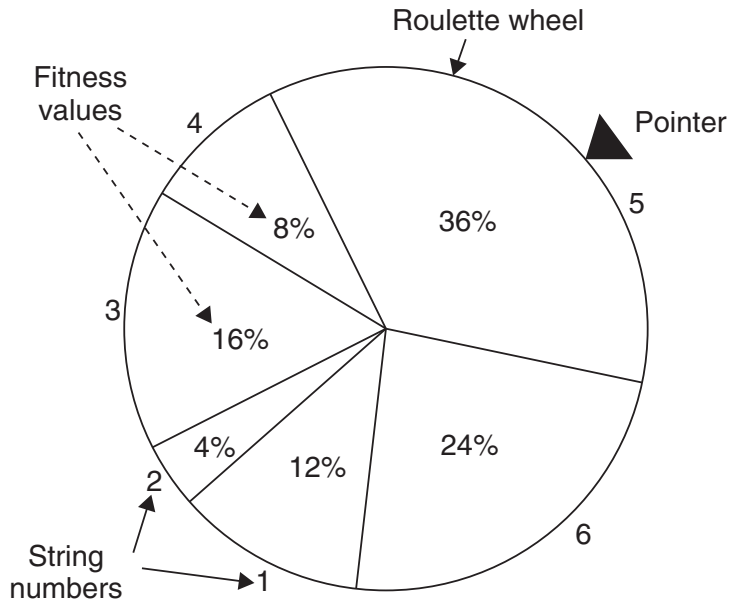


Figure 6.6: Roulette-wheel selection scheme [38].

Crossover: This is the reproduction stage. The individuals which have been selected at the previous stage are the so-called *parents*. Children are created from couples of parents by mixing their genetic material, that is their chromosomes. An example of this operation is reported in Figure 6.7, where \mathbf{X}_1 and \mathbf{X}_2 are the parents, \mathbf{X}_3 and \mathbf{X}_4 are the children.

$$\begin{aligned}
 (\text{Parent 1}) \quad \mathbf{X}_1 &= \{0 \quad 1 \quad 0 \mid 1 \quad 0 \quad 1 \quad 1 \quad 0 \quad 1 \quad 1\} \\
 (\text{Parent 2}) \quad \mathbf{X}_2 &= \{1 \quad 0 \quad 0 \mid 0 \quad 1 \quad 1 \quad 1 \quad 1 \quad 0 \quad 0\} \\
 (\text{Offspring 1}) \quad \mathbf{X}_3 &= \{0 \quad 1 \quad 0 \mid 0 \quad 1 \quad 1 \quad 1 \quad 1 \quad 0 \quad 0\} \\
 (\text{Offspring 2}) \quad \mathbf{X}_4 &= \{1 \quad 0 \quad 0 \mid 1 \quad 0 \quad 1 \quad 1 \quad 0 \quad 1 \quad 1\}
 \end{aligned}$$

Figure 6.7: Example of crossover operation [38].

Mutation: At this step the chromosome of some newly created individuals may be modified randomly. The mutation operator in fact, changes a binary digit of their string from 1 to 0 and vice versa. There are several methods to implement this operation.

Formation of the new generation: Finally a new generation of individuals can be formed. Again, there are several options to do it. For example the new population can be

made up of the best individuals of the previous generation, the children produced during the crossover stage and the individuals produced by the mutation operator.

Normally the total number of generations is decided a priori together with the number of individuals forming the population. The ability of the algorithm to catch the global minimum depends on these numbers, which have to be set according to the number of decision variables.

6.3 OPTIMIZATION OF THE DTMB 5415

In this section, an optimization procedure for DTMB 5415 is proposed, based on the results of the design of experiments carried out in Chapter 5.

Firstly, by using the CFD results of DoE2, three surrogate models have been developed: a linear model with interaction terms, a Kriging model and an artificial neural network. The surrogate models have been used to run a genetic algorithm: for each surrogate model, a geometry minimizing the total drag has been found. Then, the best individuals found through the optimizations have been simulated by using the DTMB02 model to verify the accuracy of the response surfaces. The results obtained from CFD have suggested to focus the attention on a narrower design space. Hence a new DoE, named DoE3, has been performed by adjusting the variables' bounds. Finally, the surrogate models have been updated by using the results of DoE3 and the optimizations have been repeated thus producing interesting results. In the following sections, each stage of this optimization procedure is described in detail.

6.3.1 FIRST OPTIMIZATION: OPT1

Construction of the surrogate models: In DoE2 a sample of 60 different geometries has been analysed by using the DTMB02 numerical model to obtain the total drag value associated to each hull's shape. Starting from these data, three surrogate models have been developed. More specifically, the models have been created in MATLAB: a linear model with interaction terms and a Kriging or gaussian process model have been constructed by using the Regression Learner App, while an artificial neural network has been developed by using the Neural Net Fitting App. For the neural network model, data have been split into three groups made up of 42, 9 and 9 individuals respectively. These have been used to train, validate and finally test the net.

Figure 6.8 depicts the characteristics of each response surface. Fitted and exact resistance values of each sample point, denoted by R_{fit} and R_{CFD} respectively, are normalized with respect to the baseline total resistance, denoted by R_b . By observing the residuals' plots, it is possible to notice that the Kriging model presents lower residuals: it fits the CFD data better than the other models. This may be seen also by examining Table 6.1, where the coefficients of determination and the root mean square error are reported for the three models. The Kriging model is characterized by the closest-to-1 R^2 value and by the lower $RMSE$ value. The neural network shows good performance as well, as it presents R^2 and $RMSE$ values which are close to the Kriging model's ones.

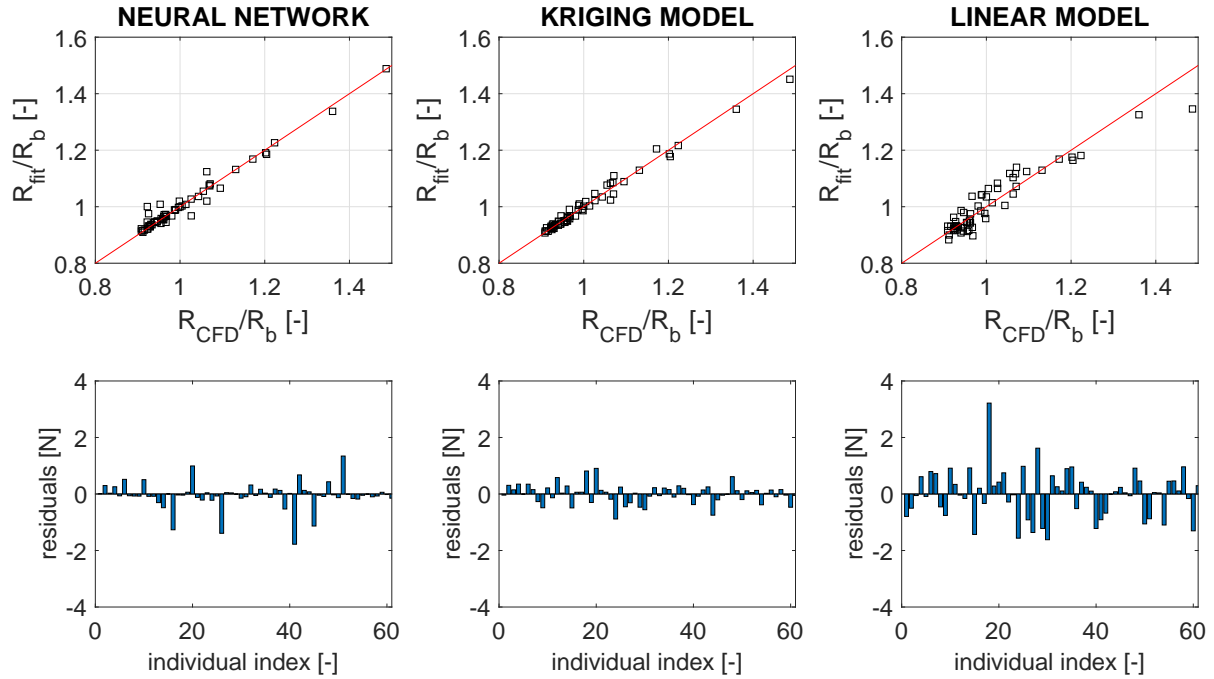


Figure 6.8: Characteristics of the three surrogate models in OPT1. Fitted and exact resistance values of each sample point (R_{fit} and R_{CFD}) are normalized with respect to the baseline total resistance (R_b).

	Neural network	Kriging model	Linear model
Coefficient of determination (R^2) [-]	0.9651	0.9823	0.8836
Root mean square error (RMSE) [N]	0.4660	0.3317	0.8512

Table 6.1: Coefficient of determination and root mean square error calculated with 6.2 and 6.3 for each surrogate model in OPT1.

Optimization and CFD check: The genetic algorithm implemented in MATLAB has been used to run the optimizations. The objective is to minimize the ship's drag. Each optimization has been carried out for 20 generations, using a population of 20 individuals. For each surrogate model, the optimization has provided the geometry minimizing the total resistance. Hence, three optimum hull's shapes have been produced: BEST-NN1 by using the neural network, BEST-KR1 by using the Kriging model and BEST-LIN1 by using the linear model with interaction terms.

In Figure 6.9, all the individuals evaluated by the genetic algorithm during the optimizations are reported for each model. The resistance values are normalized with respect to the baseline resistance, denoted by R_b . It may be noticed that in general, the estimations of the drag force provided by the three models differ a lot: the neural network provides drag values that are much lower than the ones provided by the other models. It may be concluded that at least two of the three surrogate models are not able to produce

an accurate and reliable prediction of the drag. This is coherent with data reported in Table 6.1.

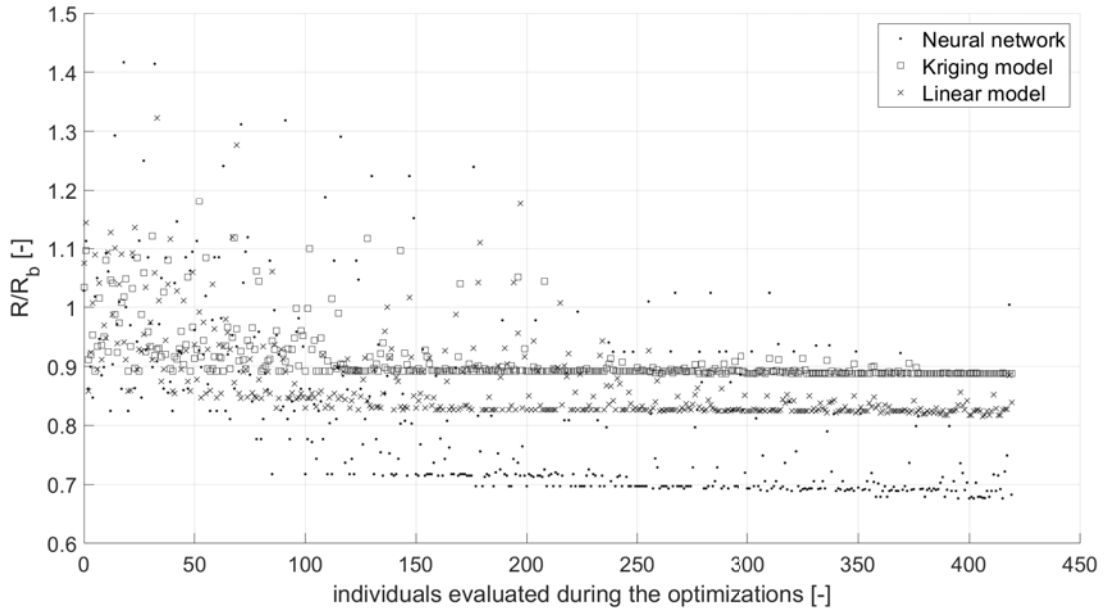


Figure 6.9: OPT1: individuals evaluated during the optimizations on the three surrogate models. R_b denotes the baseline resistance.

To test the accuracy of the surrogate models, the best individuals obtained through the optimizations have been simulated by using the DTMB02 numerical model. Table 6.2 reports the CFD results compared to the predictions provided by the models and the associated percentage errors. It is possible to note that the Kriging model produces the most accurate prediction of the drag, as suggested by Table 6.1.

	Drag value provided by the model [N]	Drag value provided by CFD [N]	Percentage error (%)
BEST-NN1	15.69	20.79	24.53
BEST-KR1	20.47	20.83	1.73
BEST-LIN1	18.62	21.23	12.29

Table 6.2: Comparison between the drag values provided by the models and the ones provided by the CFD simulations for BEST-NN1, BEST-KR1 and BEST-LIN1.

In Table 6.3, the characteristics of the optimum hull geometries provided by the optimizations are reported together with the individuals BEST1 and BEST2 from DoE1 and DoE2. Baseline data are also summarized there. By examining the table, it is possible to observe that all the BEST individuals are clustered in a certain region of the design's space. Hence it is possible to deduce that, although only the Kriging model is able to provide an accurate and reliable prediction of the drag, all the surrogate models are able to approach the minimum. More specifically the optimum hull geometries provided by the neural network and

the Kriging model are quite similar, while BEST-LIN1 presents slightly different values of the decision variables. The variables' bounds of the best individuals suggest what region has to be further investigated in order to catch the minimum. Therefore, it is possible to reduce once again the variables' ranges and repeat the optimization process. The values of the bulb's angle are not commented here because in Chapter 5, this decision variable has proven to have a negligible effect on the ship's drag.

Individual	$a[\circ]$	$w[-]$	$l[-]$	$d[-]$	$R_P[N]$	$R_V[N]$	$R[N]$	$\Delta R(\%)$
Baseline	0	1	1	1	7.914	14.949	22.863	-
BEST1	-2.25	0.75	1.0375	0.75	6.104	14.486	20.590	9.94
BEST2	-0.8437	0.4594	1.1687	1.0625	5.96	14.812	20.772	9.15
BEST-NN1	-2.6027	0.6743	1.1825	1.4961	6.023	14.766	20.789	9.07
BEST-KR1	-0.7239	0.7213	1.1848	1.0439	6.117	14.715	20.833	8.88
BEST-LIN1	-0.0316	0.3101	0.7233	0.5592	6.859	14.369	21.229	7.15

Table 6.3: Characteristics of the baseline, of the best individuals of DoE1 and DoE2 (BEST1 and BEST2) and of the best individuals found with the genetic algorithm by using the surrogate models (BEST-NN1, BEST-KR1, BEST-LIN1). R denotes the percentage reduction of the total resistance.

6.3.2 SECOND OPTIMIZATION: OPT2

The third design of experiments: A third design of experiments, DoE3, has been performed, adjusting the variables' bounds in accordance with the results achieved in the previous section. The bulb's angle has no longer been taken into consideration. Table 6.4 reports the upper and lower bounds set for each variable. The analysis has been performed by using a sample of 40 individuals which have been selected with the Sobol sampling method available in the software CAESES. For each design point, a CFD simulation has been carried out in order to evaluate the total resistance R , the viscous resistance R_V and the pressure resistance R_P .

Figure 6.10 depicts the results of DoE3. Here, resistance values are normalized with respect to the baseline ones (R_b , R_{Pb} and R_{Vb}) and the values of the decision variables are normalized between zero and one. The trend of the resistance as a function of each variable is clear: the resistance grows with the bulb's width and depth, decreases with the bulb's length.

	$w[-]$	$l[-]$	$d[-]$
Lower bound	0.3	0.7	0.5
Upper bound	1.15	1.2	1.5

Table 6.4: Variables' bounds in DoE3.

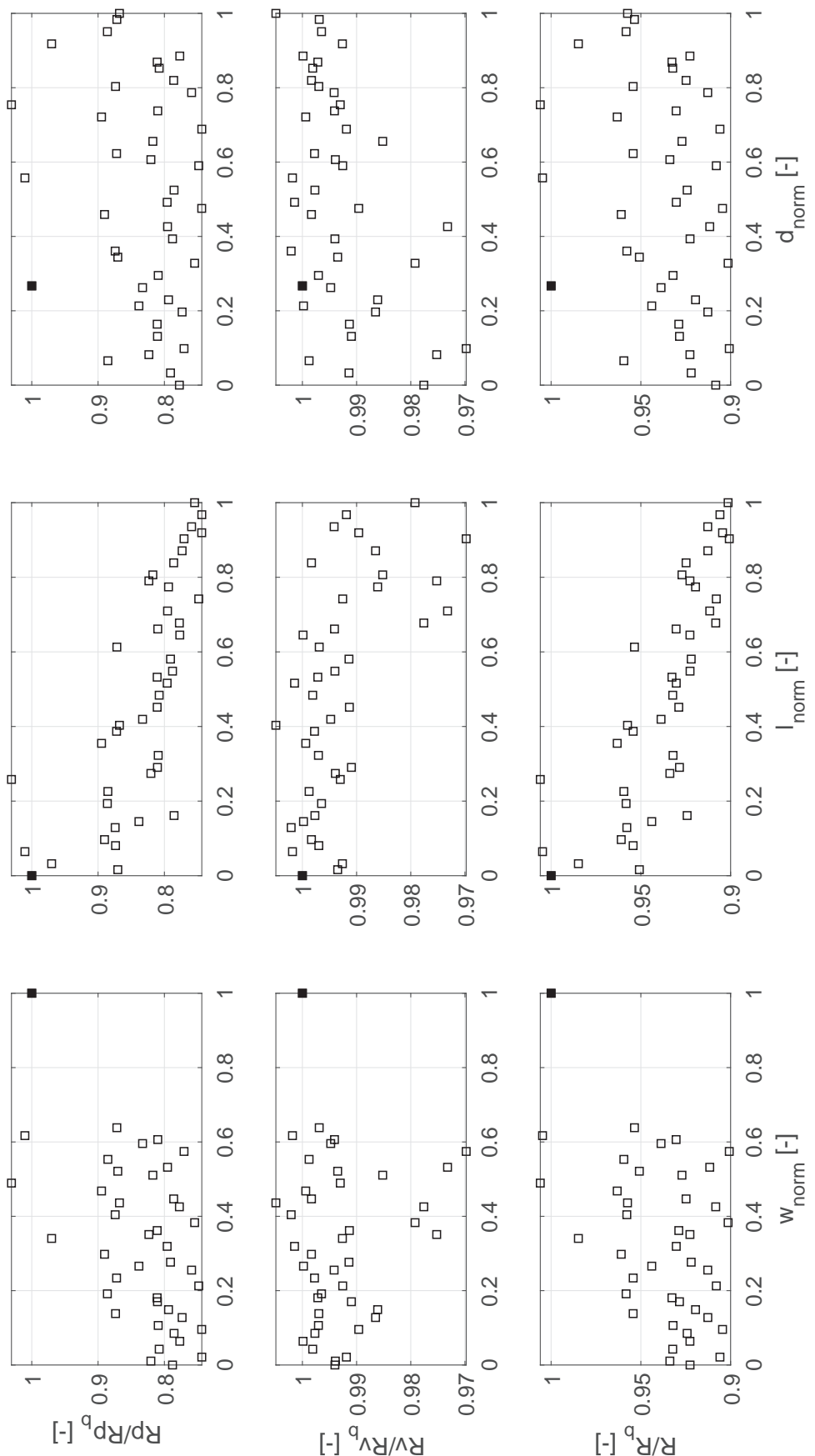


Figure 6.10: Results of DoE3. Variables values are normalized between zero and one. The baseline is represented by the black filled square. R_b denotes the baseline resistance.

In Table 6.5 a comparison between the characteristics of the best hull's geometry simulated in DoE3, BEST3, and the baseline is reported. BEST3 presents a percentage reduction of the total resistance of 9.92%.

Individual	$w[-]$	$l[-]$	$d[-]$	$R_P[N]$	$R_V[N]$	$R[N]$
Baseline	1	1	1	7.914	14.949	22.863
BEST3	0.75	1.175	0.8875	6.097	14.497	20.594

Table 6.5: Characteristics of the baseline and of the best individual in DoE3.

Construction of the surrogate models: CFD data obtained from DoE3 have been used to built three new surrogate models: a linear model with interaction terms, a Kriging model and a neural network. The procedure is the same as in Section 6.3.1. Figure 6.11 shows the characteristics of the models. Fitted and exact resistance values of each sample point, denoted by R_{fit} and R_{CFD} respectively, are normalized with respect to the baseline total resistance, denoted by R_b . Residuals are reported within the same range as in Figure 6.8 to easily compare these models to the ones developed in OPT1. The new models seem to be more accurate, thanks to the new restricted variables' ranges.

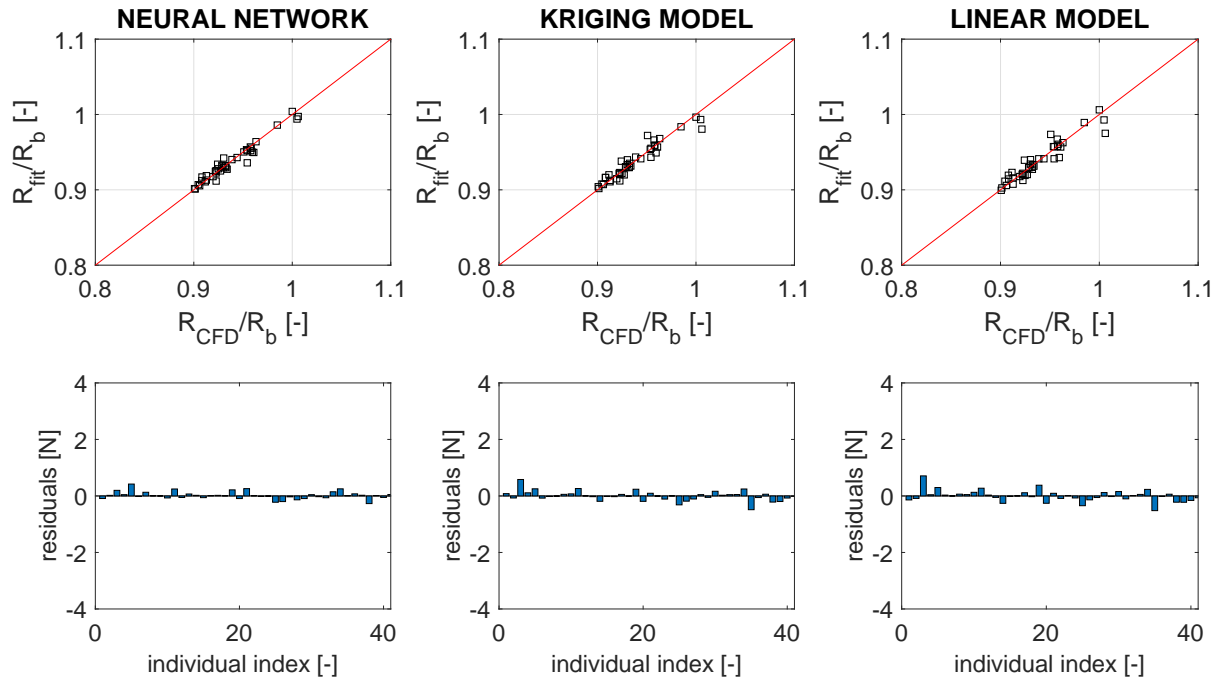


Figure 6.11: Characteristics of the three surrogate models in OPT2. Fitted and exact resistance values of each sample point (R_{fit} and R_{CFD}) are normalized with respect to the baseline total resistance (R_b).

By examining Table 6.6, where the coefficients of determination and the root mean square error are reported for the three models, it might be observed that the values of the coefficients of determination R^2 are worse than in OPT1. This is because here a smaller

number of individuals is used to build the models. However, root mean square errors are lower. Hence, these models should actually be more accurate than the previous ones. In the current case, the more reliable model seems to be the neural network, followed by the Kriging model.

	Neural network	Kriging model	Linear model
Coefficient of determination (R^2) [-]	0.9523	0.9198	0.8911
Root mean square error ($RMSE$) [N]	0.1344	0.1743	0.2031

Table 6.6: Coefficient of determination and root mean square error calculated with 6.2 and 6.3 for each surrogate model in OPT2.

Optimization and CFD check: The optimizations have been performed as in OPT1. Three optimum hull shapes have been produced: BEST-NN2 by using the neural network, BEST-KR2 by using the Kriging model and BEST-LIN2 by using the linear model with interaction terms. Figure 6.11 reports all the individuals evaluated by the genetic algorithm during the optimizations. The resistance values are normalized with respect to the baseline resistance denoted by R_b . By comparing this plot to the one in Figure 6.9, it emerges that in OPT2, drag's predictions provided by the surrogate models are more coherent. In fact, Tables 6.2 and 6.7 show that in OPT2 the accuracies of the linear model and of the neural network have much improved.

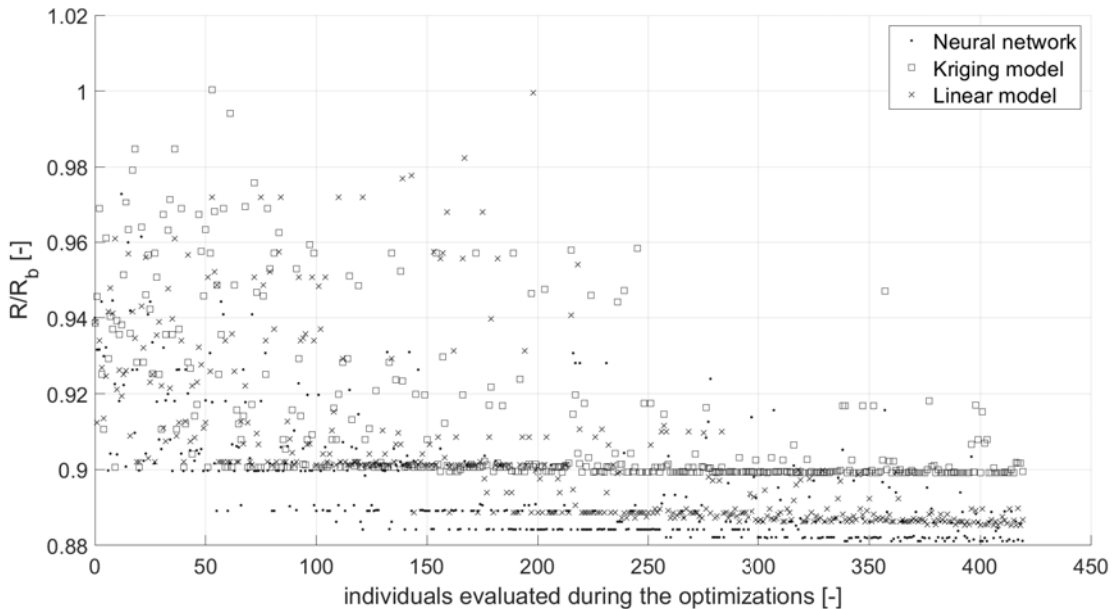


Figure 6.12: OPT2: individuals evaluated during the optimizations on the three surrogate models. R_b denotes the baseline resistance.

The three best individuals obtained in OPT2 have been simulated – as in OPT1 – to test the accuracy of the models. The results are reported in Table 6.7. Although from Table 6.6 the neural network seemed to be the best model, the Kriging model has provided the best prediction of the resistance for the optimum individual, as in OPT1.

	Drag value provided by the model [N]	Drag value provided by CFD [N]	Percentage error (%)
BEST-NN2	20.15	21.16	4.77
BEST-KR2	20.58	20.77	0.91
BEST-LIN2	20.49	21.03	2.57

Table 6.7: Comparison between the drag values provided by the models and the ones provided by the CFD simulations for BEST-NN2, BEST-KR2 and BEST-LIN2.

In Table 6.8 a comparison between the baseline and all the best individuals obtained from DoE1, DoE2, DoE3, OPT1 and OPT2 is reported. It should be noted that the individual characterized by the lowest resistance is BEST1, obtained in the first design of experiments. Figure 6.13 shows its geometry, compared to the baseline.

Individual	$a[\circ]$	$w[-]$	$l[-]$	$d[-]$	$R_P[N]$	$R_V[N]$	$R[N]$	$\Delta R(\%)$
Baseline	0	1	1	1	7.914	14.949	22.863	-
BEST1	-2.25	0.75	1.0375	0.75	6.104	14.486	20.590	9.94
BEST2	-0.8437	0.4594	1.1687	1.0625	5.96	14.812	20.772	9.15
BEST-NN1	-2.6027	0.6743	1.1825	1.4961	6.023	14.766	20.789	9.07
BEST-KR1	-0.7239	0.7213	1.1848	1.0439	6.117	14.715	20.833	8.88
BEST-LIN1	-0.0316	0.3101	0.7233	0.5592	6.859	14.369	21.229	7.15
BEST3	-	0.75	1.175	0.8875	6.097	14.497	20.594	9.92
BEST-NN2	-	0.5732	1.1511	1.4945	6.241	14.923	21.164	7.43
BEST-KR2	-	0.7303	1.1956	1.029	6.12	14.646	20.766	9.17
BEST-LIN2	-	0.4262	1.1986	1.4639	6.074	14.955	21.029	8.02

Table 6.8: Characteristics of the baseline compared to the characteristics of best individuals of DoE1, DoE2, DoE3 (BEST1 and BEST2 and BEST3) and of the best individuals found with the genetic algorithm using the surrogate models in OPT1 (BEST-NN1, BEST-KR1, BEST-LIN1) and OPT2 (BEST-NN2, BEST-KR2, BEST-LIN2). R denotes the percentage reduction of the total resistance.

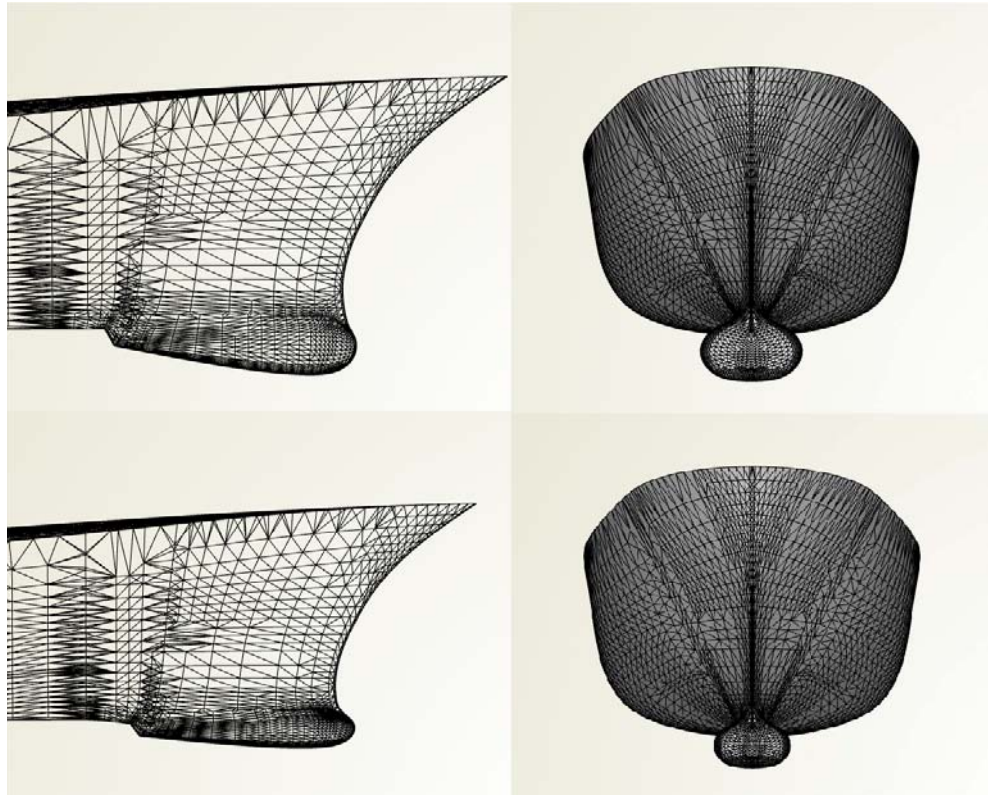


Figure 6.13: Comparison between the shape of BEST1 (second row) and the baseline (first row).

6.4 CONCLUSIONS

In this chapter surrogate models, also called response surfaces, and optimization techniques have been introduced.

A response surface is a mathematical/statistical model of a physical system, able to predict its response when one or more input parameters are changed. It may be useful in optimization problems that involve CFD simulations, as it can provide an approximation of the result in few seconds, thus reducing time and cost required for the analyses. Here the attention is focused on polynomial models, Kriging models and neural networks.

Optimization techniques are increasingly used in engineering problems to find the design which maximizes the performance of a product, minimizes its cost and so on. There are several optimization methods, which may be split into traditional and modern. Among the modern approaches, genetic algorithms are suited when the design space is discontinuous and not convex. In these cases, in fact, traditional techniques are computationally expensive, inefficient and often unable to find the global minimum/maximum. These algorithms are introduced and described in this chapter.

The original part of this chapter consists in an optimization procedure for the DTMB 5415. Two iterations, named OPT1 and OPT2, have been necessary to achieve interesting results.

OPT1: By using the 60 geometries simulated in DoE2, three surrogate models have been developed in MATLAB: a linear model with interaction terms, a Kriging model and an artificial neural network. The Kriging model ($R^2 = 0.9823$ and $RMSE = 0.3317N$) has proven to be the more accurate, followed by the neural network ($R^2 = 0.9651$ and $RMSE = 0.4660N$).

The surrogate models have been used to run the genetic algorithm implemented in MATLAB. The optimizations have been carried out for 20 generations, using a population of 20 individuals. For each model, a geometry minimizing the total drag has been found: BEST-NN1 using the neural network, BEST-KR1 using the Kriging model and BEST-LIN1 using the linear model with interaction terms.

These individuals have been simulated by using the DTMB02 model to verify the accuracy of the response surfaces. The drag prediction provided by the Kriging model was found to be the most accurate, with an associated percentage error of 1.73%. The other models, instead, have proven to be inaccurate: the percentage error amounts to 12.29% for the linear model and 24.53% for the neural network. However, all the best individuals obtained through the optimizations present drag values which are lower than the baseline's. BEST-NN1 presents the highest reduction of the resistance, equal to 9.07%. The CFD results have suggested to focus the attention on a narrower design space.

OPT2: A new design of experiments, named DoE3, has been performed adjusting the variables' bounds in accordance with the results of OPT1. In DoE3, 40 individuals have been selected by using the Sobol algorithm available in CAESES and simulated in Open-FOAM. The results show a clear trend of the resistance as a function of each variable: the resistance grows with the bulb's width and depth, decreases with the bulb's length. The best hull geometry obtained in DoE3, BEST3, presents a percentage reduction of the total resistance of 9.92%.

Three new surrogate models have been developed as in OPT1. In this case the neural network presents the closest-to-1 R^2 value and the lower $RMSE$ value ($R^2 = 0.9523$ and $RMSE = 0.1344N$) followed by the Kriging model ($R^2 = 0.9198$ and $RMSE = 0.1743N$). The values of the coefficients of determination R^2 are worse than in OPT1 because here a smaller number of individuals is used to build the models. However, root mean square errors are lower. Hence these models should be more accurate than the previous one.

As in OPT1, three optimizations have been performed by using the surrogate models and for each model, a hull geometry minimizing the total drag has been found. These are BEST-NN2, obtained by using the neural network, BEST-KR2, obtained by using the Kriging model and BEST-LIN2, obtained by using the linear model with interaction terms.

Once again, these individuals have been simulated by using the DTMB02 model to verify the accuracy of the response surfaces. Although from R^2 and $RMSE$ data the neural network seemed to be the best model, the Kriging model has provided the most accurate prediction of the resistance, as in OPT1, with an associated percentage error of 0.91%. The predictions provided by the other models have improved compared to OPT1: the percentage error amounts to 2.57% for the linear model and 4.77% for the neural network. BEST-KR2 presents the highest reduction of the resistance, equal to 9.17%.

It should be noted that among all the best individuals obtained in DoE1, DoE2, DoE3, OPT1 and OPT2, the geometry characterized by the lowest resistance is BEST1.

Conclusions

CONCLUSIONS

This thesis concerns the study of the hydrodynamic performance of a ship. The subject is broad, hence the attention is focused on few important aspects. More specifically, emphasis is placed on ship's resistance and on techniques to reduce it according to the modern design approach, which involves numerical analyses and optimization methods. All facets of the modern ship design process are described in detail: from the physics of the problem to the prediction of ship performance, from the modeling of the geometry to the choice of some influential variables and the optimization of the shape.

Each chapter deals with a particular aspect of the design process and introduces theories and principles behind it, as well as methods to cope with it. Then, in Chapters from 3 to 6 these methods are applied to a practical case: the DTMB 5415 ship.

Chapter 1 introduces the physics of the problem, focusing the attention on the components of ship resistance and on the similarity laws for naval applications. In Chapter 2, numerical methods are introduced and in particular, the most commonly used techniques to deal with two phases flows are explained. The DTMB 5415 case study is presented in Chapter 3, where the validation of a CFD model for this ship is carried out. Chapter 4 is about geometry modeling: the main approaches are summarized and a parametrization is proposed for the DTMB 5415 case. In Chapter 5, design of experiments techniques are described and applied to the DTMB 5415 to evaluate the influence of variables on ship performance. Finally, in Chapter 6, an introduction to surrogate models and optimization methods is proposed and an optimization procedure is implemented to find the best DTMB 5415 design configuration.

Validation: The validation of an OpenFOAM numerical model for the DTMB 5415 has been carried out by using the InterFoam solver in three phases. Firstly, the DTC hull tutorial case available in OpenFOAM has been run to see if this model could be a good starting point. This simulation has led to results in good agreement with experimental data. Then, the DTMB 5415 geometry has been inserted in the tutorial case and the simulation, named DTMB01, has been performed without any modification. This has been possible because the DTC hull model and the DTMB 5415 model share similar dimensions. Finally the mesh has been modified to improve the wave pattern prediction. This last model is denoted by DTMB02.

The percentage error in the resistance predictions amounts to 0.6%, 1.1% and 1.2% for the DTC hull, the DTMB01 model and the DTMB02 model respectively. In the DTMB02 model, the mesh elements have been increased from 896 917 to 2 356 423 to achieve a better prediction of the wave pattern. The drawback is a longer computational time. However this model has been preferred because, as the wave-making resistance is the main component of the ship's drag, an accurate prediction of the wave pattern is essential.

The DTMB02 flow field has been studied and compared with the experimental one. The main hydrodynamic phenomena are caught by the CFD analysis, while some smaller vortex structures cannot be noticed on the simulation's contour. To catch them properly,

a further increase of the number of cells would have been necessary. However the DTMB02 model has been considered to be a good compromise between accuracy and computational time and, therefore, validated for the purposes of this thesis.

Parametrization: The attention has been focused on two details of the geometry, which are the bulbous bow and the transom stern. The parametrization has been carried out by using the commercial software CAESES.

The free form deformation method has been adopted to produce modifications of the bulbous bow. The parameters involved are the bulb's length, width, depth and angle. For width, length and depth, the design variables correspond to the scale factors used to obtain the deformation. Instead, for the bulb's angle the design variable is the rotation angle applied to the deformation box. The free form deformation method has proven unsuitable for the stern parametrization, hence a conventional approach has been used here: the stern's shape has been reconstructed by using points and NURBS curves, taking as design variable the z-coordinates of the points. This allows to modify the stern's depth.

The parametrization proposed for the DTMB 5415 does not take into consideration any constraint, i.e. it does not guarantee that the length, the displacement volume and other geometrical features of the modified hulls are kept as in the baseline. In principle, this approach is not correct because the ship's main dimensions influence the hydrodynamic performance and the mechanical behaviour. However, constraints have not been taken into account to simplify the problem.

Design of experiments: The analysis has been carried out in two phases: DoE1 and DoE2. In both cases, a sample of individuals has been selected by using the Sobol sampling technique available in the software CAESES. Then, each hull geometry has been tested in OpenFOAM by using the DTMB02 numerical model. The CFD simulations have provided for each individual the values of the total resistance R , viscous resistance R_V and pressure resistance R_P . In both DoE1 and DoE2, viscous resistance has proven a negligible component of the total drag, as the latter and the pressure resistance have shown the same trends. Therefore, the attention has been focused on the total resistance only. Finally the ANOVA method, available in the statistical software R, has been used to analyse the results.

DoE1 and DoE2 have been performed by using samples of 40 and 60 individuals respectively. In DoE1, the variables' ranges have been set rather wide to enable a proper exploration of the domain. In DoE2, they have been adjusted in accordance with the results of DoE1. The analysis of variance has shown that the stern's depth and the bulb's angle have a negligible influence on the total resistance. Hence these variables have not been taken into account in the further analyses.

By comparing the best individuals obtained in DoE1 and DoE2, denoted as BEST1 and BEST2, it is possible to observe that they present a similar value of the drag force but quite different shapes. Further analyses are then necessary to understand whether a global minimum exists. BEST1 and BEST2 present a percentage reduction of the resistance equal to 9.94% and 9.15% respectively.

Surrogate models and optimization: The optimization has been carried out in two iterations, OPT1 and OPT2. In each iteration, three surrogate models have been devel-

oped in MATLAB: a linear model with interaction terms, a Kriging model and an artificial neural network.

In OPT1, the models have been developed by using the 60 hull geometries simulated in DoE2. In OPT2, a new design of experiments (DoE3) with 40 individuals has been performed by reducing variables' bounds in accordance with the results of OPT1. These new hull geometries have been used to build the surrogate models. Then, both in OPT1 and OPT2, the models have been used to run the genetic algorithm implemented in MATLAB and for each model a geometry minimizing the total drag has been found: BEST-NN1, BEST-KR1, BEST-LIN1 in OPT1 and BEST-NN2, BEST-KR2, BEST-LIN2 in OPT2. These individuals have been simulated by using the DTMB02 model to verify the accuracy of the response surfaces.

- Both in OPT1 and OPT2, the drag predictions provided by the Kriging model are the most accurate, with an associated percentage error of 1.73% and 0.91% respectively. The other models have proven to be inaccurate in OPT1 – the percentage error is equal to 12.29% for the linear model and 24.53% for the neural network – whereas their accuracies have improved in OPT2 – the percentage error is equal to 2.57% for the linear model and 4.77% for the neural network. It may be concluded that the Kriging model is the more reliable and that it is able to provide a good estimation of the resistance also when the variables' domain is extended, as in OPT1. The other models, instead, provide an accurate prediction of the ship's drag only in a narrower design's space, as in OPT2.
- All the best individuals obtained through the optimizations in OPT1 and OPT2 present drag values which are lower than the baseline's. This means that, although the neural network and the linear model are less accurate than the Kriging model, all models are able to move towards the optimum.
- It has been said that BEST1 and BEST2, from DoE1 and DoE2, present a percentage reduction of the resistance equal to 9.94% and 9.15% respectively. The best hull's geometry obtained in DoE3, BEST3, is characterized by a percentage reduction of the drag of 9.92%. In OPT1 and OPT2, BEST-NN1 and BEST-KR2 present the highest reductions of the resistance, equal to 9.07% and 9.17% respectively. Hence, among all the best individuals obtained in DoE1, DoE2, DoE3, OPT1 and OPT2, the geometry characterized by the lowest resistance is BEST1. This result suggests that a simple design of experiments may be sufficient to improve the ship's performance if there is not enough time to perform further analyses. In the optimization procedure proposed in this thesis, the surrogate models are not able to improve the design configuration: the procedure has to be ameliorated.
- Finally, the results of DoE3 show a clear trend of the resistance as a function of each variable: the resistance grows with the bulb's width and depth, decreases with the bulb's length.

BIBLIOGRAPHY

- [1] L. Larsson, F. Stern, M. Visonneau. *Numerical Ship Hydrodynamics - An assessment of the Gothenburg 2010 Workshop*. Springer, 2014.
- [2] J. Wu, X. Liu, M. Zhao, D. Wan. *Neumann-Michell Theory-Based Multi-Objective Optimization of Hullform for a Naval Surface Combatant*. Applied Ocean Research VOL.63 PP.129-141, 2017.
- [3] A. Serani, G. Fasano, G. Liuzzi, S. Lucidi, U. Iemma, E. F. Campana, F. Stern, M. Diez. *Ship Hydrodynamic Optimization by Local Hybridization of Deterministic Derivative-Free Global Algorithms*. Applied Ocean Research VOL.59 PP.115-128, 2016.
- [4] F. Huang, C. Yang. *Hull Form Optimization of a Cargo Ship for Reduced Drag*. Journal of Hydrodynamics VOL.28 NO.2 PP.173-183, 2016.
- [5] H. Kim, C. Yang. *A New Surface Modification Approach for CFD-Based Hull Form Optimization*. Journal of Hydrodynamics VOL.22 NO.5 PP.520-525, 2010.
- [6] Y. H. Hou, X. J. Jiang, X. H. Shi. *Ship Hull Optimization Based on New Neural Network*. Journal of Computers VOL.28 NO.1 PP.137-148, 2017.
- [7] E. Besnard, A. Schmitz, H. Hefazi, R. Shinde. *Constructive Neural Networks and Their Application to Ship Multidisciplinary Design Optimization*. Journal of Ship Research VOL.51 NO.4 PP.297-312, 2007.
- [8] W. Luo, L. Lan. *Design Optimization of the Lines of the Bulbous Bow of a Hull Based on Parametric Modeling and Computational Fluid Dynamics Calculation*. Mathematical and Computational Applications VOL.22 NO.4, 2017.
- [9] J. W. Yu, C. M. Lee, I. Lee, J. E. Choi. *Bow Hull-Form Optimization in Waves of a 66000 DWT Bulk Carrier*. International Journal of Naval Architecture and Ocean Engineering VOL.9 PP.499-508, 2017.
- [10] K. Suzuki, H. Kai, S. Kashiwabara. *Studies on the Optimization of Stern Hull Form Based on a Potential Flow Solver*. Journal of Marine Science and Technology VOL.10 PP.61-69, 2005.
- [11] I. Marini -Kragi , D. Vu ina, M. urkovi . *Efficient Shape Parameterization Method for Multidisciplinary Global Optimization and Application to Integrated Ship Hull Shape Optimization Workflow*. Computer-Aided Design VOL.80 PP.61-75, 2016.
- [12] A. Cominetti. Open-source shape optimization: an application to bulbous bow. Master s thesis, University of Genova, Mechanical Engineering, 2017.
- [13] J. H. Park, J. E. Choi, H. H. Chun. *Hull-Form Optimization of KSUEZMAX to Enhance Resistance Performance*. International Journal of Naval Architecture and Ocean Engineering VOL.7 PP.100-114, 2015.

Bibliography

- [14] Z. C. Hong, Z. Zong, H. T. Li, H. Hefazi, P. K. Sahoo. *Self-Blending Method for Hull Form Modification and Optimization*. Ocean Engineering VOL.146 PP.59-69, 2017.
- [15] T. N. Duy, T. Hino. *A Study on the Stern Shape Optimization of a Container Ship using Navier-Stokes Analysis*. 2015.
- [16] Anthony F. Molland. *Ship Resistance and Propulsion*. Cambridge University Press, 2011.
- [17] J.S. Carlton. *Marine Propellers and Propulsion*. Butterworth-Heinemann, 2007.
- [18] H. Schneekluth, V. Bertram. *Ship Design for Efficiency and Economy*. Butterworth-Heinemann, 1987.
- [19] J. O Dea, D. Jenkins, T. Nagle. *Flow Characteristics of a Transom Stern Ship*. David W. Taylor Naval Ship Research and Development Center Report, 1981.
- [20] V. Bertram. *Practical Ship Hydrodynamics*. Butterworth-Heinemann, 2000.
- [21] S. Mirjalili, S. S. Jain, M. S. Dodd. *Interface-Capturing Methods for Two-Phase Flows: An Overview and Recent Developments*. Center for Turbulence Research, 2017.
- [22] V. Vuković, H. Jasak, . Malenica. *Decomposition Model for Naval Hydrodynamic Applications, Part I: Computational Method*. Ocean Engineering VOL.121 PP.37-46, 2016.
- [23] Christopher J. Greenshields. *OpenFOAM User's Guide 5.0*. OpenFOAM Foundation Ltd, 2017.
- [24] A. Olivieri, F. Pistani, A. Avanzini, F. Stern, R. Penna. *Towing Tank Experiments of Resistance, Sinkage and Trim, Boundary Layer, Wake and Free Surface Flow Around a Naval Combatant Insean 2340 Model*. IIHR Technical Report No. 421, 2001.
- [25] O. el Moctar, V. Shigunov, T. Zorn. *Duisburg Test Case: Post-Panamax Container Ship for Benchmarking*. Journal of Ship Technology Research VOL.59 NO.3 PP.50-65, 2012.
- [26] E. V. Lewis. *Principles of Naval Architecture VOL.2: Resistance, Propulsion and Vibration*. The Society of Naval Architects and Marine Engineers, 1988.
- [27] A. Biran, R. L. Pulido. *Ship Hydrostatics and Stability*. Butterworth-Heinemann, 2003.
- [28] S. Harries, C. Abt, K. Hochkirch. *Modelling Meets Simulation - Process Integration to Improve Design*. Honorary colloquium for Prof. Hagen, Prof. Schlüter and Prof. Thiel, 2004.
- [29] S. Jeong, H. Kim. *Development of an Efficient Hull Form Design Exploration Framework*. Hindawi Publishing Corporation, Mathematical Problems in Engineering, 2013.
- [30] T. W. Sederberg, S. R. Parry. *Free-Form Deformation of Solid Geometric Models*. SIGGRAPH Computer Graphics VOL.20 NO.4 PP.151-160, 1986.
- [31] D. C. Montgomery. *Design and Analysis of Experiments*. John Wiley and Sons, 2013.
- [32] F. Genovese. *Performance Assessment of Surrogate Model Integrated with Sensitivity Analysis in Multi-Objective Optimization*. Master thesis in mathematical engineering, 2016-2017.
- [33] M. Cavazzuti. *Optimization Methods: From Theory to Design*. Springer, 2013.

- [34] K. Friston, J. Ashburner, S. Kiebel, T. Nichols, W. Penny. *Statistical Parametric Mapping: The Analysis of Functional Brain Images*, chapter Analysis of Variance by W. Penny, R. Henson. Elsevier, 2006.
- [35] O. Roustant, D. Ginsbourger, Y. Deville. *DiceKriging, DiceOptim: Two R Packages for the Analysis of Computer Experiments by Kriging-Based Metamodeling and Optimization*. Journal of Statistical Software VOL.51 NO.1, 2012.
- [36] D. Kriesel. Neural networks and learning machines, 2007.
- [37] S. Haykin. *A Brief Introduction to Neural Networks*. Pearson, 2009.
- [38] S. S. Rao. *Engineering Optimization*. John Wiley & Sons, 2009.

